Department of Precision and Microsystems Engineering

Visualisation of ultrasound waves in air to support acoustic levitation

W.M. Mooiweer

Report no : 2023.031
Coach : Vincent Bos
Professor : Peter Steeneken
Specialisation : Engineering Dynamics & Mechatronics System Design
Type of report : MSc. Thesis
Date : 19 May 2023

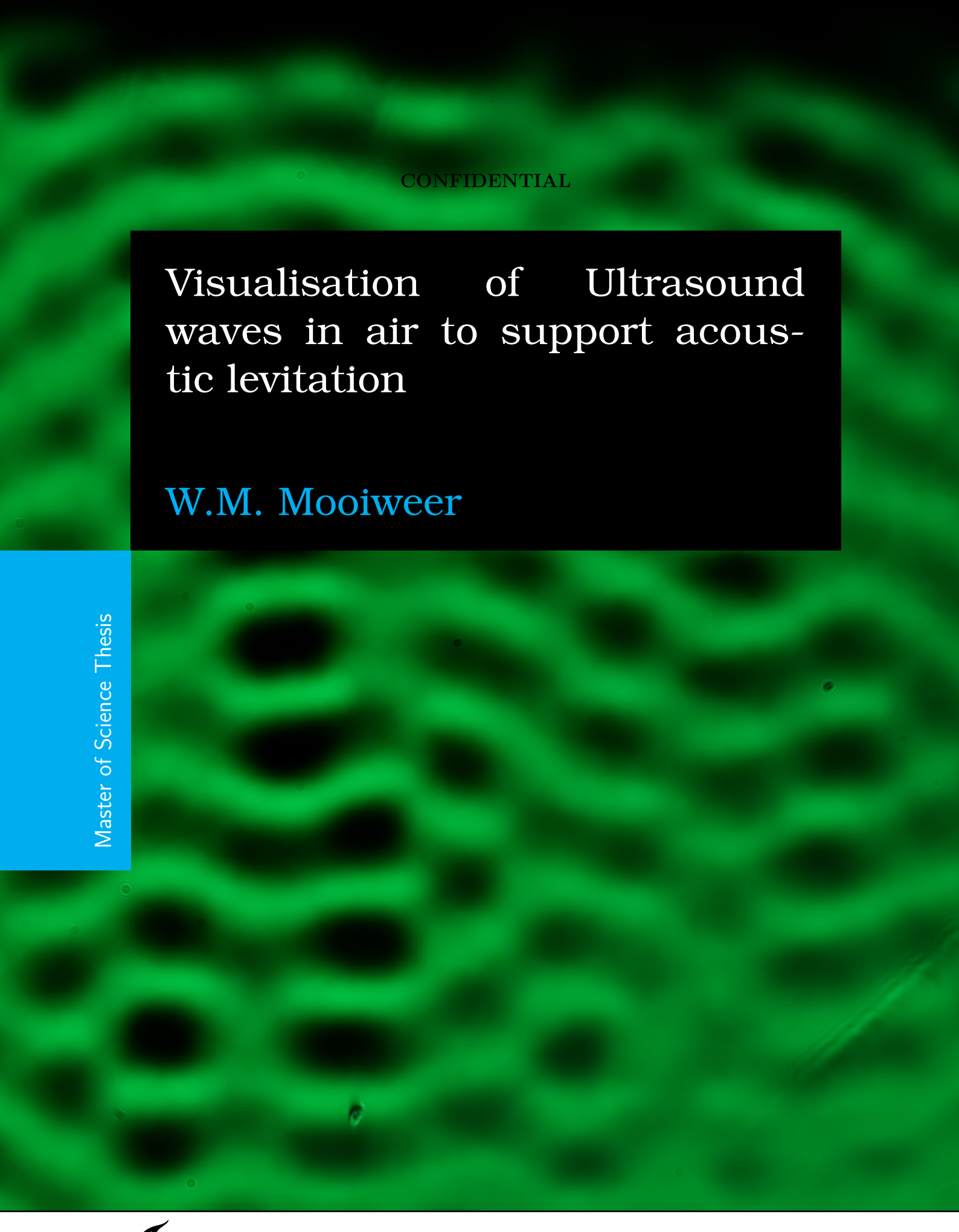

CONFIDENTIAL

Visualisation of Ultrasound waves in air to support acoustic levitation

W.M. Mooiweer

Master of Science Thesis

TU Delft Delft University of Technology

Precision and Micro-systems Engineering

MSCCONFIDENTIAL

Visualisation of Ultrasound waves in air to support acoustic levitation

Master of Science Thesis

For the degree of Master of Science in High-Tech Engineering at Delft University of Technology

W.M. Mooiweer

May 19, 2023

Faculty of Mechanical, Maritime and Materials Engineering (3mE) · Delft University of Technology

Abstract

Acoustic levitation is an novel method that could lend itself very useful to fast and precise transportation of small objects. To verify the acoustic field and the modelling assumptions, the acoustic field must be visualised and quantified. Different methods to visualise a pressure gradient are investigated and rated against design requirements. These requirements are: 1. difficulty, as the setup should be buildable within the period of a MSc. thesis. 2. Time per measurement and 3. measurement sensitivity. It is decided that using a double coincidence spherical mirror schlieren setup is most suitable measurement method. To capture the high speed sphenomena of ultrasound acoustic waves in air, the schlieren light source is pulsed and matched to the frequency of the acoustics to 'freeze' the acoustic wave in the air. Parameters that influence the schlieren image are identified and studied. These parameters are duty cycle, cut-off, ISO, light source phase delay and light source frequency. A horizontal cut-off is determined as the best, while it is determined that the other parameters can be adjusted dependent on the acoustic field. The acoustic field generated by double phased array is observed. Trap locations and types can be identified using the schlieren system. Quantification of the schlieren images has been attempted but without satisfactory results, mainly due to an interesting observation regarding a correlation between the camera focus distance and the pressure gradient. The schlieren system is a useful research tool and successful at visualising the pressure gradient under the assumption that it is constant over the optical axis. Further research is needed to for quantification and to assess the impact of the observation.

Table of Contents

List of Figures

List of Tables

Acknowledgements

I would like to thank my supervisors Peter Steeneken en Vincent Bos for their assistance and guidance during the writing and research of this thesis. I would also like to thank the rest of the acoustic levitation group, and in particular Gerard Verbiest and Frederike Wörtche for their support while writing my thesis and the interesting discussions along the way.

Delft, University of Technology
May 19, 2023

W.M. Mooiweer

0-1 Introduction

0-1-1 General

To many people, the concept of levitating objects with sound is taken directly from a science fiction movie. For some reason levitation in general is always an area of interest for humankind. For some, flying and levitating has a sort of magical feeling of freedom attached to it. Acoustic levitation sounds so easy and intriguing but also impossible and difficult; using only sound to levitate? 'You're telling me that is possible?!' Wouldn't every kid want to strap a bookshelf speaker to a skate board and create the coolest hover board? It sounds unreal since it's not something that is easily stumbled upon in everyday life. The conditions under which acoustic levitation is possible are mostly known but a lot of research into the details is yet to be done.

0-1-2 Introduction

Acoustic levitation can be used for in many applications that demand contact-less handling of items. Liquid drops can be mixed and moved without contact and solids can be moved at high speeds to create holographic displays. To move particles at high speed and precision exact knowledge on the acoustic field is needed. At the point of writing this report, the goal is to use ultrasonic frequencies to move multiple objects through air. In order to research the ultrasound waves and the interaction with the levitated particles one must understand the pressure fields that are generated by the standing waves. The visualisation and quantification of the pressure gradient will enable the verification of theory with real life.

The goal of the visualisation of the ultrasound waves is useful for the following reasons:

1. Visualising the ultrasound waves is great for increased understanding of the acoustic field during the research phase. It allows for easily verifying if the acoustic field and the location of the levitated particle.
2. Visualising the ultrasound waves might help find the lack in acoustic levitation existing models. In the modelling of acoustic field and the associated levitated particle movements, the cause of low frequency motions is still unknown. The transducers are the actuators that are controlled, yet the acoustic field interacts with the particle. To model and determine the particle movement, the acoustic field needs to be verified.

While quantifying the existing models would be terrific, it is not the main goal of visualising the standing waves. The main goal of this setup is to have a research tool to better understand what is going on by visualisation. As a lot of information can be gained through visualisation alone.

0-1-3 Aim of the study

The goal of this study is to increase the ability of acoustically levitating particles through pressure gradient visualisation. The design and construction of a research tool is needed

for the further research into acoustic levitation. Once the tool is assembled, improvements towards acoustic levitation can be made which leads to the following main research questions:

- To what extent can improvements be made to acoustic levitation using visualisation of the pressure gradient?
  - What is the most suitable pressure gradient visualisation technique?
  - To what extent do visualisation technique parameters influence the visualisation of the acoustic field?
  - What factors that influence acoustic levitation can be visualised?
  - To what extent can the visualisations be quantified?

0-1-4 Outline of the study

This thesis is divided into three main sections: THe parameters that influence the visualisation, visualisation of the acoustic field and quantification. These are covered in chapters 3 and 4, and 5 respectively. Leading up to these chapters is chapter 1, where supporting theory will be explained. This chapter covers basic theory on acoustic levitation and theory to understand relevant measurement techniques. A suitable measurement technique is also chosen and the experimental setup is described in chapter 2. The influence of certain setup parameters, such as duty cycle and phase delay, on the visualisation is covered in chapter 3. Chapter 4 covers visualisation of factors that influence the particle stability such as the acoustic field but also reflections and thermal flow. A schematic overview of this is given in Figure 1.

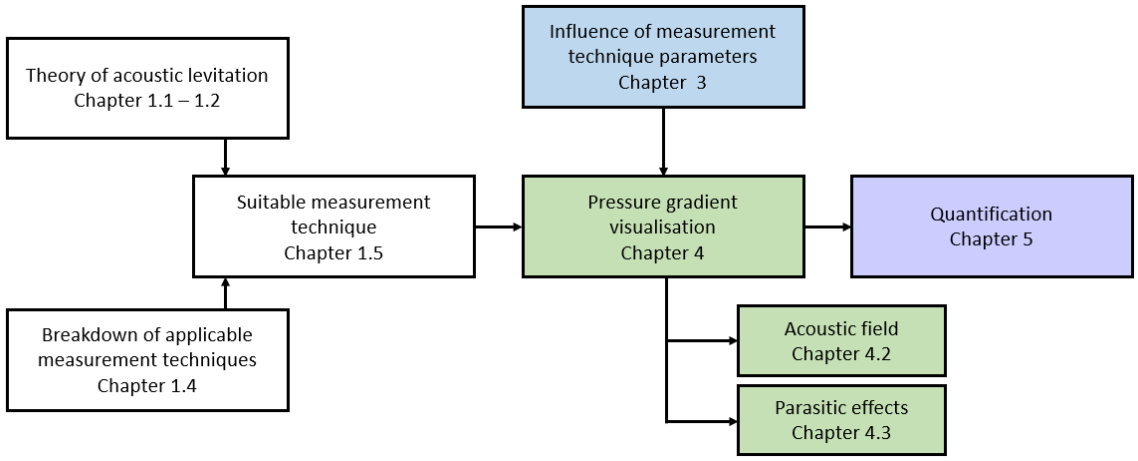

Figure 1: Outline of study

Not present in the figure are the final chapters concluding the findings and giving an outlook for further research.

Chapter 1

Theory

In this chapter some light will be shown on the theory that is needed to read this report and understand the design decisions that are taken. The basics of acoustic levitation will be covered through focus on the physics of acoustics and the physics of the levitated particle. Also covered are multiple measurement techniques. This section covers both a brief overview of relevant theory and the state-of-the-art from literature with respect to pressure gradient visualisation techniques.

1-1 Physics of the medium

1-1-1 Basics of acoustics

Since the key technology in this report is acoustic levitation, acoustics need to be well understood. This subsection will highlight some key points that are needed to understand acoustics and what happens to the medium when an acoustic wave is present. Extra focus will be put on ultrasound frequencies propagating through air as this is the most relevant for this paper. Ultrasound is sound with a frequency higher than 20kHz, which makes it inaudible to human hearing.

Acoustics derived from conservation of mass and momentum To get to a workable equation and understanding of acoustics, this chapter will show the derivation of the equations of mass and momentum to a simpler equation. Sound in its essence results from a time-varying perturbation of the dynamic and thermodynamic variables that describe the medium [11]. Small variations in velocity, pressure and density compared to steady reference values. The variations in density and pressure can be assumed isentropic and the flow compressible [12]. Isentropic means that the flow is both adiabatic and reversible.

Starting with the equations for conservation of mass and momentum for a moving single-component of viscous fluid as presented by Kundu et al [12] and shown in Equation 1-1 and

Equation 1-2, respectively. Where ρ, p and u are the fluid density, pressure and velocity respectively. τ_{ij} is the viscous stress tensor. The terms i and j stand for XXX. Added source terms q and f, are an unsteady volume source distribution and an unsteady body-force distribution respectively [12]. These terms can account for acoustic sources such as a transducer and are often described in the initial and boundary conditions [12].

$$\frac{1}{\rho}\frac{D\rho}{Dt} + \frac{\delta u_i}{\delta x_i} = q(x_i, t) \tag{1-1}$$

$$\frac{Du_j}{Dt} + \frac{1}{\rho}\frac{\delta p}{\delta x_j} = g_j + \frac{1}{\rho}\frac{\tau_{ij}}{\delta x_i} + f_j(x_i, t) \tag{1-2}$$

If the flow is assumed isentropic, an equation of state for the pressure $p = p(\rho, s)$ can be used. A equation for the pressure can be constructed from this under the assumption of constant entropy (setting Ds/Dt at 0) and using the relation between p, ρ and c as given in Equation 1-3. The first assumption can be made since the irreversible entropy production is proportional to the squares of the velocity and the temperature gradients, which are negligible for weak waves [12][13]. This would not be the case with, for example, shock waves. Furthermore, entropy fluctuations occur mainly as an effect of heat transfer or chemical reactions, which are both assumed to be negligible for the relevant application in this report. The subscript s indicates that the derivatives are taken at constant entropy.

$$c^2 \equiv (\frac{\delta p}{\delta \rho})_s \tag{1-3}$$

$$\frac{Dp}{Dt} = (\frac{\delta p}{\delta \rho})_s + (\frac{\delta p}{\delta s})_\rho \frac{Ds}{Dt} = c^2 \frac{D\rho}{Dt} \tag{1-4}$$

Using Equation 1-3 and Equation 1-4 a general wave equation for the pressure can be constructed from Equation 1-1 and Equation 1-2 [12] under the assumptions that the steady body force is spatially uniform, thus $\frac{\delta g_j}{\delta x_j} = 0$. The term τ_{ij} is often ignored unless the acoustic frequency is very high or the propagation distance is very long [12][13], thus τ_{ij} is set at 0. This general wave equation for the pressure is given by Equation 1-5, of which the derivation, as presented by Kundu et al., is given in the appendices section A-1.

$$\frac{D}{Dt}(\frac{1}{\rho c^2}\frac{Dp}{Dt}) - \frac{\delta}{\delta x_j}(\frac{1}{\rho}\frac{\delta p}{\delta x_j}) = \frac{Dq}{Dt} - \frac{\delta f_j}{\delta x_j} + \frac{\delta u_i}{\delta x_j}\frac{\delta u_j}{\delta x_i} \tag{1-5}$$

To be able to solve Equation 1-5 a common practise simplification is made. The dependent field variables are separated into nominally steady and fluctuating acoustic values as shown in equations 1-6[12]. The fluctuating values are considered small compared to the nominal values.

$$u_i = U_i + u_i', \quad p = p_0 + p', \quad \rho = \rho_0 + \rho', \quad T = T_0 + T' \tag{1-6}$$

The pressure can be Taylor expanded around a reference thermodynamic state specified by p_0 and ρ_0 shown in Equation 1-7. In which the the second-and higher-order terms can be neglected under the condition given in Equation 1-8 [12][11].

$$p = p_0 + p' = p_0 + (\frac{\delta p}{\delta \rho})_s \rho' + \frac{1}{2}(\frac{\delta^2 p}{\delta^2 \rho})_s \rho' + ... \tag{1-7}$$

$$\frac{p'}{\rho_0 c^2} << 1 \tag{1-8}$$

Normal acoustic-pressure magnitudes are in the order of magnitude of 1 Pa. A loud noise with a sound pressure level (SPL) of 120dB can even cause immediate hearing damage. A SPL of 120dB converts to a acoustic-pressure of just 20Pa. Even though pressure amplitudes for the transducer arrays in this paper can in the order of magnitude of 10^3, which is incredibly loud, the perturbations are quite small. This means that the density change is small and the condition given in Equation 1-8 holds. Ignoring the second-and higher-order terms of the pressure, a simple relationship between acoustic pressure and density fluctuations exists 1-9 [12].

$$p' = c^2 \rho' \tag{1-9}$$

One can insert Equation 1-7 into Equation 1-5 and linearize with the assumed time-invariant and spatially uniform terms U_i, p_0, ρ_i and T_0. The result is the equation for acoustic pressure in a uniform flow, shown in Equation 1-10 [12].

$$\frac{1}{c^2}(\frac{\delta}{\delta t} + U_i \frac{\delta}{\delta xi})^2 p' - \frac{\delta^2 p'}{\delta x_i \delta x_j} = 0 \tag{1-10}$$

Assuming a stationary fluid, and using the same simplified and linearized assumptions made earlier. One can also get a relationship between acoustic pressure and fluid velocity [12].

$$u'_j(x,t) = -\frac{1}{\rho_0} \int \frac{\delta p'}{\delta x_j} dt \tag{1-11}$$

Ideal gas Previous equations are derived under the assumption of constant entropy, as has been explained. Particles do undergo a temperature change but not due to heat transfer. The temperature fluctuations are due to adiabatic expansion or compression. Thus the entropy of a fluid particle can be assumed to be constant while a weak wave passes. This is because the entropy are the squares of the velocity and the temperature gradients [12]. If assumed a perfect gas, there are some useful relations between the pressure, density and temperature [12]. In which the pressure p, the density ρ, the temperature T in K and R the specific gas constant.

$$c = \sqrt{\frac{\gamma p}{\rho}} = \sqrt{\gamma R T}, \quad \frac{p}{\rho} = RT \tag{1-12}$$

Waves Since now the basics of acoustics have been covered it is useful to also get a visual understanding of waves. This can be done by looking at waves on a flexible string. It is easiest to first visualize a travelling wave after which the step can be made to understanding a standing wave. The flexible string is often used to understand acoustics and is in particularly based on the examples given in book Understanding Acoustics by Steven L Garret [14].

Take a flexible string, as can be found in a guitar string for example. This flexible string is visualized in Figure 1-1a. There is no bending stiffness (flexural rigidity) and the string has a constant linear mass. This implies that the string can only apply forces to influence the motion, produced by tension T [14]. The displacements y, are assumed small enough, thus the influence on the tension is second-order and can be neglected in a linear analysis. Furthermore, the boundary conditions are that y(0,t) = y(L,t) = 0.

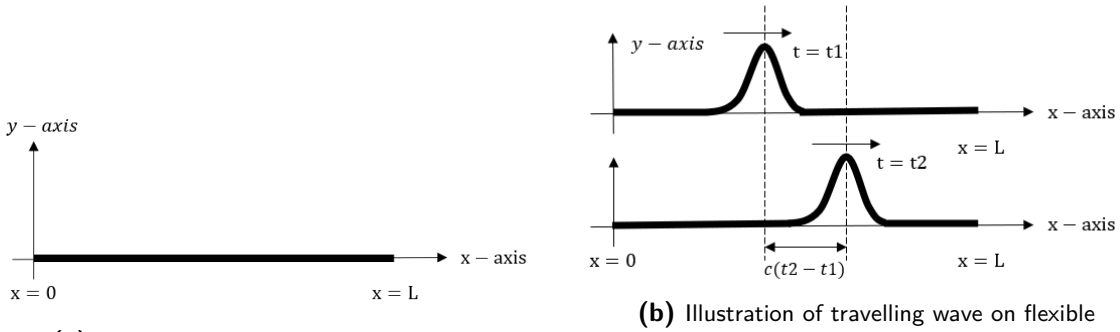

(a) Illustration of flexible string of length L

(b) Illustration of travelling wave on flexible string

Figure 1-1: Illustration of flexible string with and without travelling waves

A solution to the flexible string is shown in Equation 1-13. As a function it is useful to choose a complex exponential, shown in the same equation. A wavelength λ is defined that propagates to the right. This is illustrated in Figure 1-1b, where t2>t1. With spatial coordinates x and y. This figure illustrates a travelling wave. The wavelength and wavenumber can be related with Equation 1-14.

$$y(x,t) = f_{-}(ct - x) + f_{+}(ct + x) = |\boldsymbol{y}|cos(\omega t \pm kx + \phi) = Ae^{j(\omega t - kx)} \tag{1-13}$$

$$\lambda = \frac{2\pi}{k} \quad c = \lambda f = \frac{\omega}{k} \tag{1-14}$$

Standing waves The standing wave can be considered the superposition of two traveling waves [14] or plane waves travelling in opposite directions. The amplitude envelope is fixed in space, although the transverse displacement varies sinusoidally in time [14]. Nodes exist on the locations where the $sin(k_n x)$ term is zero. To show a real world example, with two opposite facing transducers, the amount of nodes n is dependent on the frequency and distance between the two transducers. Both of these variables are usually known for an opposite facing transducer pair. The exact locations of the nodes is also dependent on the phase of the signals both transducers, as this will determine where the interference will take

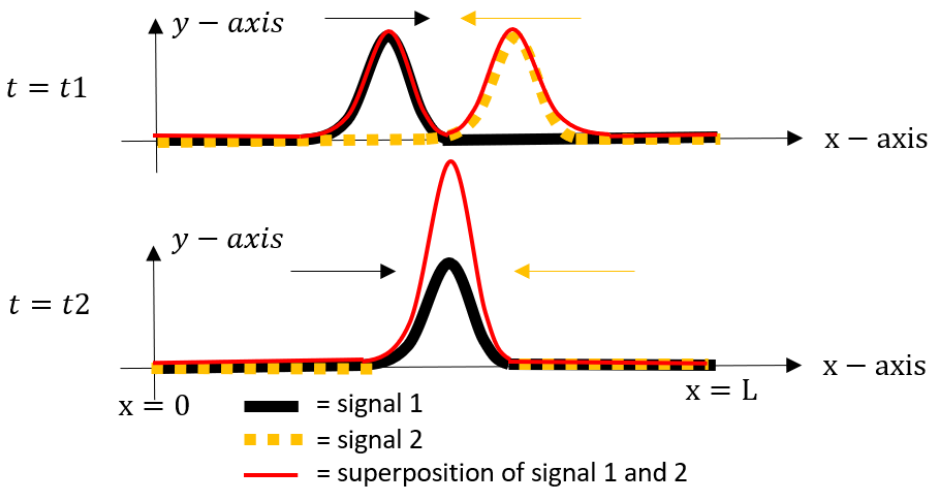

Figure 1-2: Constructive interference illustrated on a flexible string

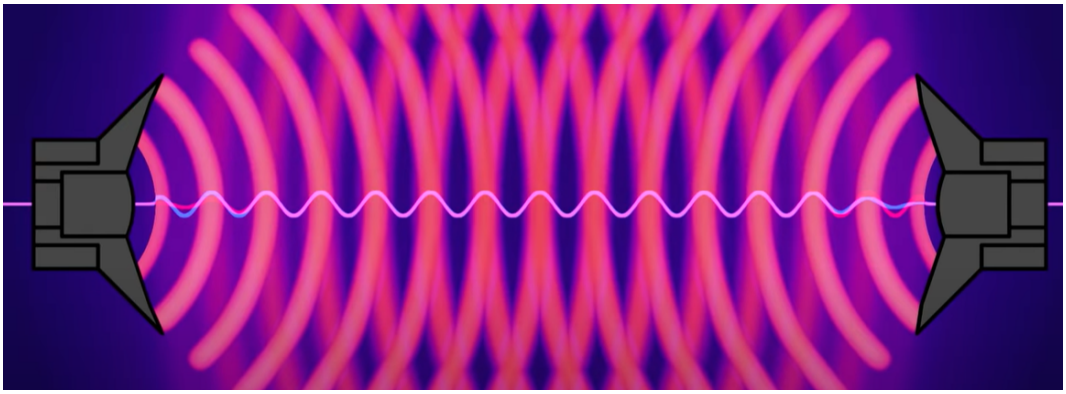

(a) Constructive interference [4]

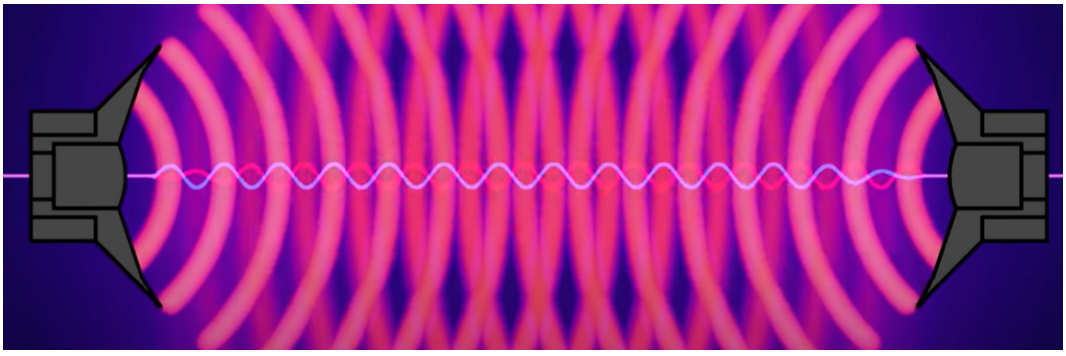

(b) Destructive interference [4]

Figure 1-3: Illustration of constructive and destructive interference of waves

place. This is illustrated in Figure 1-3a and Figure 1-3b. The superposition of the two signals can thus be higher than the individual signal, which is illustrated in Figure 1-2.

As can easily be demonstrated with a one-dimensional system, such as a string, the nodes

and anti-nodes stay fixed in space. In Figure 1-4, the amplitude is shown varying with time, indicated by a sin-wave with different colors. The nodes, indicated with red dots are the locations where the sin is zero, while the anti-nodes (black) are the locations where the sin is at its maximum or minimum. At these black points, the waveform undergoes constructive interference. Note that the only values for the sin wave are shown between the interval of [0 π].

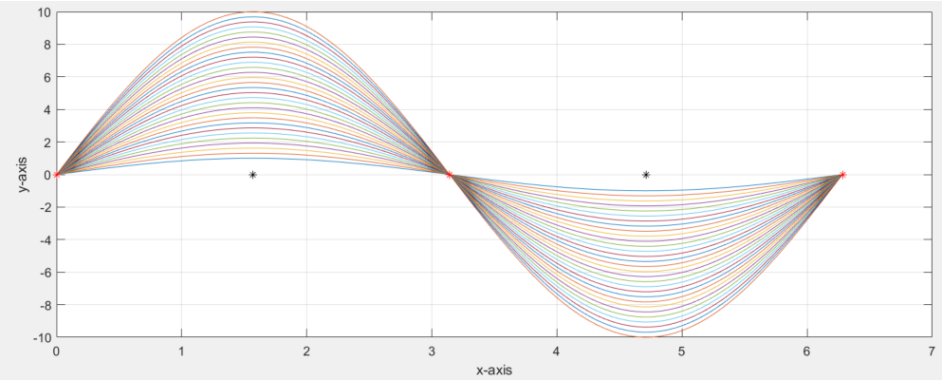

Figure 1-4: Nodes and anti-nodes illustrated

1-1-2 Effect of acoustics on refractive index

If one wants to detect pressure gradients in a medium by looking at the effect it has on light, the refractive index and the change in refractive index are important items to understand. This section will explain the connection of acoustics and refractive index. With an ultrasound wave causing a small disturbance with respect to the nominally steady refractive index, it could be written down like Equation 1-15 [15]. Where n_0 and n_1 are the mean refractive index of the medium and the maximum variation of the refractive index respectively. Both of these at a location $\boldsymbol{r}$ and at time t. What δ and n_1 depend on is a complicated matter which will be touched upon here, but a simplification will also be given useful for the use cases in this thesis. Ideally the refractive index could be written as a function related to the sound produced by the transducers.

$$n(\boldsymbol{r}, t) = n_0 + \delta n_1(\boldsymbol{r}, t) \tag{1-15}$$

Refractive index as a function of density in any medium As explained in subsection 1-1-1, an acoustic wave can be described with small perturbations of pressure. Looking at the refractive index is one way of detecting a change in pressure. The refractive index of a medium is a measure of how much light is slowed down as it passes through that medium. It is defined as the ratio of the speed of light in a vacuum to the speed of light in that medium. Pressure, among other things influence the refractive index. The refractive index of air is affected by a number of factors, including temperature, pressure and density. The concentration and humidity are assumed to be constant, together with temperature as discussed in subsection 1-1-1.

For an isotropic, dielectric material such as water the refractive index $n(\boldsymbol{r},t)$ may be described as Equation 1-16 [16] [17]. Where n, the refractive index is given at time t and location $\boldsymbol{r}$. With ambient and local density ρ_0 and ρ. χ is the intrinsic susceptibility of the material and ϵ_r the relative permittivity. The idea is that in a dielectric material the dominant chargers in atoms and molecules are bound, and are thus not free to move. With this assumption a change in permittivity will correspond with the number of molecules per unit volume of the medium [16]. The number of molecules per unit volume is related to the density of a material which gets perturbed if an acoustic wave is present.

This can be explained by the looking at the refractive index is as a function of permittivity and thus dipole moment per unit volume. And thus in a dielectic material a function of density [16]. In a region of higher density, an increase in refractive permittivity and thus refractive index is expected. This results in slower light speeds in this high density region.

$$n(\boldsymbol{r},t) = \sqrt{\epsilon_r} = \sqrt{1+\chi\rho(\boldsymbol{r},t)/\rho_0} = \sqrt{1+\chi}\sqrt{1+\frac{\chi}{\rho_0(1+\chi)}(\rho(\boldsymbol{r},t)-\rho_0)} \tag{1-16}$$

A Taylor series expansion of Equation 1-16 gives Equation 1-17 [17]. This indicates that the refractive index is mainly dependent on density. Under certain assumptions, however, this can be rewritten to make the refractive index mainly dependent on pressure [17].

$$n(\boldsymbol{r},t) = n_0 + \frac{n_0^2-1}{2p_0n_0}(\rho(\boldsymbol{r},t)-\rho_0) \tag{1-17}$$

Refractive index as a function of pressure If a medium, such as water, is assumed isotropic the change in refractive index is mostly dependent on pressure. Thus, Equation 1-17 can be written as Equation 1-18 [17]. The assumption is made that the medium is isotropic and dielectric while the behavior of the processes in this medium are isentropic (adiabatic and reversible). It is also assumed that the amplitude of the ultrasound waves is small. Making these assumptions the over-density $\rho(\boldsymbol{r},t) - \rho_0$ can be related to the over-pressure of the ultrasonic wave $p(\boldsymbol{r},t)$ through a coefficient [17][18].

$$n(\boldsymbol{r},t) = n_0 + \frac{n_0^2-1}{2n_0\rho_0c_0^2}p(\boldsymbol{r},t) \tag{1-18}$$

To get a feeling for what the sensitivity is of the refractive index, the adiabatic piëzo optic coefficient $\frac{\delta n}{\delta p}$, can be calculated. The following values are filled in for ultrasound in air: $n_0 = 1.0003$, $\rho_0 = 1.225\ kg/m^3$ and $c_0 = 343$ m/s. $\frac{\delta n}{\delta p} = 2.032\times10^{-9}Pa^{-1}$. With a sound pressure level (SPL) of about 3000 Pa this results in maximum perturbation of refractive index of $6.0946\times10^{-6}Pa^{-1}$.

Refractive index as a function of pressure in a gas The refractive index, in a transparent homogeneous medium, is a function of only the density and can be obtained by Equation 1-19 [7].

$$\frac{n^2-1}{\rho(n^2+2)} = constant \tag{1-19}$$

For gases, in which $n \approx 1$, Equation 1-19 can be simplified. It is reduced down to Equation 1-20 in which K is the Gladstone-Dale constant. This constant K relates the refractive index to density according to the similarly named Gladstone-Dale relation Equation 1-20 [5][19]. This simple linear relationship is only valid for gases and weakly dependable on wavelength and temperature [7]. For air, $K = 0.23\,\mathrm{cm}^3/\mathrm{g}$ for normal visual light wavelengths [5]. One can see from Equation 1-20 that n is only weakly dependent on density ρ. If the pressure is assumed constant and the ideal gas equation of state hold, the refractive index can be written containing pressure using Equation 1-12 [7].

$$n = 1 + K\rho = 1 + K(\frac{p}{RT}) \tag{1-20}$$

If one simply takes Equation 1-20 and calculates $\frac{\delta n}{\delta p}$ it comes around to $2.73 \times 10^{-9} Pa^{-1}$.

It is assumed that, even for the high local pressures produced by the transducer arrays relevant for this report, the ideal gas law and therefor Equation 1-20 holds.

1-1-3 Non linear acoustics

As the ultrasonic acoustic wave travels through the medium it changes the pressure. This local change in pressure also changes the local temperature. A local change in temperature, locally changes the speed of sound. This affects the frequency and introduces non-linearity [12]. As a sinusoidal wave, of a single frequency, travels through the air, the points of high pressure will travel faster than the points of low pressure. This results in self-distortion of the wave and the introduction of other frequency components. The higher harmonics are not caused by the transducer surface [1] and have a noticeable effect on the levitated particle [20]. A Laser Doppler Vibrometer (LDV) is used to measure the acoustic field. In Figure 1-5(a) the fundamental frequency and associated pressure nodes are displayed. In Figure 1-5(b) the second harmonic is displayed. It is important to note that, while the fundamental frequency has a node (minimum) at point +2, the second harmonic has a maximum here [1].
Using a low acoustic pressure, near the minimum acoustic potential, the behavior of the particle can be described as a spring-mass system [20]. In this condition the particle will oscillate harmonically from the equilibrium position. However, if a higher acoustic pressure is applied there is a energy transfer to higher order harmonics [21].

1-1-4 Acoustic streaming

The introduction of pressure gradients as a result of acoustic waves will also come with an effect called acoustic streaming. While the details of acoustic streaming are out of scope, a short overview will be given. Rayleigh streaming is a form of time-averaged fluid flow that exists in the viscous interaction between a solid surface and an acoustic wave [22].Rayleigh streaming is a viscosity effect, caused by attenuation and energy dissipation at the interfaces between the medium and the surface of the levitated particle [18]. Another form of streaming

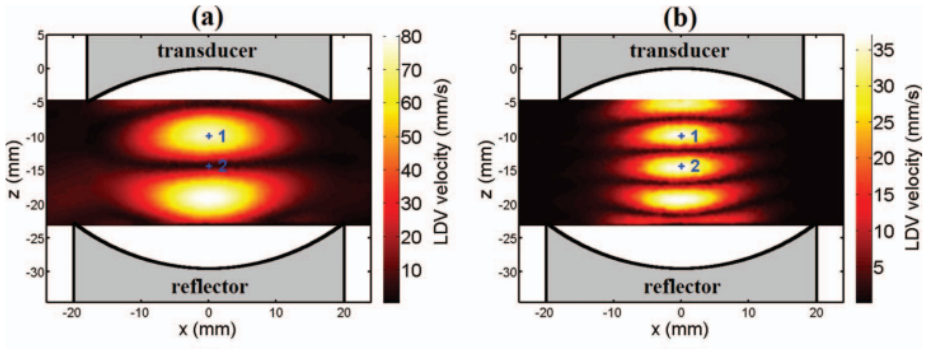

Figure 1-5: Sound field in (a)fundamental frequency and (b)second harmonic taken from [1]

can be observed with ultrasonics, Eckart streaming or so called 'quartz wind', which has been observed in water and air[18]. Rayleigh streaming is an energy dissipation within the Stokes boundary layer to an adjacent solid boundary, while Eckart streaming occurs within the main body of the medium [18][23].

Acoustic streaming can be a cause of spontaneous oscillations [2] and rotations of the levitated particle [18]. This can cause uneven heating of the levitated particle and cause mass and heat transfer. In this paper the attention is mainly focused on levitating solid particles. Dealing with internal circulation in a levitated drop is considered outside of scope. Thermal flow fields are strongly influenced by sound pressure level [2] but can also be caused by the heating induced by the sample or the container walls. The vortex-flow streaming happens outside of the boundary layer of the levitated particle in the standing wave field in air. The vortex-flow streaming causes velocity changes at distances proportional to the wavelength as can be seen in Figure 1-6. On smaller particles the motion is affected more by the drag force caused by acoustic streaming, while on larger particles acoustic radiation force mainly determines the motion. A visualization of streaming flows of a water droplet levitated in air can be seen in Figure 1-6a and Figure 1-6b.

1-1-5 Reflection of sound

Reflections of ultrasound waves will occur from objects placed along the path of the wave. In a transducer-reflector type setup, the reflections are essential to create a standing wave for particle levitation. For a phased array, reflections are not needed for the creation of a standing wave. The influence of reflections is dependent on the exact setup configuration. But Marzo et al. [24] states that not considering reflections in the design single axis, multiple transducer configuration still results a good correspondence between simulated and experimental levitation forces. Parasitic reflections can however be a source of unwanted noise on measurements of the acoustic pressure field. In the design of a pressure gradient visualisation setup this should be taken into account. Considering the surfaces and object to which sound can reflect greatly affect the standing wave field. Especially in a small container the ultrasonic standing wave field, wall propagation and reflection cause a complex standing wave field, which demands the model taking reflections into account [25].

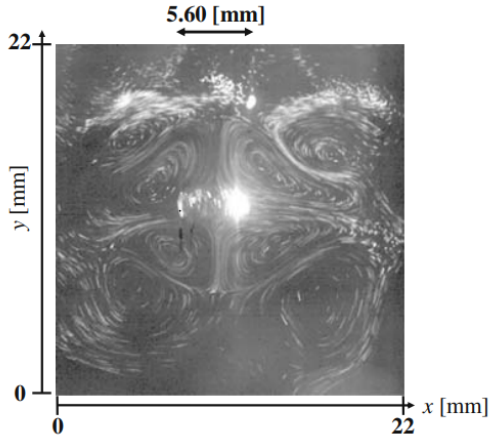

(a) The flow field around a water drop in reduced gravity conditions from [2]

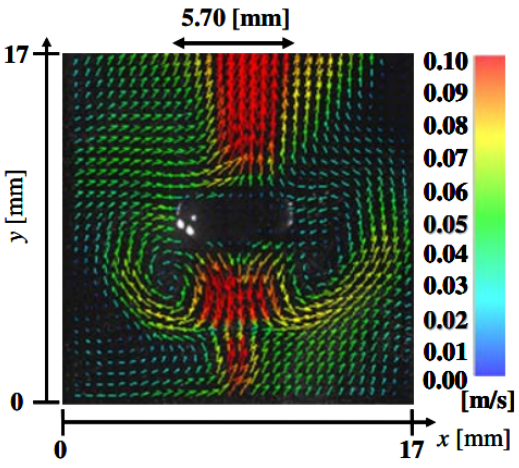

(b) The average velocity vector field around a water drop around 162dB taken from [2]

Figure 1-6: Flow fields around water drop in normal and reduced gravity conditions [2]

1-2 Physics of the levitating particle

1-2-1 Basics of acoustic levitation

Levitation of objects can be achieved using acoustics. An acoustic wave can exert forces on an object through the acoustic radiation force [26]. A standing wave can be generated by placing two transducers in opposite directions facing each other as shown in **??**. The two moving waves produced by both transducers will cause regions of constructive and destructive interference as is illustrated in (Figure 1-3a and Figure 1-3b). The standing wave oscillates with the same frequency as the ultrasound and pressure regions are formed at the areas of constructive interference. Although a standing wave is not necessary for acoustic levitation this method is the most popular method due to the trapping strength [27] and considered in this thesis. There are limitations regarding particle size and density with respect to the used frequency and the required acoustic power [27], details of which are considered outside the scope of this thesis. The regions of nonzero pressure that are created with a standing wave create an acoustic trap in which particles can be levitated. The levitation of the particle is achieved through the acoustic radiation force. The acoustic radiation force is dominant over effects such as thermal or viscous contributions for particle levitation [28]. Though these effects can have an effect on the stability of the particle, the acoustic radiation force is dominant [27].

The Gor'kov Potential The simplification of the forces acting on a particle inside an acoustic field is given by the Gor'kov potential shown in Equation 1-21. The assumption is made that the particle is much smaller than the wavelength, spherical and rigid. Only the incident acoustic field is taken to determine the forces on the particle [27]. Where U is dependent on V, the volume of the spherical particles, the frequency of emitted waves, ρ the density and c the speed of sound. Although the Gor'kov theory is applied succesfully in acoustic

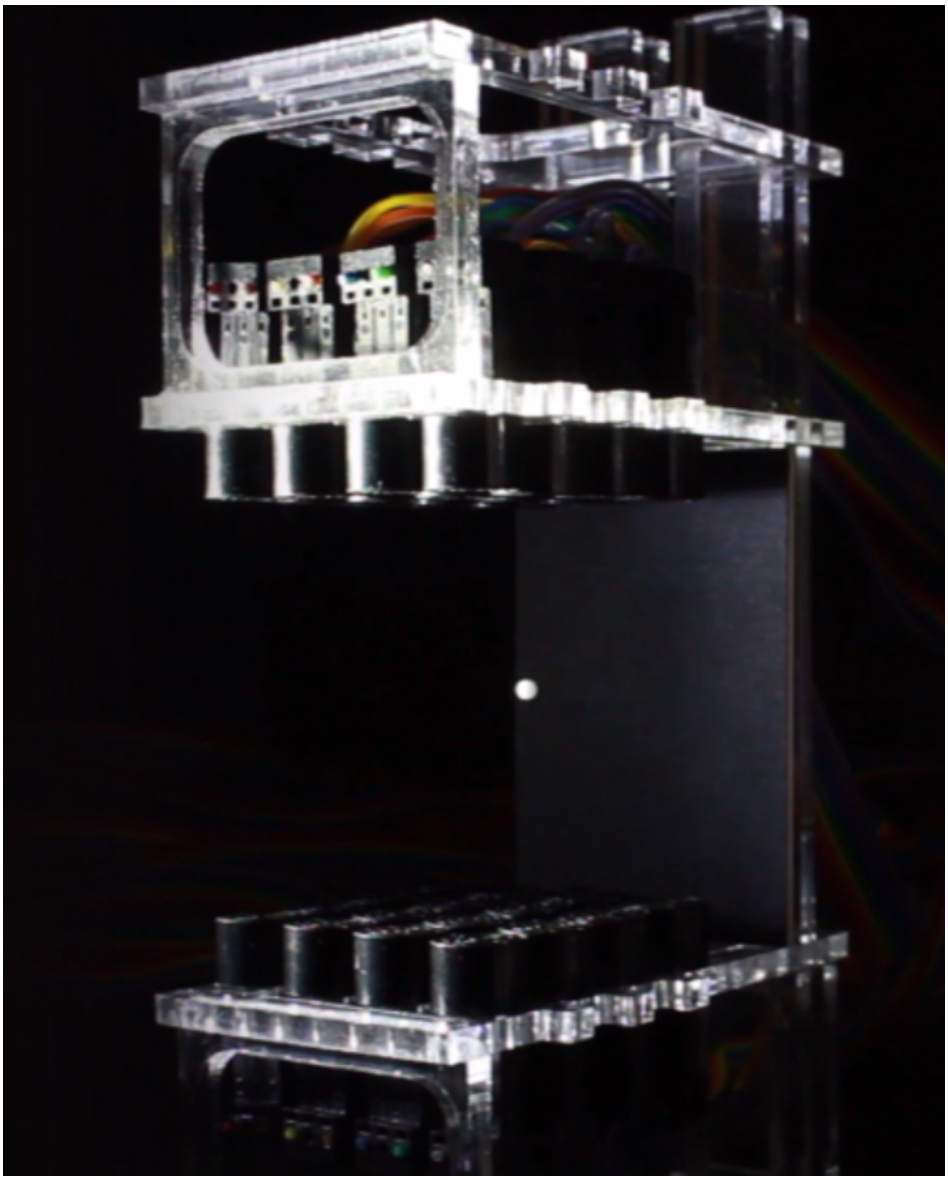

Figure 1-7: Acoustic levitation in Levipath [3]

levitators, there are some phenomena that cannot be explained, such as the oscillation of the levitated particle, harmonic generation and acoustic streaming. To calculate the potential for the acoustic radiation force, first a numerical method is used to determine the pressure and the velocity fields in the medium in which the levitation will take place. Then the obtained pressure and velocity fields are plugged into the Gor'kov equation (1-21) [20].

$$\boldsymbol{F} = -\nabla U \tag{1-21}$$

Where U can be defined in terms of incident pressure as shown in Equation 1-22 [27]. Where V is the volume of the spherical particle, ω the sound frequency, ρ the density (with subscripts 0 and s referring to the propagating medium and the particle material, respectively) and c

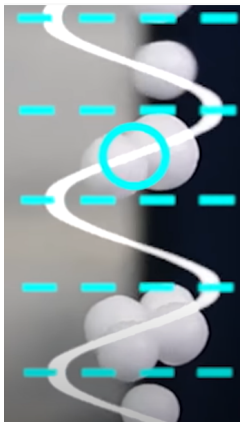

Figure 1-8: Sound pressure waves shown with acoustically levitated objects [4]

the speed of sound.

$$U = \frac{1}{2}V(\frac{1}{c_0^2\rho_0} - \frac{1}{c_s^2\rho_s})(|p|^2) - \frac{3V}{2}(\frac{\rho_0 - \rho_s}{\omega^2\rho_0(\rho_0 + 2\rho_s)})(|p_x|^2 + |p_y|^2 + |p_z|^2) \tag{1-22}$$

U can also be described in terms of pressure and velocity [29]. The velocity can be obtained through the gradients of pressure [29], thus both notations are fine. In the notation used in Equation 1-23, dimensionless expressions f_1 and f_2 are given in 1-24. Where the compressibility $\kappa_0 = \frac{1}{\rho_0 c_0^2}$ of the fluid is used [29].

$$U = V_p[f_1\frac{1}{2}\kappa_0\langle p_{in}^2\rangle - f_2\frac{3}{4}\rho_0\langle v_{in}^2\rangle] \tag{1-23}$$

$$f_1 = 1 - \frac{\rho_0 c_0^2}{\rho_s c_s^2} \qquad f_2 = \frac{\rho_s - \rho_0}{\rho_s + 0.5\rho_0} \tag{1-24}$$

A more general method to calculate the force acting on a particle without the assumptions used in the Gor'kov potential one should look into the radiation flux integral [27], which is outside of scope of this report.

1-2-2 Oscillations

Both liquid and solid acoustically levitated particles can oscillate around a certain equilibrium. Since there is a focus in this thesis on very accurate acoustic levitation, any spontaneous oscillations are undesired. Two types of oscillations can be identified: small spontaneous oscillations, caused by the interaction of the acoustic field and the levitated particle and large induced oscillations, caused by external forces such as thermal streams or a drift in the medium.
The frequency at which this oscillation occurs is influenced by multiple factors. The oscillation frequency in the axial direction is different from the frequency in the lateral direction, which indicates that the Gor'kov potential is different in each direction [20]. The oscillating frequency is also dependent on the acoustic pressure[30]. For a solid particle especially, since it

does not change shape, particle density has an influence on the oscillation frequency. Particle shape also has an influence on the oscillation frequency. With aspect ratio a/b, where a the lateral radius and b the axial radius. With an increase in the ratio a/b, the axial vibration frequency increases, which can be explained by the higher acoustic radiation force due to the shape.

Many causes of these oscillations have been identified in papers but determining which applies and the impact in each case is difficult. In a study, the frequency spectrum of the oscillations was analysed and in some cases the oscillations are at the fundamental frequency of the acoustic transducer, but in some cases at a much lower frequency [20]. At lower pressure amplitudes the motion of the particle behavior can numerically be predicted fairly well. At higher pressure amplitudes, however, non-linear effects appear [20].

1-2-3 Rotation

Just like oscillations acoustically levitated objects can rotate, both spontaneous and induced. An object has three principle axis and therefor three axis of rotation with three moments of intertia.

The spontaneous oscillations in an axis symmetric levitator are often around the axis of symmetry. Rotation of acoustically levitated liquids, with a much higher viscosity than air, can be rotated through viscous torque [31]. The working principle for acoustically levitated thin-films in air seems be the acoustic torque produced by coupling of acoustic radiation and asymmetry in the levitated object [32]. A paper in which rotational control has been achieved for thin-film samples in a single axis acoustic levitator, by varying pressure up with a rotational stability of $12 \pm 5\mu m$. It was found that the increase in pressure also caused an increased rotational speed.

1-2-4 Particle Movement

In a single axis acoustic levitator particles can be moved by shifting the phase of the opposite facing transducers such that the standing wave position changes. With a phased array this can be done in three dimensions. The phase of each transducer is calculated to form a node in a desired levitation position. The phase of each transducer determines the complex pressure at each location in the volume between the phased arrays as is shown in Equation 1-25 [33]. In which P_0, A, ω and k stand for the constant for transducer amplitude power, transducer phase, peak-to-peak signal amplitude and wave number, respectively. The transducer phase delay is ϕ. The far field directivity function D_f is dependent on the angle θ to the normal vector from the transducer surface. The directivity function can be simplified to Equation 1-26 [33]. Distance d is needed for divergence of the pressure amplitude. The pressure at one point in space is the contribution of each single transducer to that point as can be seen in Equation 1-27.

$$p(\mathbf{r}, t) = P_0 A \frac{D_f(\theta)}{d} \exp i(\varphi + \omega t + \phi)) \tag{1-25}$$

$$D_f(\theta) = sinc(ka \cdot sin(\theta)) \tag{1-26}$$

To move the particle levitated inside this position or node, the phase change for each transducer can be calculated to gradually shift the node to along a path. As the pressure field and thus the Gorkov potential is moved around the particle, an equilibrium at a new location will be sought.

$$p(\mathbf{r},t) = \sum_{n=1}^{n=N} Ae^{i(k\mathbf{r}+\omega t+\phi)} \tag{1-27}$$

1-2-5 Multi object levitation

Levitation and simultaneous movement of multiple objects has been achieved many times and is still an ongoing area of research [34][35]. Multiple objects can be levitated in the same trap, though this of course does not allow the individual control of each object. In a typical 1D acoustic levitator multiple nodes exist above each other along the degree of movement. In many of these nodes, dependent on acoustic pressure, an object can be levitated. This however, does also not allow for individual control of each object. A flat double side phased array allows for the creation of nodes on many different locations simultaneously. Even if only setting the phases of each transducer for one node location, other nodes usually appear simultaneously. In these locations constructive interference occurs allowing the creation of a node and thus a possible levitation point. Optimally determining the phase of each transducer for multiple levitation points while maintaining high control-ability and trap quality is an ongoing area of research. Since the pressure at one point in space is determined by the contribution of all transducers, not all levitation points necessarily have the same pressure.

The following points can be taken into account for the design of a pressure gradient visualisation tool: the complexity of the acoustic field increases significantly as more independent traps are generated. This might decrease the quality of measuring a 3D field with a 2D view. The presence of multiple objects in the acoustic field might increase reflections also contributing to the complexity of the acoustic field.

1-3 Pressure gradient visualisation in transparent media

A variety of methods for visualising pressure gradients in transparent media exist. Factors such as the magnitude of the pressure gradient, the scale of the observed phenomena and information captured by the visualisation determine if a method is suitable. An overview of suitable methods for visualising an ultrasound standing wave will be presented in here. As described in subsection 1-1-1 an acoustic wave is a perturbation of pressure. With this perturbation of pressure some other changes occur in the medium. Besides changes in density and temperature, the index of refraction changes. Thus, measuring the index of refraction will allow the pressure field to be reconstructed which allows a pressure gradient to be calculated, under the assumption that the medium is an ideal gas.

Light is a very suitable method for detecting ultrasound. It is advantageous since it does not disturb the sound field or introduce nucleation sites [36]. Appropriate methods for detection and quantification of an acoustic field, with and without light, will be discussed later, in section 1-4. First, the interaction between light and ultrasound needs to be thoroughly understood, which will be presented here.

1-3-1 The interaction between light and ultrasonic acoustic waves

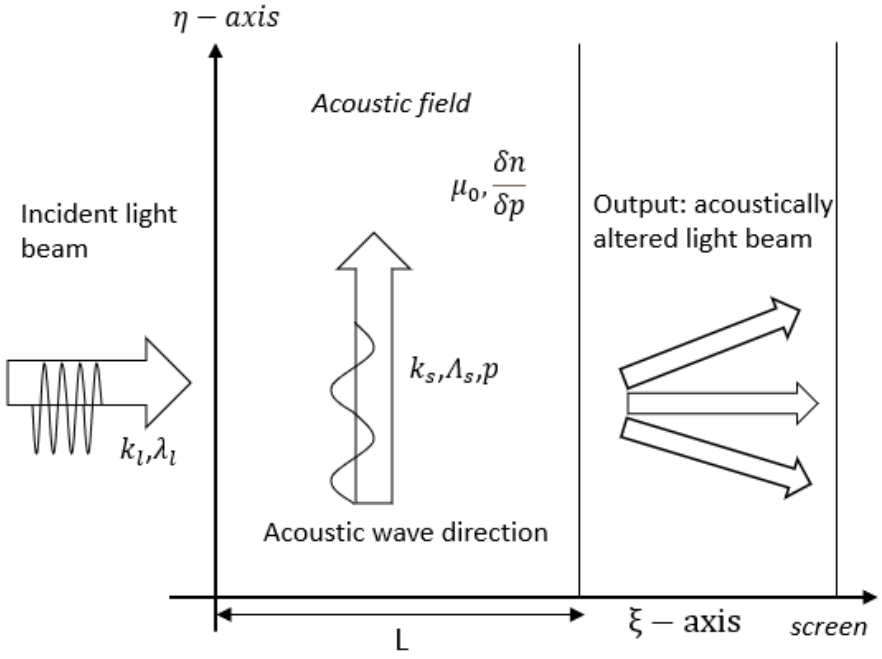

Figure 1-9: Setup for explaining the interaction of light by ultrasound

Take a incident light beam upon, parallel to the ξ-axis, and an acoustic field that parallel to the η-axis, as is illustrated in Figure 1-9. As discussed earlier in subsection 1-1-1 an acoustic wave will cause changes in pressure and thus refractive index in the medium. Dependent on the light wave length and sound frequencies, the interaction between light and sound can

be very diverse and effect how the light beam has changed upon the exit of the sound field. Sound waves can modulate the amplitude, deflect and shift the frequency of the light[37]. The physical phenomenon of scattering is dependent on the interaction of a beam of light with wavelength λ and a particle of size d_p, its characteristic dimension [38]. Different theories of light are needed to explain and understand different phenomena that can occur in the interaction of optics and acoustics. Broadly speaking, one could look at Equation 1-28 and divide this into 3 regions. If Equation 1-28 is $<<1$, ray optics apply. If near 1, wave optics apply and when $\gg 1$, quantum optics apply [38]. For normal green light, λ is around $550 \cdot 10^{-9}m$ (550nm). For a frequency of $40 \cdot 10^3$ Hz the wavelength in air is $8.6 \cdot 10^{-3}m$ (8,6mm). Thus ray optics apply in general. For ultrasound in the megahertz spectrum (10^6Hz) however, Equation 1-28 starts to get close to one where wave optics need to be taken into account. Both ray optics and wave optics will be discussed in this section.

$$\frac{\lambda}{d_p} \tag{1-28}$$

Besides the 3 regions in Equation 1-28, more parameters should be taken into account for the diffraction of light by ultrasound in different media. These are the Klein-Cook and Raman-Nath parameters, shown in Equation 1-35 and Equation 1-36 respectively [36].
The ability to understand what physics are dominant is important in comparing different frequencies and media throughout literature. Even though Equation 1-28 is a great start, the purview does not cover medium. More details will be given in a further paragraph.

Ray optics The simplest theory of light is ray optics. Light that travels different optical media is described by a collection of geometrical rules. Ray optics therefore is also sometimes called geometrical optics [39]. One of the first theories as what happens with light that is diffracted by ultrasound points at simple geometrical optics [15]. Parallel rays get refracted by a change in refractive index. If in the presence of an acoustic field, the change of refractive index is mainly dependent on the pressure.

The refractive index of a medium is defined in Equation 1-29. Where c_0 is the speed at which light travels in free space. Thus a medium with a refractive index higher than 1, will reduce the speed of the light to c.

$$c = \frac{c_0}{n} \tag{1-29}$$

If the assumption is made that an abrupt change in refractive index is present, the resulting angle with respect to the incidence light ray angle can be calculated using Snell's law [40][39], which is intended for refraction through discrete surfaces. A ray travelling through an acoustic field in gas will not come across a discernible surface, thus the assumption of an abrupt change cannot be made. To determine light ray trajectories through a graded index material one can use Fermat's principle, as shown in Equation 1-30.

$$\delta \int_A^B n(\mathbf{r}) ds = 0 \tag{1-30}$$

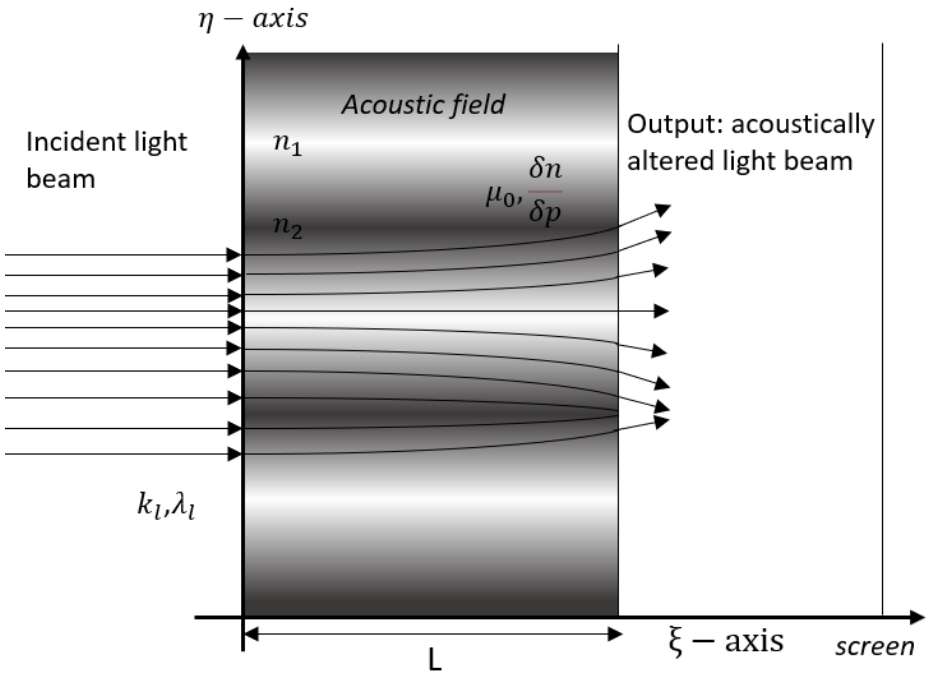

Figure 1-10: Rays of light bending as a result of a perpendicular sinusoidal varying acoustic field

Fermat's principle presents an accurate approximation of the light path s through a volume of inhomogeneous medium with refractive index $n(\mathbf{r})$ [39]. Where the components of $\mathbf{r}(s)$ are x(s), y(s) and z(s).

$$\frac{d}{ds}(n\frac{d\mathbf{r}}{ds}) = \nabla n \tag{1-31}$$

For the paraxial approximation, where the trajectory is almost parallel to the optical axis z Equation 1-31 can be simplified to Equation 1-32 [39].

$$\frac{d}{dz}(n\frac{dx}{dz}) \approx \frac{dn}{dx} \quad \frac{d}{dz}(n\frac{dy}{dz}) \approx \frac{dn}{dy} \tag{1-32}$$

Satisfying Fermat's principle (1-30) it can also be useful to look at the Eikonial equation 1-33 [39]. Which looks at the surfaces which the ray trajectories are normal to. The scalar function $S(\mathbf{r})$ is such that its equilevel surfaces are normal to the rays [39].

$$|\nabla S|^2 \approx n^2 \tag{1-33}$$

Wave Optics To understand more phenomena one needs to expand beyond the theory of simple ray optics. Diffraction of light by high frequency sound waves can occur under certain conditions which cannot be explained by ray optics. In ray optics light is described by the wave function [39]. Where the light is described as an optical wave $u(\mathbf{r}, t)$. The mathematical

details of which are out of scope of this report. Though, the linear equation is presented in Equation 1-34 as a starting point for further reading. Since the wave equation is linear, the principle of superposition applies [39].

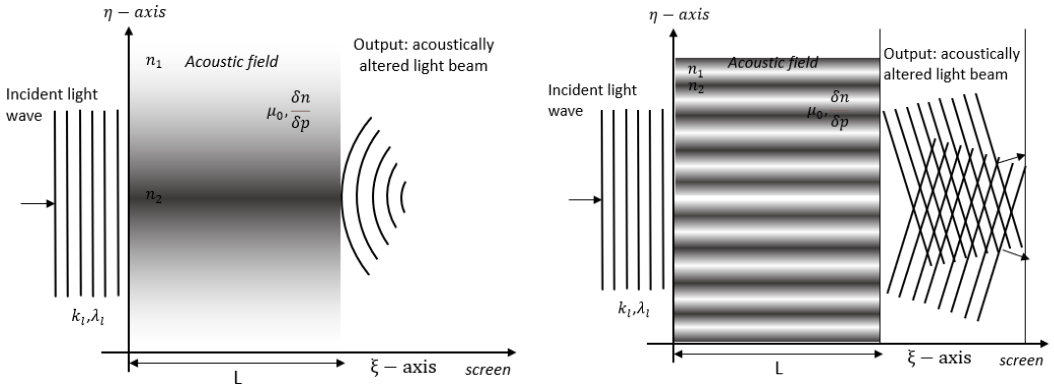

(a) Light waves as a result of a perpendicular low frequency sinusoidal varying acoustic field

(b) Light waves as a result of a perpendicular high frequency sinusoidal varying acoustic field

Figure 1-11: Light waves as a result of a perpendicular sinusoidal varying refractive index or acoustic field

$$\nabla^2 u - \frac{1}{c^2}\frac{\delta^2 u}{\delta t^2} = 0 \tag{1-34}$$

Wave optics do allow for the explanation of diffraction through diffraction gratings. Diffraction of light by high-frequency sound waves can occur [37] under certain conditions which will shortly be touched upon. As it can be seen in Figure 1-11a, a graded-index plate or volume can act as a lens, where the light is focused on a region with higher refractive index. This can be explained by a phase shift that occurs in the light wave. The phase shift, and thus the path in which direction the light waves are bend, depends on the thickness of the material or difference in refractive index [39]. Both cause a slight change in speed along a certain path through the medium compared to another path with different parameters. If more than one optical wave is present in the same region, the principle of superposition states that the total wavefront is the sum of the individual waves [39]. Constructive or destructive interference can occur, just as was explained in subsection 1-1-1. This interference can lead to diffraction patterns on the screen, where the light intensity is dependent on a multitude of factors. The idea of viewing the ultrasonic waves purely as phase grating originated in 1935 by Raman an Nath [41]. Who considered that initial parallel rays do not bend at all and only cause a phase delay, dependent on the refractive index of the region they go through [15].

The diffraction of light by ultrasound Multiple theories are explained in the book 'The diffraction of light by ultrasound' from Michael V. Berry, which will be briefly explained in the section below. Different forms of sound diffracted light exist, depending on the sound and light wavelength and the dimensions of the interaction [37]. As already explained in the previous subsection, the interaction of light and ultrasound, with relevant conditions for this project, can be explained with ray optics. These conditions are sound frequency at 40kHz and

visible light in air. However, with other conditions different phenomena can occur. If different acoustic wavelengths are required for an acoustic levitator, visualising and measuring these new wavelengths has to reconsider a suitable method. Getting a better understanding when these more difficult phenomenon occur and what factors influence them is explained in this subsection.

As is shown in Figure 1-9, parallel rays are incident on a liquid filled vessel of width L with ultrasound waves traversing parallel to the η-axis. The different theories aim to say something meaningful about the light intensity after ξ=L. Many different theories to explain the diffraction pattern exist, valid through a selection of boundary conditions. Though what the main conclusion is, is that using the scalar wave theory is sufficient and necessary [15] as it yields better results describing the light and the resulting diffraction patterns. It is important to highlight that there is a difference between a dynamic, time-varying, graded-index medium compared to a static one. The theory of acousto-optics deals with the propagation of light through a inhomogeneous medium with a time-varying perturbed refractive index [39]. Using a pulsed light source, driven with a similar frequency to the observed acoustics, one can assume a time-invariant graded-index medium.

If a thin beam of light is perpendicularly incident on an acoustic wave the acousto-optic interaction known as Raman-Nath or Deybe-Sears scattering occurs [39][37]. The more general case of incident light at an angle other than perpendicular is called Bragg diffraction [39][37], which is a phenomenon often used in acousto-optic devices. There are two types of analytical solutions for opto-acoustical diffraction. The first being Raman-Nath diffraction, the second being Braggs diffraction [42]. Raman-Nath diffraction can be expected when the Klein-Cook parameter, shown in Equation 1-35, is much smaller than 1 [43] [44]. While Braggs diffraction can be expected if the Klein-Cook parameter is much bigger than 1 [44].

A lot of literature about detecting pressure fields in ultrasound is written in the context of medical ultrasound. Often the frequencies are in the megahertz range and the medium that is often used is water. Another article investigates the usage of ultrasonic transducer phased arrays to steer a laser with the change in refractive index in Tellurium dioxide [30]. In order to compare these different combinations of ultrasound and light within a medium one should look into the dimensionless parameters. Two dimensionless parameters Equation 1-35 and Equation 1-36 are found to be important in the theory. With k, μ_0, μ_1, λ and Λ, the optical wave number, the mean refractive index of the liquid, the maximum variation of refractive index, the optical wave length and the acoustic wave length. The first dimensionless parameter, Equation 1-35, is the Klein-Cook parameter. Q is characterized by the square of the frequency and the sound field dept L [45]. The second parameter is known as the Raman-Nath parameter, which depends on the maximum variation of the refractive index, also known in liquids as the adiabatic piezo-optical coefficient or opto-elastic coefficient [46], the sound pressure amplitude p and the sound field dept L [47][45][48].

$$Q = \frac{2\pi\lambda L}{\mu_0 \Lambda^2} \tag{1-35}$$

$$v = k\mu_1 L \quad = k\frac{dn}{dp}pL \tag{1-36}$$

To get an idea of what ranges these parameters have they are displayed for multiple inputs. The first input in the situation that is most relevant for this paper, ultrasound of 40kHz in air. Possible future updates to an acoustic levitator with higher frequency is also accounted for. Another input is aimed at a well documented research field namely medical ultrasound. For this 1MHz and 20MHz in water will be taken. The calculated parameter values are shown in Table 1-1 and Table 1-2. The estimates for the maximum variation in refractive index n_1 can be calculated using the Gladstone dale constant (Equation 1-20) and the maximum pressure given in the table. The estimated values of $\frac{dn}{dp}$ for air and water correspond with the values used by A. Holm and H. W. Persson [46].

	kHz in air	kHz in air	kHz in air
Sound frequency	40KHz	40KHz	200KHz
Interaction length	10cm	0.5cm	1cm
Speed of sound in medium	343m/s	343m/s	343m/s
Wavelength of light	550nm	550nm	800nm
n_0	1.0003	1.0003	1.0003
Max pressure amplitude	3000Pa	3000Pa	3000Pa
Q (Klein-Cook parameter)	0.0047	0.0002	0.0085
v (Raman-Nath parameter)	9.372	0.4686	1.2887

Table 1-1: Dimensionless parameters important in diffraction by ultrasound for the kHz range in air

	MHz in water [47]	MHz in water [47]	MHz in Tellurium dioxide [30]
Sound frequency	1MHz	13MHz	75 MHz
L	21mm	21mm	1cm
Speed of sound in medium	1480m/s	1480m/s	4260m/s
Wavelength of light	632nm	632nm	632 nm
n_0	1.333	1.333	2.26
$\frac{dn}{dp}$	1.51810^{-10}	1.51810^{-10}	-
Sound pressure amplitude	≈ 0.0005Pa	≈ 0.0005Pa	-
Q (Klein-Cook parameter)	5.7	6.88	6.9
v (Raman-Nath parameter)	≈ 1.6	≈ 1.6	-

Table 1-2: Dimensionless parameters important in diffraction by ultrasound for the MHz range in water and Tellurium

Suitable parameters for the experimental setup discussed in this report are the first two columns of Table 1-1. The exact value of which will lay somewhere between the values calculated in the first two columns. This results from the difficulty to exactly estimate the the exact interaction length and maximum local pressure from a complex pressure distribution generated by an phased array .Despite high numbers for the Raman-Nath parameter the calculated value for the Klein-Cook parameter are sufficiently low. Since Q is much smaller than 1, there is weak acousto-optic interaction, and thus Raman-Nath regime can be assumed [43][44][48]. Multiplying Q and v also results in $Qv << 1$. Both criteria 1-37 are satisfied for Raman-Nath behavior to occur [49]. This indicates that it modelling the light is possible with a straight line undiffracted ray approach [49]. The criteria for Raman-Nath regime are given in 1-37 and can be easily described as the following; 1. The sound field is thin enough

to ignore optical diffraction effects and 2. the sound field is weak enough to ignore optical ray-bending effects [49]. The diffraction of light by ultrasound is outside the scope of this report and extensively documented [50][49].

$$Q << 1 \quad Qv << 1 \tag{1-37}$$

1-3-2 The interaction of light and a complex acoustic field

In the previous chapter the discussed interaction between light and ultrasound is centered on a plane wave, mostly perpendicular to the light. Using Equation 1-30 one can write the deflection angles through a three-dimensional graded index field, which is shown in Equation 1-38 [51][7].

$$\epsilon_x = \int \frac{1}{n(x,y,z)} \frac{\delta n}{\delta x} dy \qquad \epsilon_z = \int \frac{1}{n(x,y,z)} \frac{\delta n}{\delta z} dy \tag{1-38}$$

If the assumption is made that this field does not vary in the direction of the optical axis this reduces to a simplified notation given in Equation 1-39. In which L indicates the length of the varying refractive index along the optical axis. In the case of air, the local refractive index can also be simplified since $n(x,y,z) = n_0 \approx 1$.

$$\epsilon_x = \frac{L}{n_0} \frac{\delta n}{\delta x} \qquad \epsilon_z = \frac{L}{n_0} \frac{\delta n}{\delta z} \tag{1-39}$$

As mentioned in 1-2-1, in a phased array setup the amplitude and especially the phase of each transducer is varied to generate nodes in desired positions. Since the phase of each transducer might be different, the acoustic field should only be regarded as a superposition of all acoustic waves. This can result in quite a complicated pressure distribution as is shown in Figure 1-12. Adding to the complexity is also taking the reflections of the acoustic waves into account. This has not been modelled in Figure 1-12. Thus, the assumption of a two-dimensional field with constant pressure gradient over the optical axis is often wrong.

The interaction of the light with the pressure perturbed field remains the same as in a simple field, as the physics remain the same. There exists a challenge in mapping the complete and full 3D acoustic field. A simpler 2D representation will result in some loss of information.

1-4 Ultrasonic Pressure gradient visualisation methods

In this section relevant pressure gradient visualisation and qualification methods are highlighted. The main working principle of each method is explained. As most of these methods are used in a wide range of applications, the link with visualising and quantifying ultrasound from literature is also specified. The state-of-the-art with respect to measuring airborne ultrasound, in the context of acoustic levitation, is also mentioned.

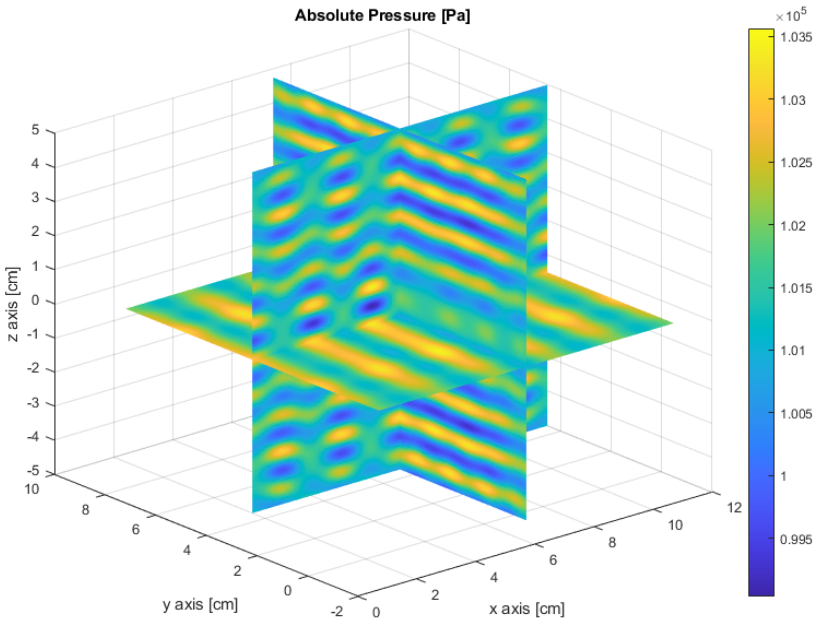

Figure 1-12: Modelled absolute sound pressure with 128 transducer phases set to 0, with an array located at the xy-plane z= -5 and z = +5

1-4-1 Shadowgraphy

The working principle of shadowgraphy has to do with the deflection of light as a result of a varying index of refraction in the test area. As discussed in subsection 1-1-2 a perturbation in the refractive index causes the light to deflect. Light originating from a point source, usually a pinhole, is projected through a test area onto a screen [51]. Without the presence of a perturbation in refractive index, light would illuminate the screen uniformly. But the perturbation causes some light rays to be refracted or deflected from their original path, contributing to extra illumination on its final location on the screen [51]. Adding a lens, as illustrated in Figure 1-13, causes the now parallel rays to be refracted. The refraction is caused by $\frac{\delta n}{\delta x}$ and $\frac{\delta n}{\delta y}$ as discussed in subsection 1-3-1 [51][7].

Thus a uniform gradient would not cause deviations from the parallel path and would not display a shadowgraph. The deflection angle ϵ is proportional to the refractive index gradients in the test area [51]. The intensity observed on the screen is proportional to the gradients of the deflection angle. Thus the observed shadowgraph displays a second spatial derivative of the refractive index $\frac{\delta^2 n}{\delta x^2}$ and $\frac{\delta^2 n}{\delta y^2}$ [38][51].

Using principles similar to shadowgraphy to visualise medical ultrasound in water have been used by by N. Kudo [52][53]. Using shadowgraphy successfully to visualise and quantify airborne ultrasound has not been attempted, since schlieren methods are often used. Schlieren relies on the same working principle but is mostly superior for this application and will be explained in the next subsection.

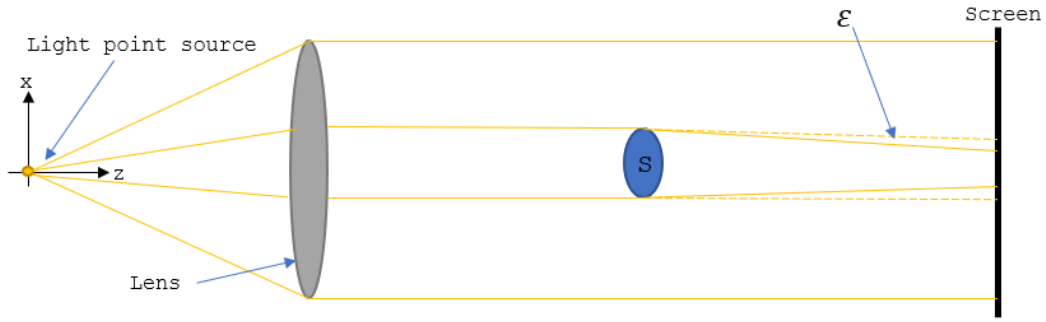

Figure 1-13: Illustration of direct shadowgraphy

1-4-2 Basics of Schlieren

The schlieren technique is an indication of the projection of light that is partially deflected by an object [51]. Though first observed in 1665 by Hooke, the classical schlieren system have been proposed in 1859 by Foucault and Toepler [54]. Schlieren photography has been widely used to observe phenomena in transparent media.

As with shadowgraphy, the working principle of schlieren has to do with the deflection of light as a result of a varying index of refraction in the test area. Light originating from a point source is projected through a test area where a perturbation in the refractive index causes the light to deflect. From this point on it is identical to shadowgraphy. The differences lays in what happens beyond this point, as can also be seen in Figure 1-14. The first of those difference being the presence of a cutoff, something that is partially blocking the refracted light. The second, the fact that the schlieren image is a focused image, while shadowgraphy is just a shadow. Finally, the illuminance level on the screen responds to the first spatial derivative of the refractive index in the schlieren while shadowgraphy responds to the second spatial derivative (or Laplacian) [51]. Though there are some advantages using shadowgraphy over schlieren, such as the ease of the setup. The main disadvantage however, is the lower sensitivity for weaker disturbances of refractive index [51].

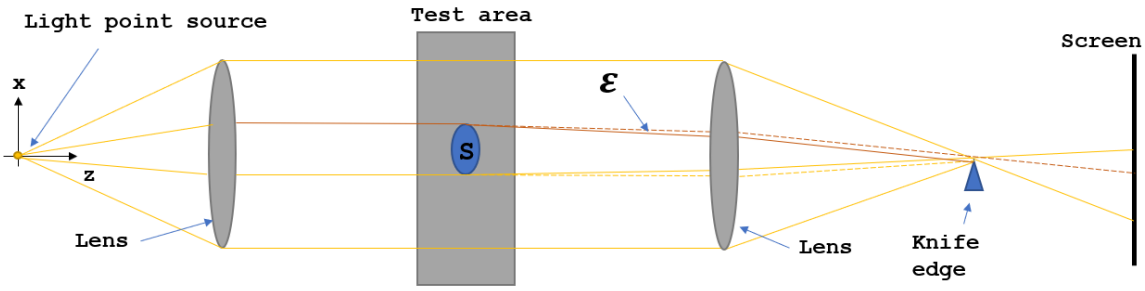

Figure 1-14: Illustration of basics of schlieren

Many different configurations of a schlieren setup for different applications are possible. In this report three setups will considered: the traditional two lens schlieren system, the Z-type setup (Figure 1-15) and the single parabolic mirror coincident setup (Figure 2-3). The Z-setup

Location in schlieren setup	Subscript
At source (slit)	s
At focus of second mirror without knife edge	0
At focus of second mirror with knife edge	k
At screen	d

Table 1-3: Overview of subscripts used

makes it easy to explain the fundamentals while the single parabolic mirror setup is used in practise due to the easy availability of a single mirror and the doubling of sensitivity due to a double pass through the test region. The working principles however are the same. The two lens system has the same working principle as the Z-type setup and allows easy visual comparison to shadowgraphy, as is shown in Figure 1-14.

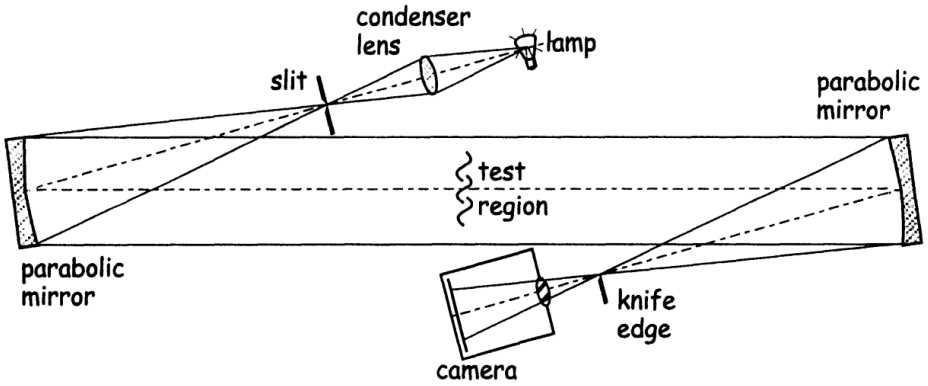

Figure 1-15: Z-type setup for Schlieren [5]

To get a better understanding of the working principles of schlieren and thus how a pressure perturbation is translated onto an image, one should look at the sensitivity. To calculate the sensitivity one can start looking at the illuminance. In the equations from the following section subscripts to refer to locations in the schlieren setup are used, for readability they are given in the overview presented in Table 1-3.

If one considers the Z-type setup, with light with luminance B (in $candela/m^2$) from the light source that is shown through a rectangular slit, with height h_s and breadth b_s. Using the inverse square law the illuminance at the first mirror can be calculated by Equation 1-40 [51]. Where f_1 represents the focal length of the first mirror from the light source. The illuminance in the source, denoted s, is given in Equation 1-40.

$$I_s = \frac{B \cdot b_s \cdot h_s}{f_1^2} \tag{1-40}$$

Assuming no losses, and thus that all the light falls on the test area and the second mirror, the illuminance in the abscence of any cutoff on the image is written in Equation 1-41. In which the magnification factor m accounts for the image size on the camera in comparison to the test area [51].

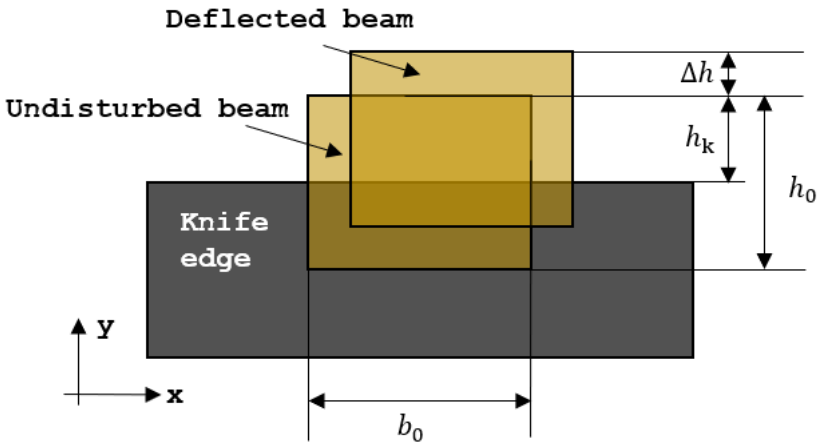

Figure 1-16: Deflected beam and undisturbed beam at the knife edge

The illuminance at the cutoff, without a knife edge present is denoted with subscript 0. The illuminance at the cutoff with a knife edge present is denoted with subscript k. If a knife edge obstructs part of the light of the undisturbed beam at the focus point of the second mirror the height of the part the light that is let through is h_k instead of h_0. This is also illustrated in Figure 1-16.

$$I_0 = \frac{B \cdot b_0 \cdot h_0}{m^2 \cdot f_1^2} \tag{1-41}$$

With the knife edge, located at exactly the focal point of the second mirror f_2 one can construct Equation 1-42 using Equation 1-43 [7]. Where f_2 is the focal length of the second mirror in the Z-type setup.

$$I_k = \frac{h_k}{h_0} I_0 \tag{1-42}$$

The illuminance at the screen or camera, denoted by d, which is located beyond the knife edge can be written as shown in Equation 1-44 [7]. As every schlieren setup has some level of background illuminance, the illuminance seen on the camera is compared to that level.

$$\frac{h_0}{h_s} = \frac{b_0}{b_s} = \frac{f_2}{f_1} \tag{1-43}$$

An initially parallel light ray coming from the first mirror through the test area gets refracted by a perturbation in refractive index. The refraction with angle ϵ and y-component ϵ_y causes part of the source image to shift with Δh. This small shift of the source image can be written as $\Delta h = \epsilon_y \cdot f_2$ [51][38]. Note that since the knife edge in Figure 1-16 is parallel to the x-axis, only the shift of the light beam in the y-direction affects the illumination on the screen [7].

$$I_d = I_k \frac{h_k - \Delta h}{h_k} \tag{1-44}$$

As mentioned above, the illuminance seen on the camera is with respect to some background illuminance. The ratio of differential illuminance is expressed as the contrast in the schlieren image, shown in Equation 1-45[51][38][7].

$$C \equiv \frac{\Delta I}{I} \equiv \frac{I_d - I_k}{I_k} = \frac{f_2 \varepsilon_y}{h_k} \tag{1-45}$$

The sensitivity of any instrument is often described as d(output)/d(input). Where the output is the contrast in the image, given by Equation 1-45. The input is the pattern of irregular ray deflections ϵ, resulting from perturbations in refractive index in the test area, in an otherwise regular beam of light [51]. The schlieren sensitivity, often called contrast sensitivity, is the rate of change of contrast with respect to refraction angle, shown in Equation 1-46[51].

$$S = \frac{dC}{d\varepsilon} = \frac{f_2}{h_k} \tag{1-46}$$

This equation gives a simple measure for schlieren sensitivity independent of any observing or recording means. It shows that sensitivity is dependent on the focal length of the second mirror in a z-type system and the unobstructed height of the source light that is let through. This equation however also gives the impression that one can reach infinite sensitivity with h_k going to zero, which is obviously not reasonable. To explain the limits of this formula one needs to take diffraction into account. That is out of scope for this report and usually a description with geometrical optics is sufficient [7][51]. Minimizing h_k would maximize the contrast, this will however limit the range for deflection of the beam, since all deflections that are the size of h_k or larger wouldn't give any illumination [7]. More on how to optimize a practical setup for sensitivity and a certain measuring range is explained in section 1-6.

Quantitative schlieren Besides just visualising pressure gradients schlieren can also help to quantify the observed phenomena. Even though the image contrast is correlated to the pressure gradient, analyzing image intensities is not the only way to quantify schlieren images. There are multiple ways which will be explained in subsection 1-6-4. Due to the refractive index varying slightly with wavelength it is preferred to use monochromatic light, although it not of major importance in schlieren systems [7]. Different wave lengths could however also be used to visualise both temperature and flow simultaneously in a schlieren setup [55].

Application to ultrasound The main downside of traditional schlieren methods is the need for high precision, and therefor, expensive optics. Luckily, the acoustic field produced within the levitator in this report and the accompanying mirror size diameter are not too large and thus affordable. In a quantitative study utilising schlieren the illumination or contrast has to be carefully analyzed, which is usually time consuming for the resulting accuracy [7]. In many quantitative schlieren measurements, the shock wave angle is an easy way to quantify instead of using image contrast [7]. Visualising ultrasound travelling waves and standing waves in water has been done many times [56][57]. Quantitative schlieren of ultrasonic waves in water has been achieved as well [58][59][60][61][62][63][53]. The visualisation of airborne ultrasound of a single transducer, of both the traveling wave and the reflection have been beautifully

demonstrated by A. Crockett and W. Rueckner [64]. Attempting quantitative schlieren measurements of single low kHz range ultrasound transducers have been done, but the study has a higher focus on shock waves instead of determining the local pressure gradient [65]. The visualisation of airborne ultrasound, using a 1D acoustic levitator, has also been achieved to successfully provide feedback on the acoustic cavity length [66]. Visualising airborne ultrasound generated by a phased array, with a pulsed light source has been achieved as well [67]. Using the same light frequency as the array frequency to visualise levitation traps while transducer heating was also noticed.

1-4-3 Background oriented schlieren

Background oriented schlieren (BOS) is a newer method that has recently gained in popularity due to advances in digital cameras [6]. Though similar to schlieren it does not heavily rely on optics, but on the readily available high quality digital camera's. This can be advantageous for some applications. A camera is aimed at a speckled background with a high spatial frequency and contrast [6]. Two images will be taken by the camera. One with and one without a disturbance between the camera and the background. Taking the two images and analyzing the displacement of the dots of the background the diffraction can be calculated. This is illustrated in Figure 1-17. The sensitivity and contrast depend mostly on the ability to detect a shift in the dots and therefor on the pixel density of the camera sensor. The absence of large optical instruments makes this method very suitable for observing large-field and outdoor phenomena such as helicopter blade-tip vortices [68], compared to traditional schlieren where hugely expensive optics would be required.

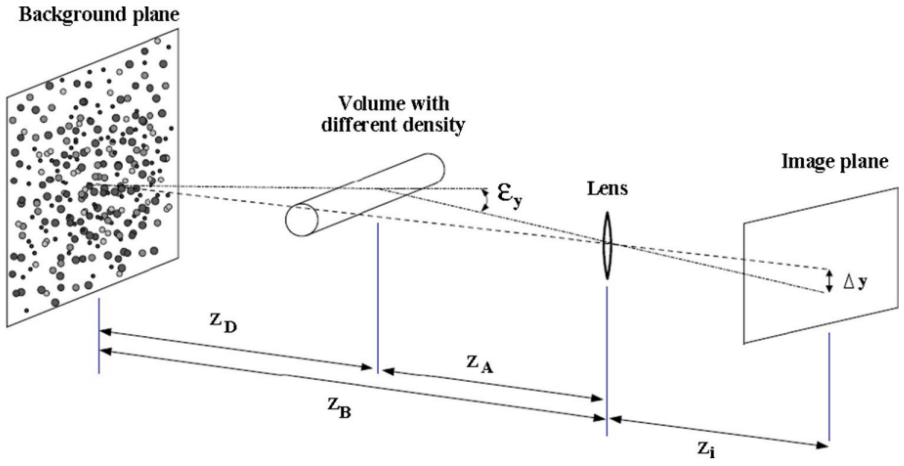

Figure 1-17: Illustration showing background oriented schlieren, from [6]

Looking at formulas is a great way to get a better grip on the working principles of BOS. The positive and negative aspects are understood more easily. With the aid of Figure 1-17, an overview of the main formulas for BOS will be given. Assuming paraxial recording and small angles for ϵ_y the image displacement Δ_y is given by Equation 1-47 [6].

$$\Delta y = Z_D M \epsilon_y \quad = f(\frac{Z_D}{Z_D + Z_A - f})\epsilon_y \tag{1-47}$$

With M the magnification factor of the background $M = \frac{z_i}{Z_B}$. Z_D the distance between the density gradient and the background dot pattern. Since a beam is dependent on the spatial gradient of the refractive index integrated along the complete length of the line of sight, the deflection angle can be written as Equation 1-48 [6]. Which is the same as Equation 1-38 under the correct assumption that $\frac{1}{n}$ does not change much since $n_0 \approx 1$ [7].

$$\epsilon_y = \frac{1}{n_0} \int \frac{\delta n}{\delta y} dz \tag{1-48}$$

Looking at Figure 1-17 with distances Z_A, Z_D and Z_i, the distance from lens to observed phenomenon, the distance from the observed phenomenon to the background and the distance from the lens to the image plane, respectively. To obtain maximum contrast for speckle tracking, the camera is focused on the background [69]. Applying the thin lens formula gives Equation 1-49.

$$\frac{1}{f} = \frac{1}{z_i} + \frac{1}{Z_B} \tag{1-49}$$

The problem with focusing on the background, which is usual practice, is that it results in not being able to sharply focus on the density gradients, which would be in focus at distance Z_i; [69][6]. This is illustrated in Equation 1-50.

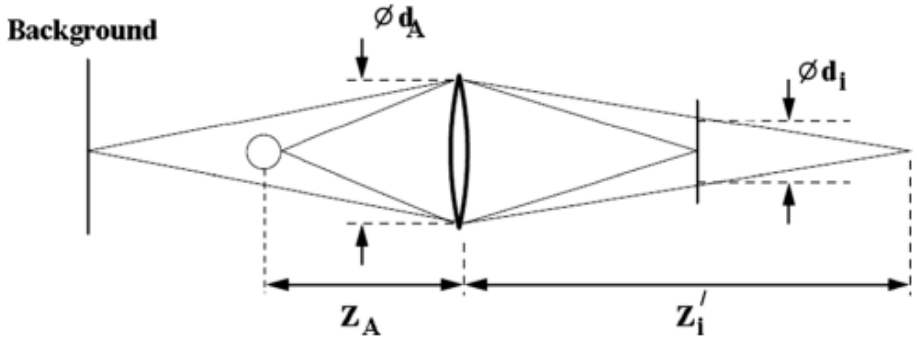

Figure 1-18: BOS focus on density gradient instead of backgound, from [6]

$$\frac{1}{f} = \frac{1}{Z_i'} + \frac{1}{Z_B} \tag{1-50}$$

In literature, aperture diameter d_A is introduced together with magnification of the density gradient $M' = Z_A'/z_A$ [69][6]. These result in a formula for the geometric blur d_i of a point at Z_A which can be expressed as shown in Equation 1-51.

$$d_i = d_A[1 - \frac{1}{f} M'(Z_A - f)] \tag{1-51}$$

Another source of blur comes from the fact that the imaging of the background is diffraction limited [69][6]. With Equation 1-52 showing the diffraction limited minimum image diameter d_d. where λ is the wavelength of the light.

$$d_d = 2.44f/d_A(M+1)\lambda \tag{1-52}$$

One tries to minimize the overall image blur d_{blur}, Equation 1-53, while optimizing the sharpness of BOS. It is a weight-off in aperture diameter d_A that needs to be made since it increases geometric blur, Equation 1-51, but decreases diffraction limited minimum image diameter, Equation 1-52.

$$d_{blur} = \sqrt{d_d^2 + d_i^2} \tag{1-53}$$

Besides use in visualizing helicopter blade vortices, BOS has also been succesfully used to visualize ultrasound in liquids [70][71]. It has also successfully been used for visualising a airborne pressure field generated by ultrasonic transducers in a phased array [72]. This acoustic levitator setup is very similar to the setup used in this report. Even though, M. Iodice et al has shown the feasibility of visualizing pressure fields for levitation traps, measurements quantifying the pressure field have not been done.

1-4-4 Microphone

Some would say the most simple and straight forward method of measuring sound pressure is using a microphone (or hydrophone in fluids). Visualization a complete pressure field with a single microphone is time consuming. It is possible, however, by using a motion stage that allows measurements in multiple places or using multiple sensors. It is not desired since a microphone can have an effect on the sound field [42]. Especially when the size of the microphone housing is similar to the wavelength of the observed frequencies. Using optical fibers to measure the refractive index in air has been done successfully [73] but also requires multiple sensors or a motion stage. To get a good understanding of the field one must measure at multiple locations spanning the three coordinates with a good enough resolution, which is time consuming. Using a motion stage also requires the assumption to be made that the field does not change significantly over the whole measurement set and is not influenced by the measurements. The usage of a microphone remains a good option for calibration, especially when the influence of the microphone on the sound field is better known. Microphones and hydrophones are commonly used to quantify ultrasound both airborne and in liquids [73]. Quantitative volumetric measurements of airborne ultrasound has even been achieved [74]. Mapping the entire acoustic pressure field of a phased array however has not been attempted.

1-4-5 Acoustic holography

Acoustic holography and near-field acoustical holography make use of the measured sound field to reconstruct the complete three-dimensional field [75]. Both are a methodology of acoustic source identification through the measurements of the sound pressure, the prediction of acoustic variables, such as the velocities, to end up with a visualisation of the visualisation of the sound field [11]. It is a method that is used in industry for example noise source identification and non-destructive testing [76]. So to clarify, this isn't a measurement technique on itself but rather a method of reconstructing the acoustic field using a multitude of, for example, microphone measurements. Quantitative acoustic field measurements of an

ultrasonic acoustic array have recently been done using a transient acoustic holography [77]. The proposed method shows the possibility to detect defects in the source transducers and calibrate accordingly. Though very useful, for application in a double phased array, where reflections are bound to occur the method seems insufficient, for quantifying or visualising the pressure gradient.

While acoustical holography is used to improve acoustic levitation, it uses the methodology of holography to calculate both the direct and scattered sound contributions to the quality of an acoustic trap [35]. The aim of the paper is combining both direct and scattered acoustic waves to construct a trap, not verify the existing acoustic field. This paper only verifies the introduced model against another model that does not take into account the scattered field without verifying the trap quality by real life measurements. Using holography to visualise or quantify an existing airborne ultrasonic field has not been achieved.

1-4-6 Velocimetry

Velocimetry, the measurement of velocity takes many forms and names. It is a broader category under which fall: laser doppler velocimetry (LDV), particle image Velocimetry (PIV) and laser induced fluerencence (LIF) velocimetry. All of which are different methods for measuring fluid velocities, some utilising a laser, as the name indicates. Laser doppler vibrometry, sometimes also abbreviated as LDV aims at measuring the doppler shift of solid particles or membranes, and does not fall under the category of velocimetry. This measurment technique is covered in subsection 1-4-7. Since the goal of this section of the report to list relevant pressure gradient visualisation techniques, fluid velocity measuring techniques fall outside of the scope. Despite this, measuring fluid velocity is relevant for determining the Gorkov potential (Equation 1-21) and gaining insight into the fluid mechanics of acoustic levitation. Some techniques might even be able to be adjusted to measure the pressure gradient, thus it is worth covering them in this report.

PIV is commonly used to measure a two-dimensional cross section of a flow field simultaneously. The seeding of particles however may influence the acoustic field and thereby the flow field [78]. Laser doppler Anometry (LDA) or also known as Laser doppler velocimetry (LDV) is a method that used doppler shift of light to measure velocity of a (semi-)transparent medium. The doppler shift is measured from light that is scattered from small particles suspended in the medium [7]. Many different setup configurations exist dependent on application. Even though LDA has a high temporal resolution, it is only possible to measure velocity at any one point in time [79]. LDA has been succesfully applied for simultaneous measurements of acoustic and streaming velocities in a periodic acoustic field [80].

Laser doppler velocimetry has been used for semi-quantitative measurements with of streaming velocities caused by ultrasound in air [81]. The study however was not aimed at finding the pressure gradient. Schlieren has even been used together with PIV to observe turbulent flow of a jet ignition [82]. In this paper the pressure gradient that is visualised from the eddies in a turbulent flow serve as the seeding 'particles'.

1-4-7 Interferometry

Interferometry uses the interference of light to extract information. Compared to schlieren and shadowgraphy, the working principle of interferometery does not rely on the deflection of light [7]. A light beam is usually split up into a reference and a measurement beam and later combined and compared to extract information, as is illustrated in Figure 1-19. The Mach-Zehnder interferometer is often used for aerodynamic flow measurements as it allows for a large displacement of the reference beam compared to the test beam [7]. As the beams travel along two paths, with and without the test section, the beam through the test section gets slightly altered due to a perturbation in refractive index. Using wave optics, it can be understood that a phase difference occurs between the reference and the measurement beam as there is a slight difference in refractive index along the optical path [7]. The phase difference of the light between the two beams lead to an interference pattern which can be used to evaluate the path length difference and the refractive index perturbation [7]. The obtained image from interferometry consist out of fringes which look like a bright and dark stripe pattern. Interferometry as described above, mainly uses monochromatic light but interferometry using ultrasound does also exist [83] but is left outside of the scope of this quick overview of interferometry.

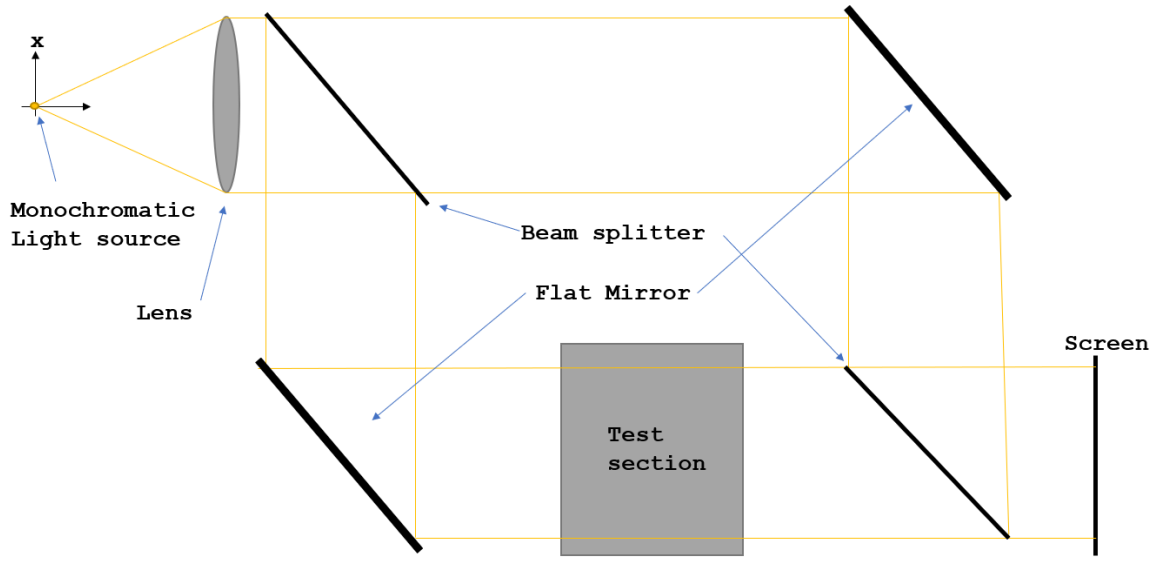

Figure 1-19: Illustrated setup of a Mach-Zehnder interferometer [7]

Using interferometry for qualitative measurements of ultrasound have been done in water for in the megahertz frequency [84]. Other optical measuring methods using phase difference also exist and have been used for tomography of ultrasound beams in water [17]. Qualitative measurements and visualisation of the pressure amplitude of airborne ultrasound using interferometry have also been achieved [85][86]. The alignment however, of an interferometer is somewhat complicated [7]. Measuring the waveform of a single 40kHz transducer had a limited spatial resolution of 1mm and took over an hour[85] since a laser is used to map a grid of line measurements.

Laser Doppler Vibrometry Laser Doppler Vibrometry (LDV) can be used to make quantitative measurements of 2D ultrasound fields in air [8][1]. If the assumption is made for adiabatic conditions, as is with most light based methods, the refractive index can be related to the sound pressure rate and quantitative measurements can be made. A laser beam is split up into a measuring and a reference beam. The measuring beam is aimed at item to be measured and a phase change will occur in the light. This happens due to a velocity change due to changes in refractive index as a result of the acoustic pressure field in the measured volume. Instead of the ray bending phenomenon, the phase-lattice theory explained in section 1-3-1 is taken advantage of. In Figure 1-20 a rigid reflector is shown with a measuring volume in which ultrasound is generated. Often the sample itself is not rigidly clamped and will provide scatter of the light. This scattered light is compared with the referenced beam. Both phase and intensity in the measured field can be reconstructed.

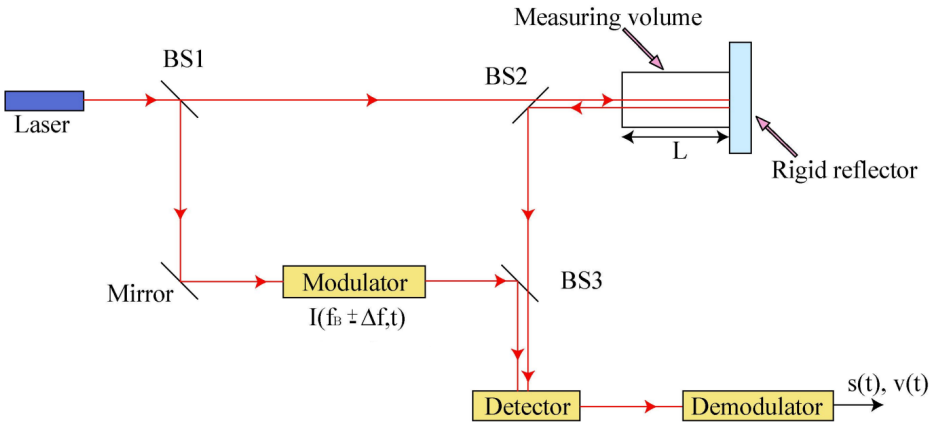

Figure 1-20: Illustrated setup for Laser Doppler Vibrometry [8]

1-4-8 Tomography

Tomography isn't a detection method itself but a method of converting measurements from different angles into a higher order output. For example converting 2D images into a 3D model. Tomography uses waves that penetrate a certain object which are directed from different angles surrounding the to be observed object. Taking the collection of measurements from different angles a tomographic reconstruction can be done to get a slice or even 3D field of the observed object. It is a common method used in CT and MRI scans, but can also be used with ultrasound. Optical phase contrast tomography (OPCT) provides an instantaneous three dimensional measurement of the pressure field without requiring a model for the pressure field structure [87]. However, the minimum detectable signal levels are a function of the field structure. This method makes use of the phase change between light beams that traverse different areas of refractive index.

Optical diffraction tomography has also been applied to ultrasound [62] and airborne ultrasound [46]. In the last study single transducers in the frequency range from 200kHz to 1MHz with a pressure amplitude in the kPa range have been studied successfully using a laser. Though, the margin of error deemed not satisfactory for a reference measurement system, but improvements seemed possible.

Tomography has been applied with both traditional and background oriented schlieren (BOS) to characterize an ultrasonic acoustic field [88][89][90][9]. In the experiments, transducers operating over 1MHz were used in water. Using BOS pressure field estimations were made of the pulsed ultrasound. BOS Tomography is illustrated in Figure 1-21. Only single transducers are classified simultaneously in a setup that prevents standing waves. Tomography hasn't been applied to airborne ultrasound generated by a phased array yet.

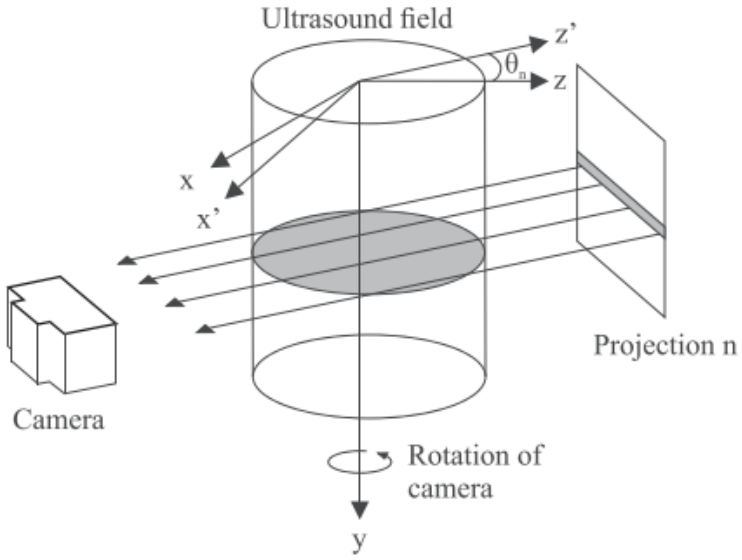

Figure 1-21: Illustration for BOS tomography [9]

1-4-9 Acoustic levitation specific methods

While the other discussed measurement methods aim to reveal more information about an arbitrary pressure field, one can also use the use application of the pressure field to gain knowledge. Analyzing a known particle that is levitated in an acoustic field can tell something about the shape and strength of that field. Although it is good to discuss these methods visualizing and analyzing the acoustic field pressure, usually a separate way is necessary to verify the formulas and assumptions that are used in these techniques. These methods also give a very local and thus limited observation, but can be directly applied to airborne ultrasound.

Minimal required levitation force The first way one could go measuring the pressure field is looking at the required levitation force for a certain particle to levitate. Using the Gorkov potential (Equation 1-21) one can derive the minimal required levitation force for a given particle [29]. A 1D example is well presented in the MSc. Thesis of S.J.P.M Roefs. The minimal acoustic pressure needed for the acoustic force for a 1D example is given in Equation 1-54. In which ρ_0, ρ_p, c_0 and f are the mean medium density, the particle density, the mean speed of sound and the sound frequency. This is assuming a spherical particle much smaller than the wavelength.

$$p_a^{min} = \sqrt{\frac{8g\rho_0\rho_p c_0^2}{10\pi f}} \tag{1-54}$$

Levitating particle eigenfrequency The second way to gain insight into a local pressure is looking at the particle eigenfrequency. A levitated particle can oscillate around its levitation position as a ball oscillating in a bowl or a mass spring system. For small oscillations around the equilibrium position the harmonic oscillation can be described 1-55, which can also be derived with the Gorkov potential 1-21 [85].

$$\Omega = \frac{1}{2\pi}\sqrt{\frac{20\pi^2 f^2 p_a^2}{10\pi f 4\rho_0\rho_p c_0^4}} \tag{1-55}$$

1-4-10 Consideration for best suitable measurement technique

In this subsection the best suitable measurement technique is chosen, from all methods discussed. The main goals of the setup must be able to achieve visualisation of airborne ultrasound. Since the setup will be used as a research tool it is useful to consider design requirements that influence the usability of the setup. These design requirements are:

1. **Difficulty:** The experimental setup should be acquired, build and tested within the scope of a MSc. thesis. There should be time left to experiment with the setup, besides designing and constructing it.
    - 1a. Purchase and delivery of the equipment should be less than 2 months
    - 1b. Alignment period should be less than 1 month, including necessary training for specialized equipment
    - 1c. Total setup cost should be less than 10000EUR
2. **Time per measurement**.
    - 2a. The time for one measurement should be less than one minute
    - 2b. Initial post-processing steps should take less than 30 minutes
    - 2c. Direct, live feedback is an advantage
3. **Measurement sensitivity**
    - 3a. Should be able to measure acoustics with pressure amplitudes in the range from 300Pa to 3000Pa. These are the calculated pressure amplitudes for a single transducer and within an acoustic trap generated by the acoustic levitator. Sensitivity should be able to be adjustable within that range.
    - 3b. Spatial resolution should be at least $\frac{\lambda}{10}$
    - 3c. The sensitivity to external factors should be to such an extend that it will not require the setup of a controlled environment exceeding the alignment period.

One also needs to consider the type of measurement that needs to be done. Two transducer arrays facing each other produce a volume in which standing waves are created through constructive interference. Since the goal is to both measure and visualise the pressure gradient of that field. To specify, the goal is to verify how well the theory corresponds with reality and to get more information on the pressure (gradient) in of the nodes levitating the particle. Using a point measuring method such a as a microphone gives a very good indication for that specific point but for calculating a gradient many measurements need to be done that quickly become very time consuming. For this reason, among others, using a microphone as a main measurement technique is not chosen. Velocimetry also requires specialized equipment, which will exceed the maximum alignment period. But most importantly, velocimetry does not measure pressure gradient.

Choosing a method that shines light through the volume of interest seems most suitable. Though promising for its high sensitivity, interferometry, the benefits do not out weight the disadvantages. It will have a slow time per measurement since line measurements are done.

It is also a method that requires more specialized equipment and is more difficult to set up than the rest of the presented methods. It will most likely exceed the maximum alignment period, since it will require a controlled environment. While similar, schlieren is superior over shadowgraphy and BOS for the higher sensitivity. The advantages of easier setup for some applications of BOS do not apply, since the volume of interest is in the range of decimeters. A downside of all light measuring methods is that, one has to realize that measuring what has been done to that initial light is a result of everything that has happened along the complete journey of that light beam. This however could be overcome using tomography.

1-5 Knowledge gap in literature: Project proposal

Visualising the complete airborne ultrasound field from a phased array has only briefly been demonstrated [67]. Disturbances in the Hz range still effect levitated particle stability, which may possibly be found looking at the pressure field. A comprehensive overview of applying the schlieren method to a phased array to visualise the acoustic field is not found.

Traditional schlieren is an excellent way to quickly visualise the airborne ultrasound field. A research tool in the form of a schlieren setup that can visualise the airborne ultrasonic acoustic field shall be designed and constructed. First, the right equipment will be chosen for the setup. A model will be made to generate schlieren images from the calculated acoustic pressure field. Once the construction of the schlieren setup is finished the schlieren images can be analyzed and compared to the model.

1-6 Considerations for suitable schlieren setup

Since schlieren is the most suitable measurement technique it is worth doing a more deep dive into it. This section will cover all considerations that need to be to be understood to get to a schlieren setup that can quantify and measure the acoustic pressure field of an acoustic levitator.

1-6-1 Schlieren of high speed phenomena

When trying to image quick, repeating phenomenon like ultrasound waves, two options are possible. Either a short exposure time, shorter than the period of the phenomenon that is being captured, with a accompanying illumination period, or a longer exposure that that gives a time-averaged image of the phenomena [91]. The first option requires a camera that can be synchronised with the acoustics and has a shutter speed that is quick enough for the phenomena. High speed camera's able to capture several thousands of frames per second exist but are quite expensive (>10000EUR). The second option needs an illumination period that matches the high speed phenomenon frequency. Synchronising the light frequency to the acoustics is much easier done and and this approach is used in this report. This is illustrated in Figure 1-22.

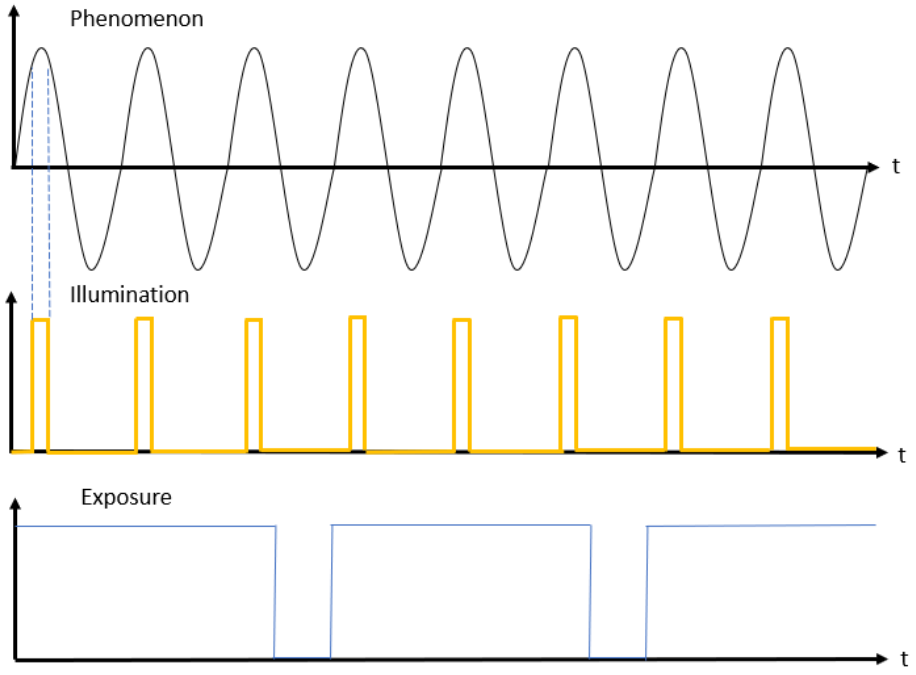

Figure 1-22: Schematic overview of illumination period and camera exposure time

1-6-2 Equipment

Both the light source, source slit and cut-off are essential items to a well functioning schlieren setup.

Light source Choosing the right light source for your application can be quite difficult dependent on the total needed amount of light. With large mirrors and high background illumination more powerful light sources are needed. Luckily, since the introduction of the LED, one does not need to consider the differences between light sources as spark gaps, xenon tubes and arc lamps anymore [92]. For visualising an acoustic levitator with a schlieren setup with a mirror diameter of about 20cm an LED is sufficient, as it has been done before [67]. LED's can also be pulsed in the sub micro second range, which is useful for high speed schlieren [92][51] as is explained in subsection 1-6-1. Dependent on the emitter size, an LED can sometimes be used directly at the focus without the need for a source slit [92].

Source and cut-off combination Many variations exist of the source and cut-off combination that can emphasize certain features in the schlieren image [51]. Schlieren allows for the unique feature that allows the choice of selecting a source and cut-off pair. Settles gives an in-dept overview of these pairs. The most simple and useful combination remains the rectangular source slit and knife-edge [51]. The largest range of schlieren sensitivity can be obtained with the simple pair and no reason necessary to use other complicated shapes. Some main distinguishing pairs will be named here that could be useful.

Understanding the difference between dark-field and bright-field source and cut-off combinations can be insightful. Dark- and bright-field are types of spatial filters, also known from microscopy. While dark-field methods block the lower frequency components and the DC component of the spatial frequency spectrum bright-field methods do the opposite [51].

Instead of a knife edge one could opt for using a graded-filter. In situations where sensitivity does not have the highest importance a graded-filter is a better choice as it extends the sensitivity range and lessens the diffraction effects [51]. This will also result in a sharper picture with better spatial resolution.

With the phase contrast methods the knife edge is replaced by a suitable phase plate. Phase contrast has the advantage that it is much more sensitive to small, weak phase perturbations. But the main disadvantages for schlieren applications, is the lower ability to visualise amplitude objects [51].

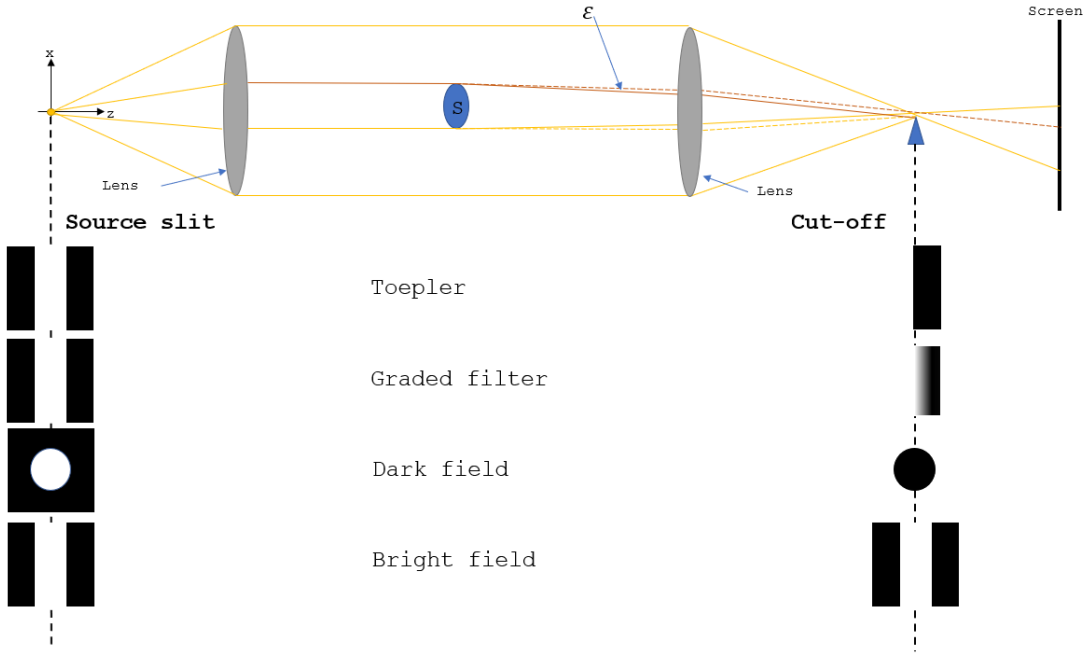

Figure 1-23: Variations on source and cut-off pairs

Color schlieren also offers great benefits but will be covered in section 1-6-4.

Cut-off placement All components must be carefully aligned to avoid, as much as possible, issues such as collimation, focus and non-uniform light distribution over the collimated light beam [38]. Many different combinations of source and cut-off filters can be used. The adjustment of the knife-edge, does not only determine the contrast of the image but also the uniformity of light distribution. The knife edge is to be placed exactly on the focus point of the spherical mirror. Too close or too far from this point axially, and the screen will not display a uniform light distribution. This is illustrated in Figure 1-24.

Optics and alignment The required optics needed for a schlieren setup depend on the setup type that is used and on the sought precision.

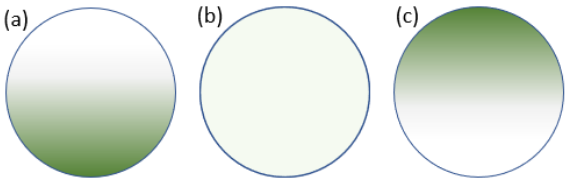

Figure 1-24: The effect of the axial knife edge position on the uniformity of the light distribution. (a) too close to the mirror (b) correct placement (c) too far from the mirror focal point

The alignment of the optics is important in order for the system to work. It can be made easier by using a mirror mount which has an adjustable rotation. Avoid as much ambient light, by turning off room lighting and closing curtains, helps to identify the beam of light with a sheet of white paper. Although not as prone to vibrations as interferometry, it is important to make sure that the setup is rigid. As schlieren depends on ray-optics instead of wave-optics, the setup is more resistant to vibrations than interferometry which would already display motion amplitudes in the order of light wavelengths [38]. Though with a setup length in the order of meters, bending and rigidity of the optical mounting can be noticeable.

Once in a good position axially, the knife edge can be adjusted to determine the percentage of cut-off. This determines the sensitivity. Where a small cut-off % will result in a small amount of light being blocked, which leads to a lower contrast with the possibility of camera saturation [38]. A large cut-off % will result in a higher contrast but may also cause the loss of information in regions where there was a small pressure gradient.

1-6-3 Schlieren sensitivity

The schlieren sensitivity or sometimes also referred to as the 'limit of visibility' is interpreted as the minimum variations in contrast of an image required to detect a difference in the varying refractive index. This is determined by the refractive index variations, the sensitivity of the schlieren setup as well as the image capture capabilities of the camera [93]. The sensitivity of the schlieren setup is considered without taking the camera into consideration. The camera does play an important role in the acquisition of the schlieren image but can be adjusted.

Schlieren setup sensitivity before camera The formulas (1-56) given by Settles [51] give a great explanation of the sensitivity, however it is good to verify what this will actually mean in practise and access the influence of each component of the measurement setup to the overall sensitivity. A low refractive index variation, will require a high sensitivity from both the schlieren setup and the accompanying camera. The refractive index gradient of a test subject is often not the setup parameter that allows tweaking for increased sensitivity thus the influence of the schlieren optics and imaging capabilities will be discussed below.

For a given schlieren setup, there is a limit in sensitivity, and thus the minimum detectable refraction ϵ_y. To get a ballpark figure, it is given in literature that a 5% contrast should be detectable [51] Combining Equation 1-39 and Equation 1-45 one can obtain Equation 1-56, which is a limit of measurement sensitivity for a given setup assuming a 5% contrast threshold

[51]. Where the sensitivity is dependent on the refractive index gradient itself, the schlieren setup and the medium.

$$\frac{\delta n}{\delta x}|_{min} = 0.05\frac{n_0 h_k}{L f_2} \tag{1-56}$$

In choosing the right components for a schlieren setup one might not exactly know the range of the refractive index that will occur in the test area. The greatest refraction ϵ_{max} can be estimated with Equation 1-57[51]. This would be the maximum angle of deflection. In Equation 1-57 the assumption is made that a spherical 'bubble' of high density has a focusing effect like thin positive lens. The greatest refraction then occurs at the outer edges of that lens, with n_0 and n_1 being the mean refractive index and the maximum perturbation with respect to that mean, respectively. Taking the values used and calculated in subsection 1-1-2: $n_0 = 1.0003$, $n_1 = 6.0946 \times 10^{-6}$, ϵ_{max} can be estimated at 1.2186×10^{-5} rad.

$$\epsilon_{max} = 2(\frac{n_0 + n_1}{n_0} - 1) \tag{1-57}$$

In the quest of achieving the best sensitivity one needs to optimize h_k/f. Since h_k cannot minimized without limit due to diffraction limits, it is dependent on the source slit dimensions. Usually a cut-off percentage of around 50% is deemed typical where diffraction effects can be neglected. When studying an object, with the photographic method, which produces a slight deviation in the light beam, it is necessary to use the smallest possible light source slit [94]. This is of course limited by the total amount of light that can shine through the source slit.

Not properly adjusting the measuring range of the schlieren setup for a given phenomena can result in measuring range anomalies which can result in an almost binary schlieren image appearance, due to over- or under-ranging [51]. In case of a color filter, the measuring range of the schlieren system can also be related to the dimensions of the source given that the color filter is twice the size of the source in both directions[19].

Schlieren setup sensitivity at the camera Modern day camera's allow easy adjustment of sensitivity to fit the schlieren setup measurement range. Using a single 8-bit channel allows the measurement range to be divided into 2^8 pieces. There are also camera's supporting up to 12 or 14 bits channels if higher sensitivity is needed. Most relevant schlieren setups use a commercial camera for visualisation as is shown in Table 1-4.

Diffraction limits The diffraction limits of schlieren sensitivity are not explained in the geometrical-optics definition of sensitivity. When an unobstructed image height h_k becomes smaller it will eventually start to behave like a narrow slit [51]. Diffraction problems start to occur when the light wavelength starts to come close to the critical distance d. Regular cut-off amounts using a source slit with dimensions in the $10 \cdot 10^{-2}$ mm range and using visible light in the range of 550nm should not present too many problems. Seeing a bright light band or diffraction 'halo' around objects, especially at a high cut-off % is common, though not a serious problem [51].

1-6-4 Quantitative schlieren

Schlieren imaging can produce stunning and insightful pictures but in many applications there is the need to also quantify this image. First though, it is important to understand how to interpret the beautiful schlieren pictures. If one assumes the a two-dimensional field with constant $\frac{dn}{dy}$ at a given x, y over the optical axis z, with length L, it becomes easier to interpret the contrast. The schlieren image lightens when the index of refraction increases in the perpendicular direction away from the knife edge. Thus a lighter region indicates a positive local density pressure gradient in the direction perpendicular to the knife edge [7]. The opposite is true for darker regions. Just interpreting the schlieren image contrast, is not utilising the full potential of schlieren as it allows for quantification. This can be done in multiple ways of which the most important ones are named here.

Weak lens Quantitative schlieren relies on the ability to relate the pixel intensity of a schlieren image to a imaged refraction angle, which is caused by a refractive index gradient [92]. The most straight-forward approach is putting a calibration object in the field. This calibration object has a known refractive index or refraction angle which allows a direct comparison from pixel intensity to a corresponding deflection angle and thus refractive index gradient [92]. The simplest calibration object being a weak positive lens. In combination with a Z-type setup, this is known as Schardin's 'calibrated' schlieren. The weak lens is placed in the field of view which provides information for deflection angle of the light [80]. The weak lens refracts the light and cause the light to be focused to a focus point beyond the knife-edge position. The focal length of the lens must also be bigger than the focal length of the main schlieren optics, with a larger lens focal length providing a finer resolution of refractive index variations [92]. A simple positive lens will deflect a light ray differently dependent on the radial location r on the lens. Going through the center of the lens will not deflect the ray with maximum deflection at the edge of the lens.

The position on the lens can be correlated to the the pixel intensity and the light deflection though Equation 1-58. Where r is an arbitrary location on the lens and f the focal length of the lens [80].

$$\epsilon \approx \tan(\epsilon) = \frac{r}{f} \tag{1-58}$$

Once the pixel intensity is correlated to the refractive index gradient, the rest of the schlieren image can be integrated to produce the refractive index field. Besides using a lens as a calibration optic, one could also use another known refractive index. The laminar free-convection flow of a flat plate has been used as well to compare schlieren quantification methods with [80], which is also shown in Figure 1-25. Observing acoustic waves one could also use a calibrated lens to detect the sound signal and maximum amplitudes at a point in space. This maximum and minimum sound amplitude can than be correlated with the maximum and minimum measured pixel intensities of a visualised sound wave. The use of a microphone however can disturb the sound field as mentioned in subsection 1-4-4.

Color schlieren Color schlieren uses a color or rainbow filter instead of a knife edge as a cut off. This enables a quantification of the deflection angle of the light by differentiating

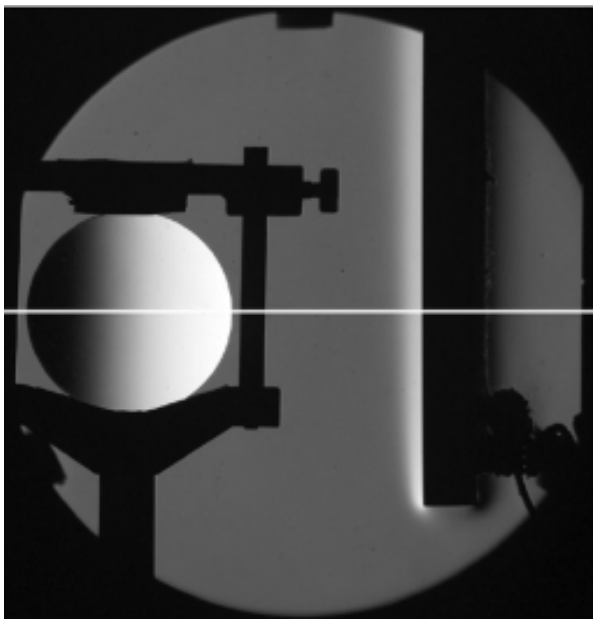

Figure 1-25: Example of a weak lens placed besides a heated metal block [10], knife edge is vertical

the shown colors in the final image [10]. The color filter has a varying color or hue. This hue can vary in 1 or 2 directions as shown in Figure 1-26. Initial white light from the light source, is deflected in different ways, dependent on the varying refractive index in the test area, such that a deflected ray will end up in a different color than the undeflected ray. This will color code the light. Using a 2-D color filter allows for bi-directional schlieren, visualising the projected density gradient in both spatial directions simultaneously[19].

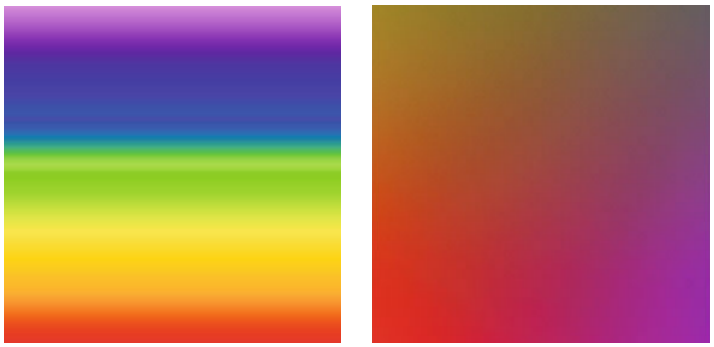

Figure 1-26: Left: 1D color filter . Right: 2D color filter

Besides producing visually striking images, color schlieren can have a few advantages. It can avoid the diffraction that can occur using a knife edge cut-off [38]. However, the design and production of a color filter are more difficult than placing a simple knife edge. While a knife-edge cut-off has the highest sensitivity is has a limited range. The color filter extends this range but at the cost of sensitivity [10].

Synthetic schlieren Synthetic schlieren or background oriented schlieren (BOS) is also used for quantitative schlieren but does yield a lower spatial resolution due to image blur [19]. BOS directly measured the pixel shift Δp of the background with respect to an empty test area. This means that ϵ or rather Δp is directly measured instead of it being converted into a pixel intensity as is the case with traditional schlieren. The deflection of the light is given by Equation 1-59. With the distances z_A and z_D being the distance of the camera lens to the test area and the distance of the test area towards the background, taken from Figure 1-17.

$$\epsilon \approx \tan(\epsilon) = \frac{\Delta p}{z_A - (z_A + z_D)} \tag{1-59}$$

There are some advantages, such as the ease and low cost of the setup that do not weight so heavily in selecting a suitable setup for visualising ultrasound. BOS will always deliver less image resolution compared to comparable traditional schlieren setups [92]. Visualizing ultrasound using background oriented schlieren has been achieved, though quantification was not achieved [67].

1-6-5 Modelling schlieren

There are three main steps in constructing schlieren images from flow fields [95]. The first, identifying and calculating the appropriate refractive index functions. Second, integrating these functions along the ling of sight and last, post-processing the integrals to obtain the correct image. The deflection of a single beam contains information about the spatial gradient of the refractive index integrated along the line of sight[6].

In the second step, integrating along the line of sight, two distinctions are made in literature. The first is the simplest and consists out of a line integral along a straight line approximation along the optical axis. This methods assumes there is minimal deflection of light through the flowfield and therefor the lightpath can be assumed exactly parallel to the optical axis. The seconds is called ray tracing [40] where the ray is adaptively traced through the flowfield. The position of the ray is updated and not necessarily exactly linear to the optical axis. This methods is more computationally intensive [95] but is sped up using a lot of pre-processing and the use of octree's.

In the third step, it was concluded that there is also a need for incorporating the effect of the optical system for the possibility to truly compare the experimental and digitally generated images [96].

1-6-6 Schlieren setups used in literature

Schlieren has been used many years to research pressure gradients in a wide spectrum of applications. In this section a brief summary of some relevant schlieren applications that are used in literature will be given. A setup is deemed relevant if it is similar in one or more of the following aspects: visualisation of (ultra)sound, similar size of target image, similar estimated pressure gradient and within the last 10 years. In the Table 1-4 the type of setup is specified, with abbreviation DCSM standing for double coincidence spherical mirror. The focal length of the schlieren optics is also specified under f. The shape and size of the source

slit are specified, though often it is not specified (n/s). The cut off type is also noted down together with a short indication of the content of the paper or the relevant pressure gradient.

Source	Year	Type	Camera	f [mm]	Source	cut off	Pressure gradient indication
[66]	2020	DCSM	Canon 6D	1500	∅ 50um	rainbow	2x bowl shaped 36x 40kHz
[97]	2020	DCSM	Canon EOS1300D	1200	n/s	knife edge	Leaky lamb waves SPL:(153dB-101.5dB)
[67]	2018	DCSM	Canon EOS1200D	1300	n/s	knife edge	2x phased array of 9x28 40kHz
[93]	2018	DCSM	Photron FASTCAM SA5	1500	n/s	knife egde	SPLs 120dB-80dB at 40kHz
[64]	2018	DCSM	Blackmagic Pocket	3120	∅ 400um	knife edge	1x 28kHz transducer
[98]	2015	2-lens	NAC MEMRECAM HX-3	1020	n/s	knife edge	10kHz - 40kHz single transducer
[99]	2014	DCSM	Canon 60D	1140	n/s	rainbow	Hot soldering iron
[56]	2013	2-lens	Lynx IPX-2M30-G	300	∅ 300um	knife edge	MHz transducer in water
[10]	2011	Z-type	Nikon D80 SLR	1168	□1 × 1mm	knife edge	f = 10m lens
[100]	2003	2-lens	Olympus OM-4	500	∅ 1mm	□1.3 × 7mm	MHz transducer in water

Table 1-4: Comparison of different schlieren setups used in literature

Chapter 2

Experimental Setup

2-1 Description of schlieren setup

A double coincidence schlieren system is often used for the reasoning that only one parabolic mirror is needed. With a small angle ϵ and a short distance to the mirror, this works in practice [51]. The need to only procure one spherical mirror is preferred. On top of this, an increase in sensitivity by a factor of two is very useful since the sought after pressure gradients are modest. The designed setup is illustrated in Figure 2-1. The components are further explained in the following subsections.

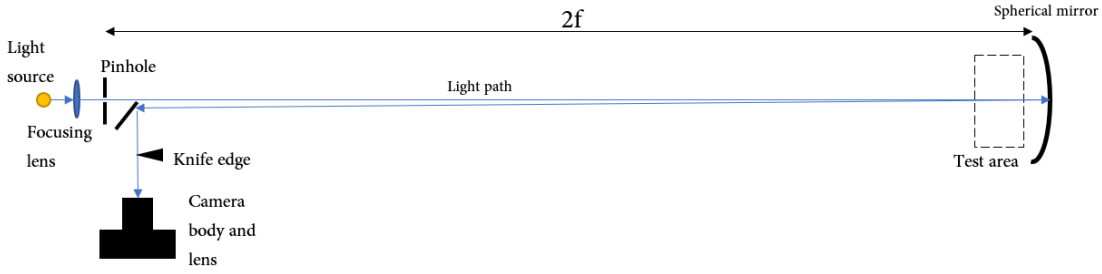

Figure 2-1: Illustrated double coincidence schlieren setup

2-1-1 Optics

A single parabolic mirror is used for a double coincidence setup. With a diameter of 8" (203,2mm) and a focal length of 80"(2032,0mm), the enhanced aluminum coated mirror from Edmunt optics seemed suitable as it had the longest focal length available within budget.

Since the pinhole and knife edge are to be placed at twice the focal length, a setup length of more than 4 meters is required. This is impractical in the available facilities thus a flat $\lambda/8$ mirror with a diameter of 100mm is used to redirect the optical path (not illustrated). This however does increase the complexity in the alignment. Pictures of full setup is shown in **??** and Figure 2-2.

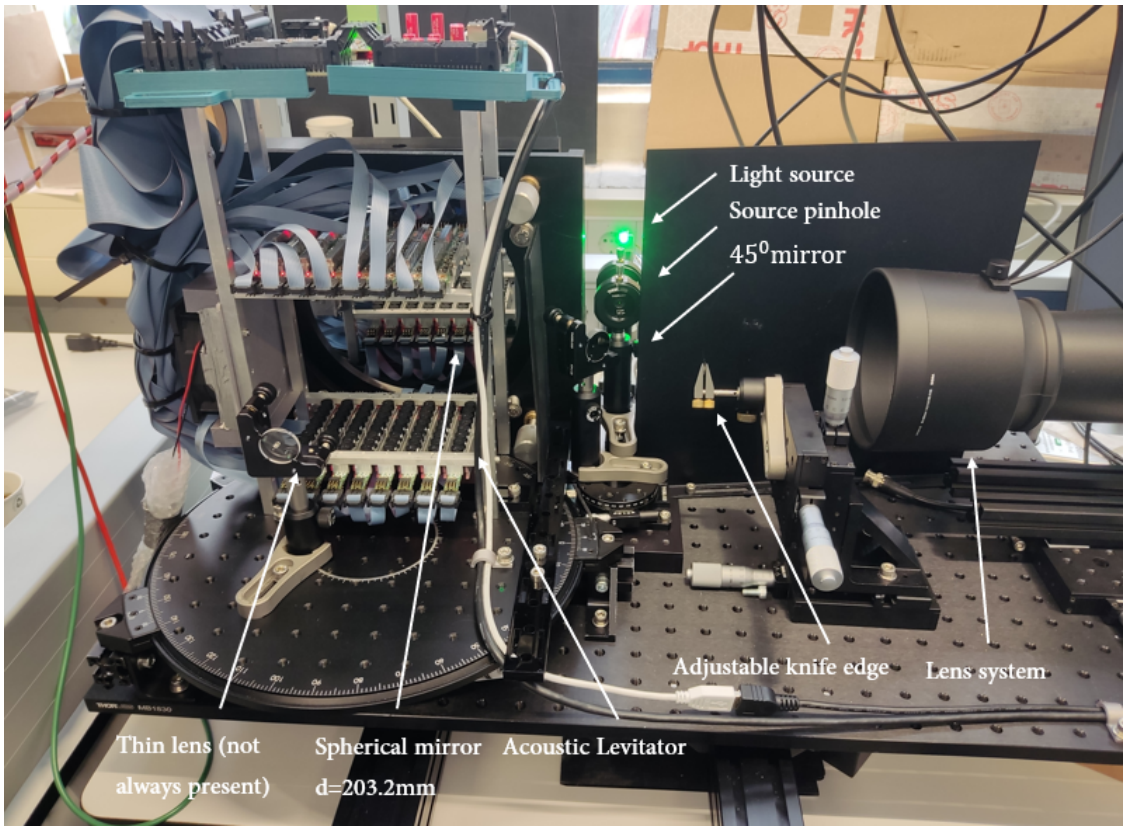

Figure 2-2: Experimental double coincidence schlieren setup

2-1-2 Light source and cut-off

Light source A regular green 5mm LED (NSPG500DS-G) is used, attached in series to a resistor of 180 Ohms. For pulsed schlieren in the kHz range, an LED is a suitable option since it is extremely affordable with sufficient luminous intensity. The LED is focused upon a 150 μm pinhole using a achromatic doublet lens, both from Thorlabs (P150K and AC254-030-AB), with a focal length of 30mm and a diameter of 1" (25,4mm).

As illustrated in Figure 2-1, the light originating from the LED is focused upon the pinhole. The path from the pinhole to the parabolic mirror is unobstructed, whereas the light that is reflected back from the parabolic mirror is reflected by a second smaller mirror such that it is perpendicular to the original light path. This is due to practical reasons for the placement of the knife edge, camera and lens system. While sometimes a 50/50 beamsplitter is used [66], using a mirror and deviating slightly from parallel rays is also common in practise [51].

Signals The signal to the transducers is being controlled by an FPGA which is synced with a waveform generator (Keysight 33220A). The acoustic levitator observed consists out of two opposite facing phased arrays of a total of 128 transducers. A square wave is automatically sent from the FPGA at the clock speed of the chip. This signal is used to sync the waveform generator. The signal to the LED consists of a square wave with an adjustable duty cycle which is amplified with a regular amplifier (Thandar Instruments TTi WA301). This is

illustrated in Figure 2-3. The duty cycle can be adjusted between 20 % and 80%, as is limited by the waveform generator. The phase delay and the light source frequency of the square wave can be adjusted as well. The LED will be driven at 30Vpp with a duty cycle of 20%. The light source frequency is set at 40kHz. The transducers are driven at amplitude 0.75 out of 1, which equals about 27.5Vpp.

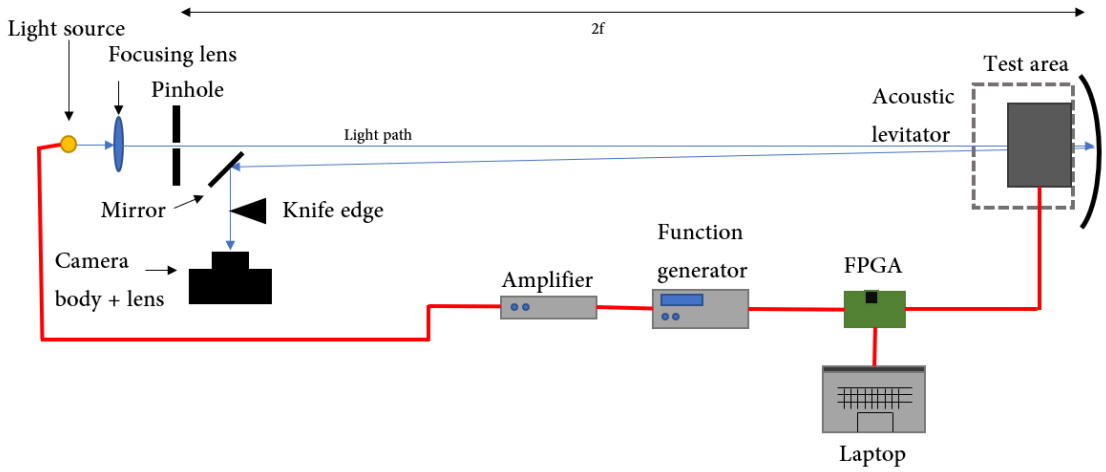

Figure 2-3: Schlieren setup and signal route

Front-lighting Front-lighting in the schlieren area is independent of primary illumination and can be very useful for image comprehension. The deliberate form of stray light, illuminating the levitated object, can be very useful and the illumination intensity, color, duration, timing and distance can all be chosen independently from the main light source [51]. Though Settles does mention that too much illumination can overpower the image. Balanced illumination is achieved by a Nikon fiber optic light source and aiming the two output light fibers onto the object to be illuminated. In this report no experimentation will be done regarding front-lighting, yet it is a very useful tool and can deliver beautiful pictures as can be seen in Figure 2-4. Instead of a dark shadow the levitated particle can clearly be seen.

Cut off As mentioned in subsection 2-1-2 using a simple knife edge is best option and it is not necessary to use another more complicated shape. The knife edge orientation is horizontal unless specified differently. The cut off percentage is difficult to determine %-wise, since a pinhole of just 150 μm is used. The alignment between the optical elements, and thus the cut off %, can be noticeably altered if the weight distribution is shifted. The alignment can also be effected by vibrations and shocks against the lab tables on which the setup is placed. This make it impossible to determine the exact cut off %. It will always be between 10% and 90% and optimized for each recording.

2-1-3 Image acquisition

To capture the schlieren and further export the data to process and analyze the images and videos, a camera and lens system are used. The camera body a Fujifilm X-T5 with a Sigma

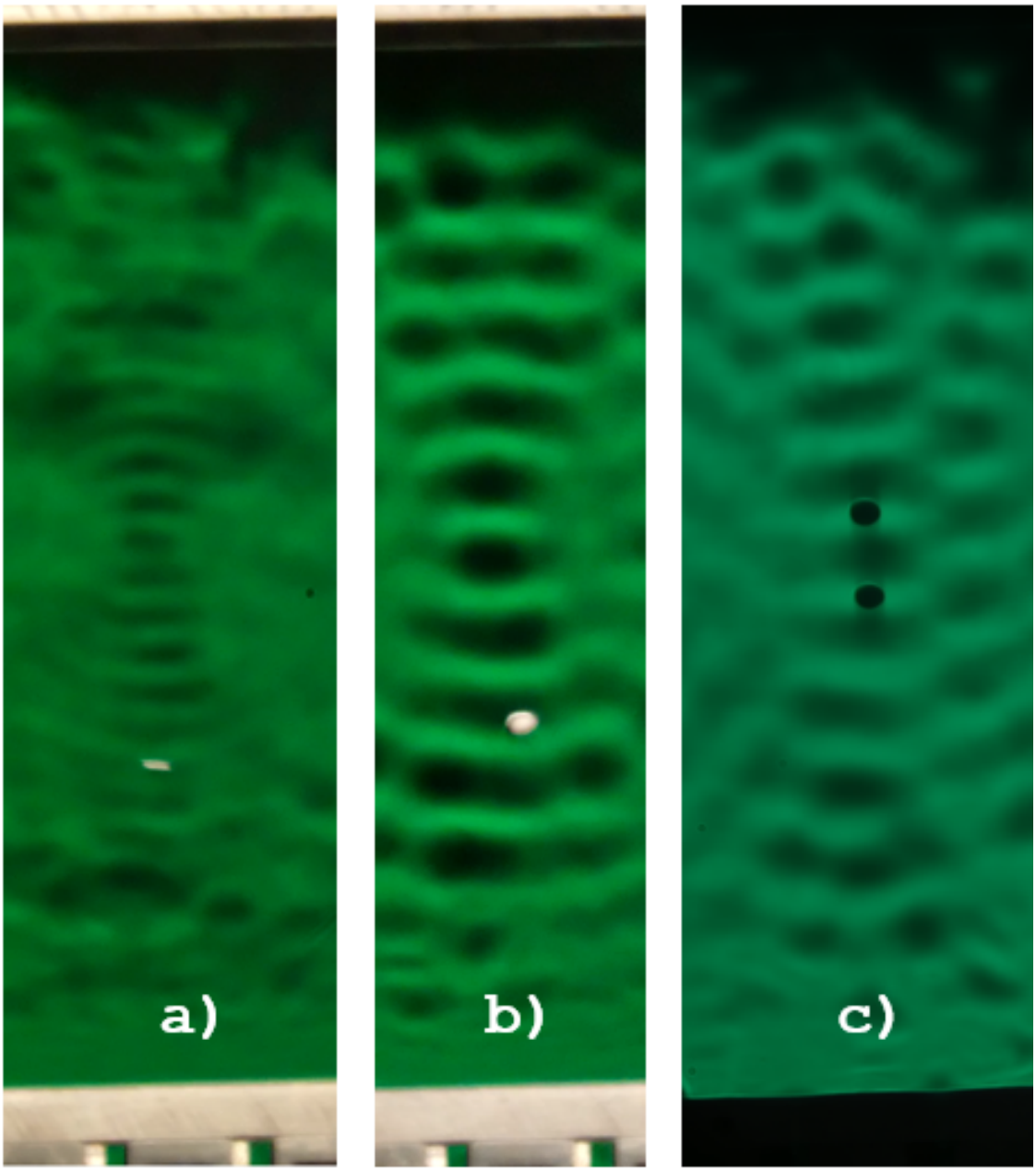

Figure 2-4: Demonstration of front lit vs. regular schlieren: a) Front lit levitated square object b) Front lit levitated styrofoam ball and c) 2 Levitated styrofoam balls without front lighting

60-600mm 1:4.5-6.3 DG hyper-telezoom lens system. This allows zooming in to a level where the full APS-C (23,5 x 15.6mm) sensor with a resolution of 6864x5152 pixels can be used. This system is relatively cheap, while allowing adjustment of many settings. There is also the possibility for direct video output through hdmi to a monitor, which is very useful for direct visual feedback. Unless differently specified videos are taken in a resolution of 4K (3840x2160 pixels).

It is unclear to what extend image processing and compression are taken place within the

camera. Images are usually compressed but can be exported in uncompressed form. Usually, due to thermal disturbances a video is taken at 4K, of which the mean pixel intensities are calculated. The videos are stored and exported in the MPEG-4 (.MOV) file format with the H264 codec. Unless specified differently videos are taken at 29,97 frames per second and have a bit dept of 24 (8 bits per color channel).

Shutter speed and ISO can be adjusted on the camera. Shutter speeds determines the amount of time the 'shutter' is open and light is captured on the image sensor. The ISO setting in the digital camera is a measure for the sensitivity of the image sensor to light. A higher ISO value corresponds to a greater sensitivity to light. Optimally the schlieren setup would be placed in a room where ambient light could be controlled. This was not possible in the current laboratory and within the time span of this report. Ambient light, both coming from other rooms and sunlight affect the illumination level of the camera. Shielding has been put in place to limit the effects of ambient light to a workable level, although it cannot be considered constant over multiple experiments. Through trial and error it has been determined that using an ISO of 6400 with a shutter time of 60 is sufficient for most conditions. These settings will be used unless specified otherwise. The effect of the ISO will be shortly covered in subsection 3-4-5 and can be seen in Figure 3-14.

Though it is possible to project the schlieren image directly on a sheet of, for example, white paper or matt glass, this is not advised due to losses in light intensity, contrast and resolution [51]. Instead focusing the schlieren directly onto the image sensor gives the best results.

The camera should be focused sharply on the plane at the location of the test area [10].

2-1-4 Image processing

As mentioned before a 4K video is taken at 29.97fps for 20 seconds, unless specified differently. The video is then analyzed using Matlab. The mean pixel intensity for all frames is calculated and put together into a resulting schlieren image. The image is used to compare different measurements. For measuring pixel values, the Matlab function 'im2gray' is used, which converts the RGB values into grayscale by eliminating the hue and saturation information while retaining the luminance, according to the BT.601 Recommendation standard. Using a picture instead of a video is quicker and does not need post-processing but noise due to thermal plumes or setup vibrations can disturb the clarity.

2-1-5 Alignment and stability

A custom frame is designed and constructed from extruded beams and optical breadboards. This frame is placed on soft rubber feet to dampen vibrations. The frame is stiff and allows the optical components to be mounted securely with respect to each other. The stability of the setup on its own was sufficient for imaging. However, the stability and alignment were easily influenced by leaning on or bumping against the table. The soft rubber is recommended as it dampens vibrations, it does allow for easy compression and thus misalignment between optical elements.

Influence of ambient air flows Ambient air flows can easily become visible in a sensitive schlieren setup and are undesirable. Ambient airflow can be caused by room ventilation, movement in the room or temperature differences. Both air flow and temperature differences can be visualised using schlieren, because of their relation to the refractive index as shown in Equation 1-20. To fight the interference of ambient air flows, Settles gives a few good suggestions, which can be found in his book [51]. The first suggestion of turning off room ventilation was impractical in the lab designated for this experiment. Thus keeping human motion was kept to a minimum but could not be set to the same level across all experiments. The main source of drafts was the heating of the transducers and amplifiers of the acoustic array..

2-2 Schlieren setup characteristics

2-2-1 Noise

Noise can be defined as the unwanted fluctuations or distortions in the image, or signal. Noise in the schlieren image can have multiple sources; refractive index gradient, optical elements and the camera.

Noise in refractive index gradient The goal of this thesis is to visualise the ultrasound acoustic waves. Using the schlieren method one can visualise the refractive index gradient which is dependent on pressure, but also on density and temperature. Thus perturbations in these will also be measurable. Heating of the transducers and amplifiers cause thermal plumes to rise and disrupt the visualisation of purely the acoustic pressure gradient, as is shown in subsection 4-3-1. And as mentioned in section 2-1-5 ambient air flow can also disrupt the schlieren image. Averaging out over time will greatly reduce the influence of these effects .

Noise in optical elements While noise due to insufficient optical elements can occur. The best quality mirrors within budget are used with the surface accuracy and quality specified in Table 2-1. The surface accuracy and quality are within specifications given by Settles [51]. There are certain places of damage on the optical elements causing a distinct distortion of the signal at that location. They can be easily spotted and cannot be removed without replacing optical components. These are also visible in Figure 2-6.

	Surface accuracy	Surface quality (lower is better)
Spherical mirror	$\frac{\lambda}{8}$	60-40
Flat 100mm mirror	$\frac{\lambda}{10}$	20-10
Flat 25.4mm mirror	$\frac{\lambda}{10}$	40-20
Focusing lens	-	40-20

Table 2-1: Surface accuracy and quality of used optics in schlieren setup

As an example are presented Figure 2-5a without noise and Figure 2-5b with a transducer line turned on parallel to the optical axis. All schlieren parameters remain the same between the two pictures, except the presence of an acoustic signal.

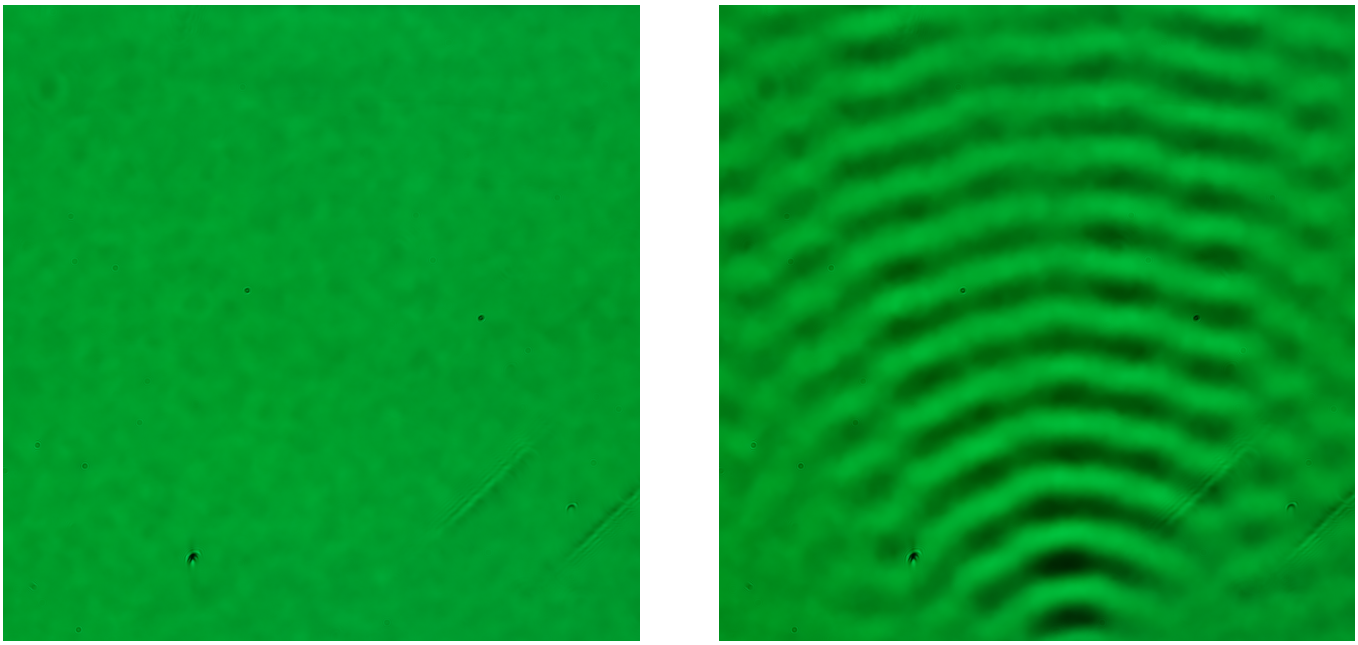

(a) Schlieren image without sound

(b) Schlieren image with sound

Figure 2-5: Standard deviation per section

Noise in camera equipment Noise relating to the image acquisition equipment, or camera is difficult to quantify as the exact image sensor specifications are unknown. The image compression and post-processing are also unknown. The noise of the optics and camera are different to the noise of the refractive index as they are constant over time. The standard deviation in Figure 2-5a is 2.72, while the mean is 97.3. These numbers are pixel intensities, without a unit, scaled in integers from 1 to 256.

To get a better understanding of the homogeneity of the noise, caused by either the inaccuracies in the optical elements or the camera, one can look at Figure 2-6. In this plot Figure 2-5a is converted to gray scale, divided into 20 x 20 sections, as shown in Figure 2-6a. The mean and standard deviation per section is calculated and presented in Figure 2-6b.

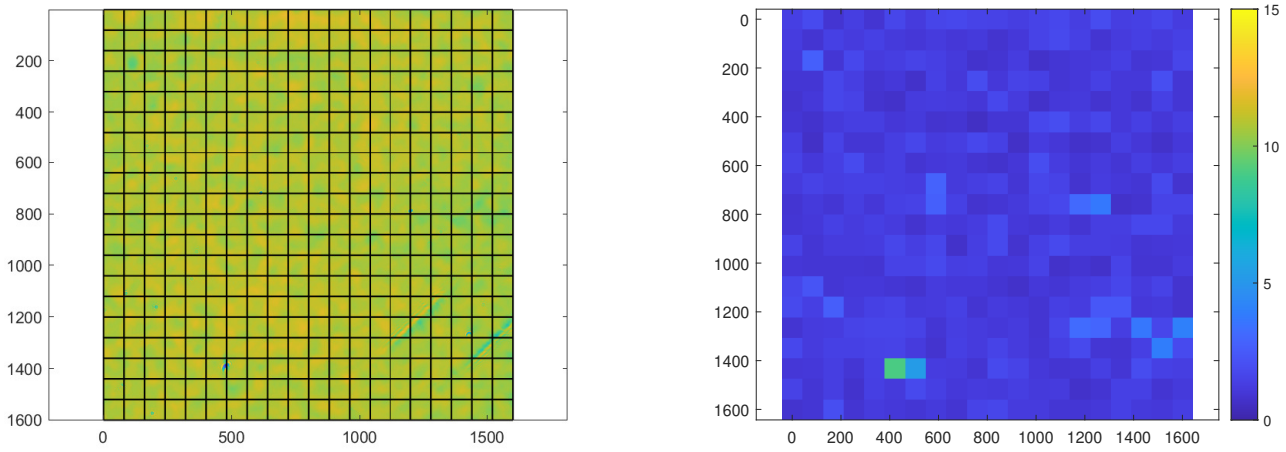

(a) Image, no sound, divided into 20x20 sections

(b) Standard deviation per section

Figure 2-6: Standard deviation per section

Higher standard deviations are present in the locations with damage, around the coordinates (1400, 500) and (1200, 1200). The overall standard deviations seems to be around 3. The standard deviation seems to be similar across the whole image. The influence of ambient light played an important role as well. Mostly affecting the complete experiment done at a certain time, but assumed to be constant for a single experiment done within the time span of an hour. More intense ambient light, for example in the form of sunlight, caused the mean intensity of the image to be raised, but can be assumed have a homogeneous distribution on the image sensor.

Signal-to-noise ratio Signal-to-noise ratio (SNR) is a common measure of the quality of an image, and is often used to quantify the amount of noise in an image relative to the underlying signal or information. A higher SNR indicates a better quality image, with less noise and more useful information.

Since the noise has been quantified in the last paragraph, the signal needs to be determined. This is done by analyzing Figure 2-5b converted to gray scale. The signal consists out of a sine wave with a decreasing amplitude. The maximum and minimum signal are determined by looking at the maximum and minimum amplitude of that sine wave. The maximum signal is 102 while the minimum signal is 28. Using the standard deviation per section of 3 one gets a $SNR_{max} = 34$ and $SNR_{min} = 9$ for Figure 2-5b.

2-2-2 Resolution

The spatial resolution of the images is dependent on the zoom of the camera. At maximum zoom the images have the highest ratio of pixels per mm. Fitting the distance between the two arrays vertically on the image sensor, divides 5152 pixels over about 130mm. This equals to about 39 pixels per mm.

The resolution on minimum detectable level of pressure is dependent on the sensitivity of the setup. To get a very rough estimate of what the range and least detectable signal is with this setup the example of Figure 2-5 and a single transducer are taken. Since a lot of assumptions are made the calculations are left for the appendices in section A-2.

2-3 Description of acoustic levitator

A short description will be given about the observed acoustic levitator that is used to produce the acoustic field. Also called the rectangular tower, it houses a total of 128 Murata MA40S4R transducers divided over two flat arrays. An array consists of 8 strips on which 8 transducers are placed. While each strip has a spacing of 17 mm, the transducers on a single strip are spaced with 10.5 mm. The amplifyers are connected on the same strip and driven by a FPGA which allows direct control of the setup through Simulink. The two phased arrays have a separation of 126 mm and held rigidly using a custom build aluminium frame.

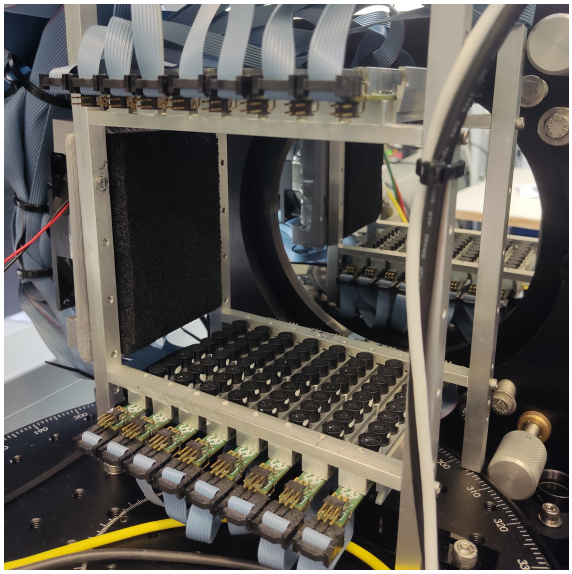

(a) Rectangular tower, close up view

Figure 2-7: Acoustic levitator setup 1: Rectangular tower,

To minimize transducer and amplifyer heating from rising and disturbing stable particle levitation, a pc case fan was added to the side. On the left side, on both **??** and Figure 2-7a, the red and black cables can be easily spotted that lead to the fan and fan shroud. The fan shroud, is designed such that a thin layer of air is blowing over the top and bottom array. The flow is verified using the schlieren setup. The fan is powered by 11V DC. The effects of this will be further explained in subsection 4-3-1.

Chapter 3

Parameters that influence the visualisation of the acoustic field

3-1 Influence of schlieren setup parameters on visualisation

The schlieren setup has many parameters that can be adjusted. There are parameters that influence the light signal. Others effect how the light is captured on the image sensor. All of these parameters have an influence on the final captured schlieren image. The parameters duty cycle and phase delay are illustrated in Figure 3-1 and will be properly explained in the next section, together with all the other relevant parameters.

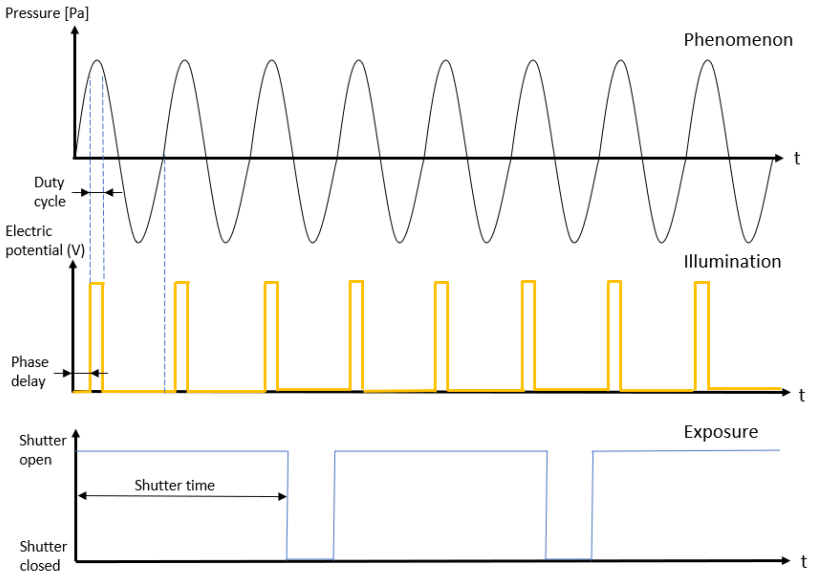

Figure 3-1: Influence of schlieren parameters on captured acoustic field

3-2 Schlieren setup parameter definition

The definition of the setup parameters are given in this subsection.

Duty cycle The duty cycle is defined as the % of the block signal sent to the LED that is high. With a duty cycle of 20%, this will result in a signal of 20% high and the remain 80% low. Only a high signal will result in the LED emitting light. This is illustrated in Figure 3-1.

Phase delay The phase delay is defined as the phase difference measured in degrees between the start of the block signal sent to the LED and the start of the incoming block signal from the FPGA. A positive phase delay means there is a time delay between the clocking signal and the output signal. This is illustrated in Figure 3-1.

Light source frequency The light source or pulse frequency is the frequency of which the square wave signal is sent out. This is kept at either the frequency of the acoustic signal, or twice this signal.

Cut-off orientation The cut-off type, of which multiple examples are given in Figure 1-23 is not varied. A simple knife edge is used. Two orientations are studied, of which one is used as a default throughout the report. A horizontal knife edge, the blade parallel to a xz-plane and the cutting edge parallel to the x-axis, will yield the refractive index gradient with respect to the z axis. For the coordinate system, refer to section 4-1-1. The horizontal knife edge is the default since the direction of the travelling waves is also predominantly along the z axis. A horizontal knife edge will cover the lower part of the z-axis, and when more cut-off is used, it moves in along the z-axis in positive direction. The vertical knife edge will cover the positive part of the x-axis and move along the x-axis in negative direction to get a higher %.

ISO A higher ISO value corresponds to a greater sensitivity to light. Increasing the ISO does also tend to increase the digital noise and grain leading to a decrease in image quality. The ISO values are settings selected on the camera.

3-3 Defining a baseline measurement

3-3-1 Transducer line

To see the effects of different parameters on the visualisation the same 'sample' has to be studied repeatedly, while varying the parameters. A line of transducers parallel to the optical axis is turned on in the acoustic levitator. All transducers have the same phase. Because of this, the pressure gradient across the optical axis is assumed to be constant, as is further explained in section 4-1.

3-3-2 Line cut

A line cut is the pixel intensities plotted from a vertical line. The plot is from right to left, with corresponding pixel intensities from top to bottom. The pixel intensities are plotted on a scale from 1 to 256. These are the gray scaled intensities in integers. A plotted line cut is often given since it gives a different way to present the pixel intensities and make the image more understandable.

3-4 Influence of each single parameter

3-4-1 Cut-off type and orientation

The source and cut-off slit combination effects what is being projected on the image sensor as previously explained in subsection 2-1-2. In this subsection both the vertical and horizontal knife edge will be analyzed. The use color schlieren has also been explored and will be analyzed.

Horizontal cut-off An acoustic levitator with horizontal phased arrays will produce the largest pressure gradients in the axis perpendicular to the array. Selecting a knife-edge orientation for visualising a vertical pressure gradient will largely yield the most insights. The bigger expected differences in pressure gradient will yield highest contrast in the image. However, selecting a different knife-edge orientation will give an insight into the pressure gradient in the perpendicular orientation which is also useful. The obtained images can be compared to straight line integral model explained in section 4-1.

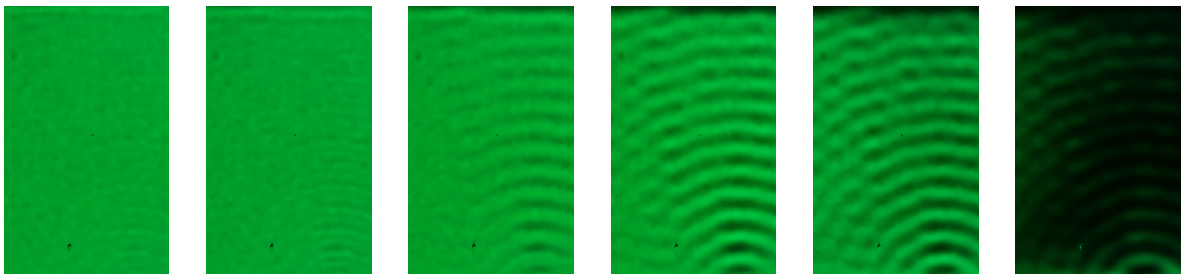

Figure 3-2: Different horizontal cut off with respect to the baseline a)

As is expected the further the higher the cut off %, the more contrast is seen in the schlieren image. This holds up to a certain cut off %, as can be seen in Figure 3-2. The best contrast can be seen in Figure 3-2e. After a certain % the amount of emitted light reaching the image sensor is lowered significantly not fully utilising the sensor, as can be seen in Figure 3-2f.

Vertical cut-off Instead of visualising the pressure gradient with respect to the z-axis, the pressure gradient with respect to the x-axis is visualised by using a vertical knife edge. The highest pressure gradients are expected, closest to the x-axis. As the pressure gradient is close to purely in z-direction on the normal from the transducer surface, a region without contrast shows, as can be seen in Figure 3-3c.

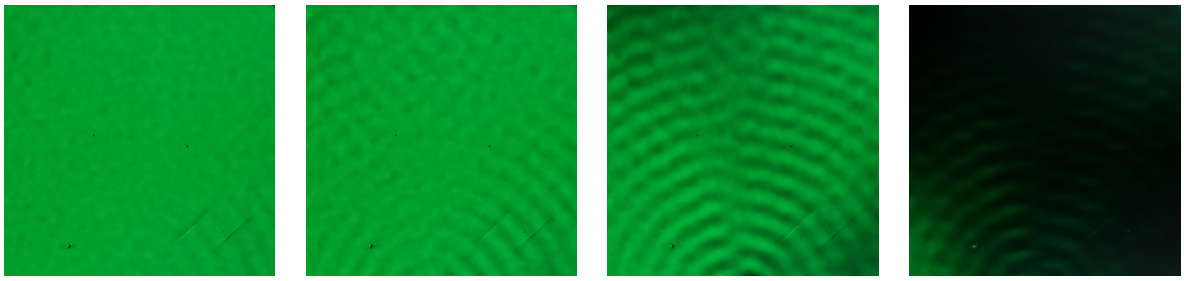

(a) +0.0mm **(b)** +0.1mm **(c)** +0.2mm **(d)** +0.3mm

Figure 3-3: Different vertical cut off % compared to the baseline a)

As is expected the further the higher the cut off %, the more contrast is seen in the schlieren image. This holds up to a certain cut off %, as can be seen in Figure 3-3. The best contrast can be seen in Figure 3-3c. After a certain % the amount of emitted light reaching the image sensor is lowered significantly not fully utilising the sensor, as can be seen in Figure 3-3d.

3-4-2 Duty cycle

Without varying the phase delay of the pulse the duty cycle is varied from 20 tot 50%. In Figure 3-4 one can see the result of turning on one row parallel to the optical axis. Row 3 on the bottom and the opposite row on top have been turned on with all phases set to zero. Voltage supply to the LED light source is kept the same over all experiments while, consequently, total emitted light is dependent on duty cycle. The LED is synced with the FPGA to ensure the same frequency is emitted both for the transducers as the light source.

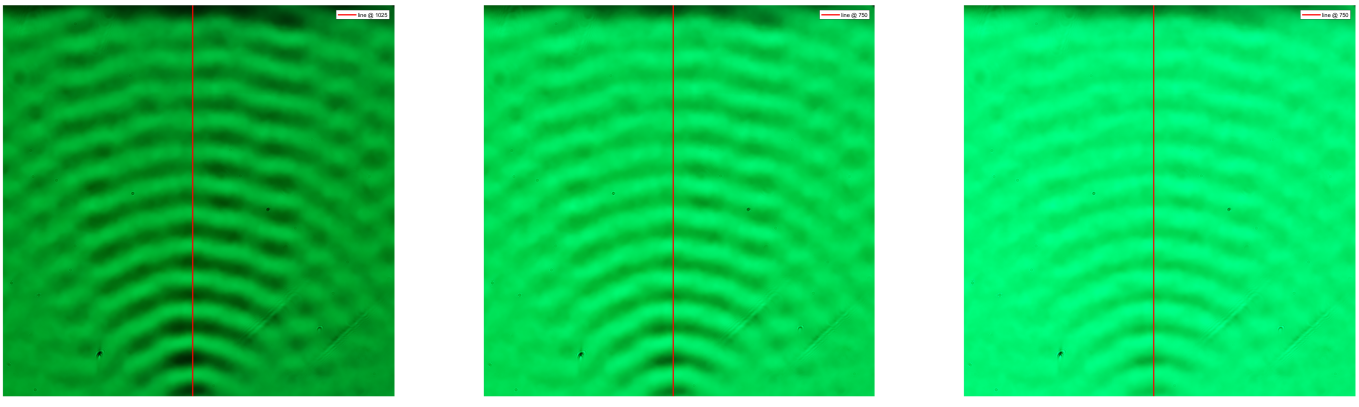

(a) 20% Duty cycle **(b)** 40% Duty cycle **(c)** 60% Duty cycle

Figure 3-4: Different duty cycles

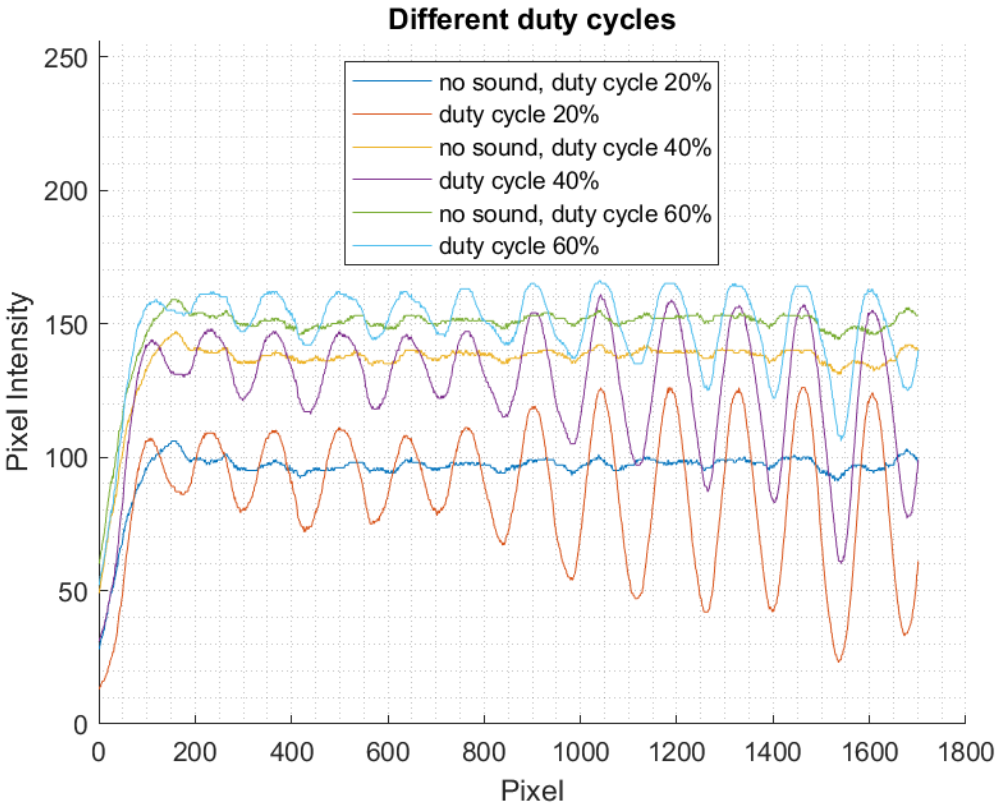

Figure 3-5: Influence of duty cycle on pixel intensity no phase offset, with and without sound

In Figure 3-5 one can see the pixel intensities across a vertical line originating in the source. Multiple line cuts have been plotted together for different duty cycles ranging 20% to 60%. One can see that the pixel intensities corresponding to the higher duty cycles are higher, as a result of the total amount of light being emitted is also higher. The contrast in the signal is highest however with the 20 % duty cycle.

3-4-3 Phase delay

Without varying the duty cycle of the signal the phase delay is varied from 0 to +90 deg. In Figure 3-6 one can see the result of turning on one row parallel to the optical axis. Row 3 on the bottom have been turned on with all phases set to zero. The phase difference between might be difficult to spot at first but using the bottom, and starting point of the acoustic signal is a good place to notice the phase offset. A red line is plotted over the schlieren images as to illustrate where the pixel intensities are taken along a vertical line for Figure 3-7.

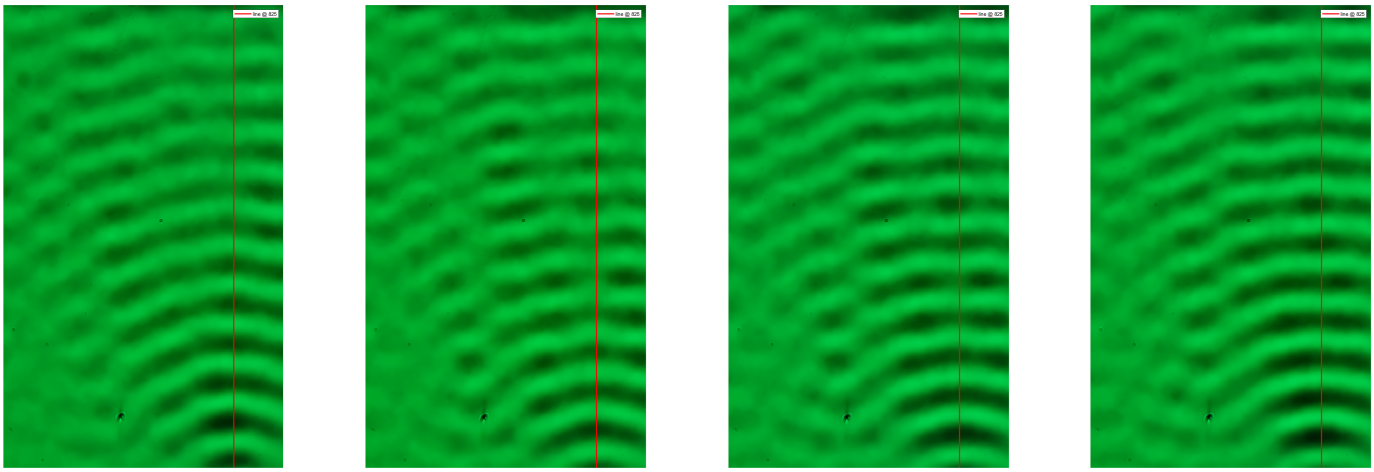

(a) +0 deg **(b)** +30 deg **(c)** +60 deg **(d)** +90 deg

Figure 3-6: Phase delay of a single transducer line

Dependent on the phase delay, the peaks shift in location with respect to each other, as can be seen in Figure 3-7. The amplitude of tends to decrease as the distance from the transducer increases. The amplitude of the shifted peaks is not constantly the same. The wavelength of the waves stay the same, independent of LED phase delay, as expected.

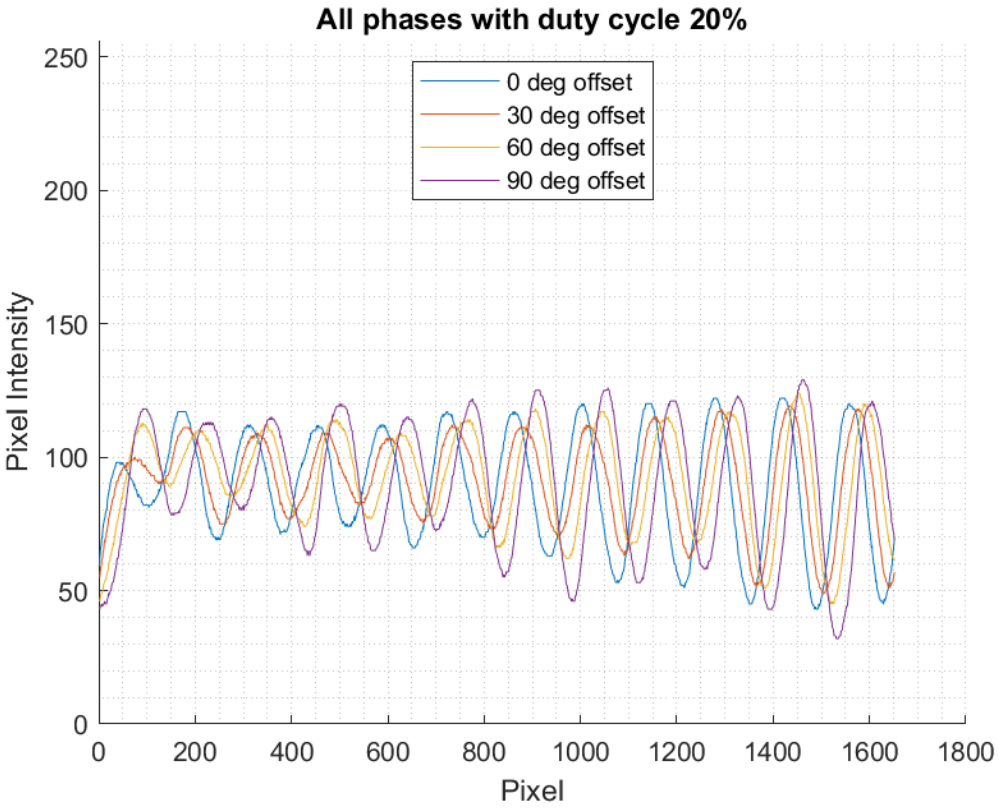

Figure 3-7: Influence of phase delay on pixel intensity

3-4-4 Light source frequency

Light source frequency 40kHz Setting the light source frequency exactly the same as the acoustic frequency, makes sure the light pulse is sent when the acoustic wave has travelled exactly one wave length. This gives the illusion that the wave is frozen. This allows the camera shutter time to be longer to capture many light pulses, since the acoustic signal is at the same location every time. A longer shutter time allows more light to fall on the image sensor and thus less light is needed. A travelling wave with the light source frequency at the acoustic frequency is illustrated in Figure 3-8. The travelling wave is a pressure perturbation, thus a pressure gradient wave is illustrated similarly to the pressure wave. To avoid confusing between the time and z-axis the illumination is drawn vertically. The travelling wave is indicated by the dotted lines. The captured intensity, a frozen image at the point of the light source, is illustrated as well.

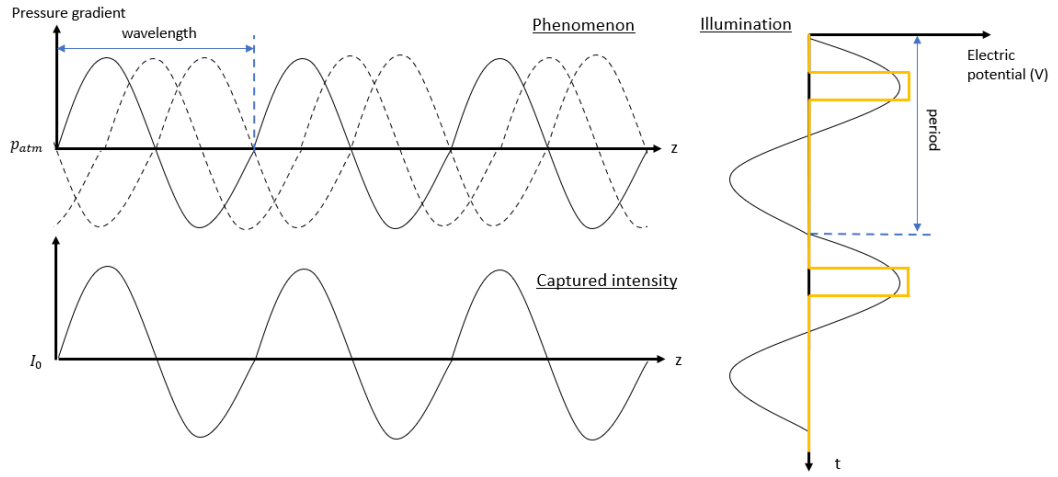

Figure 3-8: Travelling wave, light and acoustic the same frequency

A standing wave does not move but in space, but oscillate in their position between the high and low pressure gradient. Imaging this is illustrated in Figure 3-9. The captured intensity is exactly the same shape as the travelling wave, assuming a instant light flash. With a finite duty cycle however, the measured peak with a travelling wave is moving over distance z, while the the measured peak of the standing wave is only varying in intensity at the exact location.

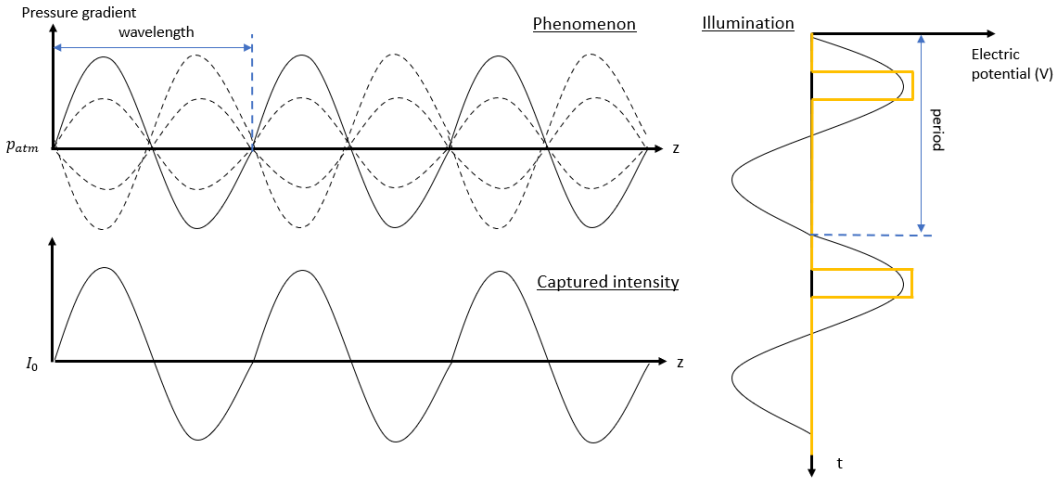

Figure 3-9: Standing wave, light and acoustic the same frequency

Light source frequency 80kHz Setting the light source frequency at twice the acoustic frequency and thus with twice the amount of pulses will visualise the travelling wave at positions spaced half a wavelength. The captured intensity of pulse 1 is indicated by the solid line, while the captured intensity of pulse 2 is indicated by the striped line. The captured intensity on the image sensor is a super position of both.

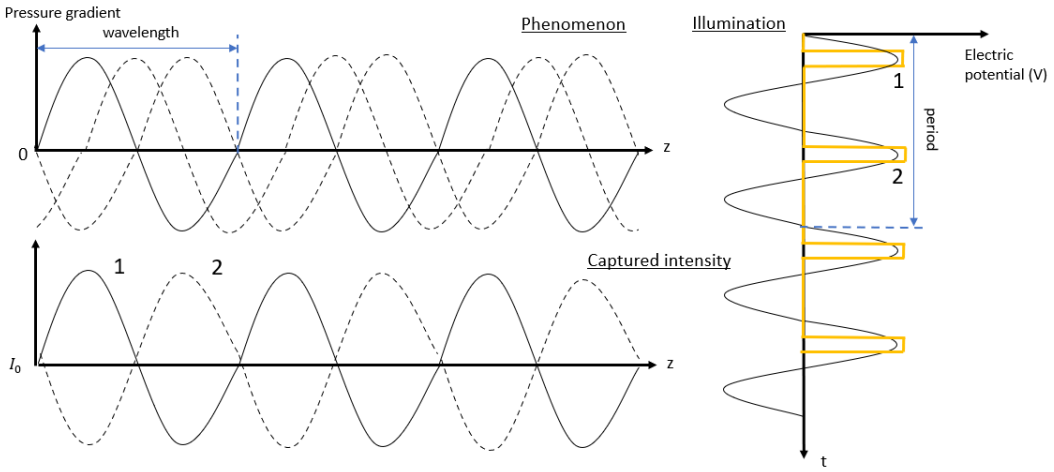

Figure 3-10: Travelling wave, light double the acoustic frequency

The light source frequency at twice the acoustic frequency visualising standing waves again yields the same result as a travelling wave. The captured intensity is superposition of both the results of pulse 1 and pulse 2.

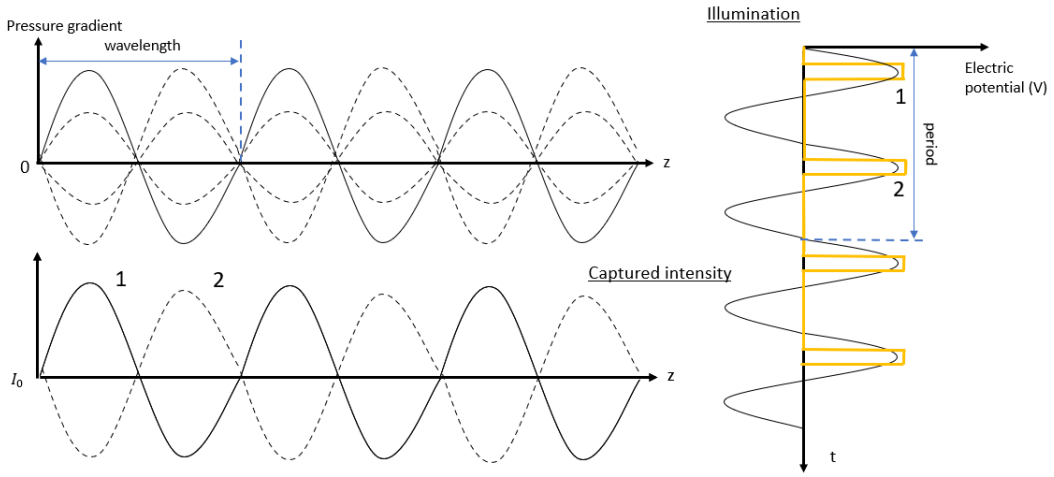

Figure 3-11: Standing wave, light double the acoustic frequency

Assuming a linear light intensity one would expect the super positions of the captured light from pulse 1 and pulse 2 to equal out. This is not the case as can be seen in Figure 3-12a. The vertical line cuts are plotted in Figure 3-13 with the red lines in Figure 3-12 indicating where the cuts are made. A sound dampening material has been attached to the top array to minimize reflections.

The peak to peak difference is a lot lower as expected with the 80kHz light source frequency. One can also see that the wavelength of the captured intensities at 80kHz are twice the wavelength of the intensities at 40kHz. The shape of the 40kHz sine wave steadily decreases, compared to the amplitudes of the Figure 3-7, which did not have a sound dampening material

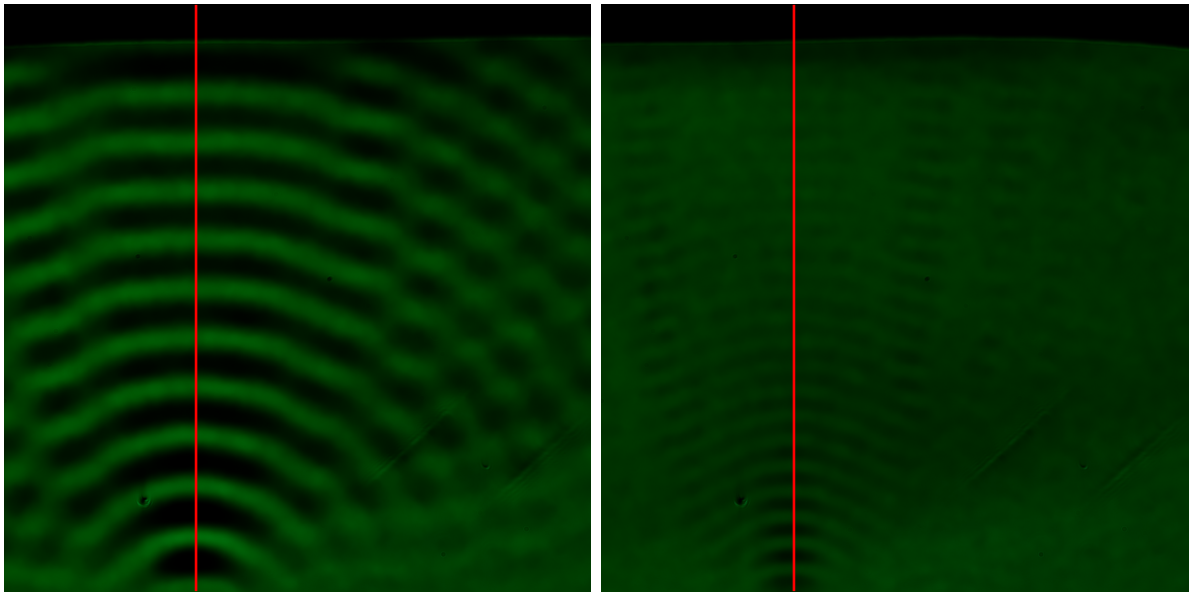

(a) Transducer line with light source at 40 kHz **(b)** Transducer line with light source at 80 kHz

Figure 3-12: Transducer line visualised with once or twice the acoustic frequency as a light source frequency

added to the top array.

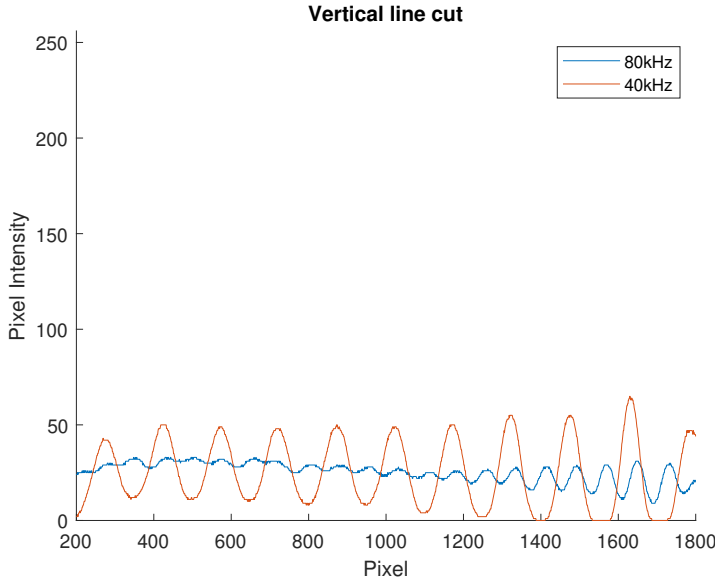

Figure 3-13: Vertical line cuts with plotted pixel intensity, with the light source at 40kHz and 80kHz

3-4-5 Camera settings

The camera settings are important for utilising the full potential of the image sensor. Properly capturing the schlieren image is important, but the image sensor does influence the interaction between the light and the acoustic field. The ISO and shutter times have just been studied for practical reasons and the results will be shortly shown here. The camera settings are not the focus of this report, thanks to the unavailable knowledge regarding the image sensor. To show the influence of the ISO, or the sensitivity to light of the image sensor, the ISO has been varied from 3200 to 10000. The effects for varying ISO are shown in Figure 3-14.

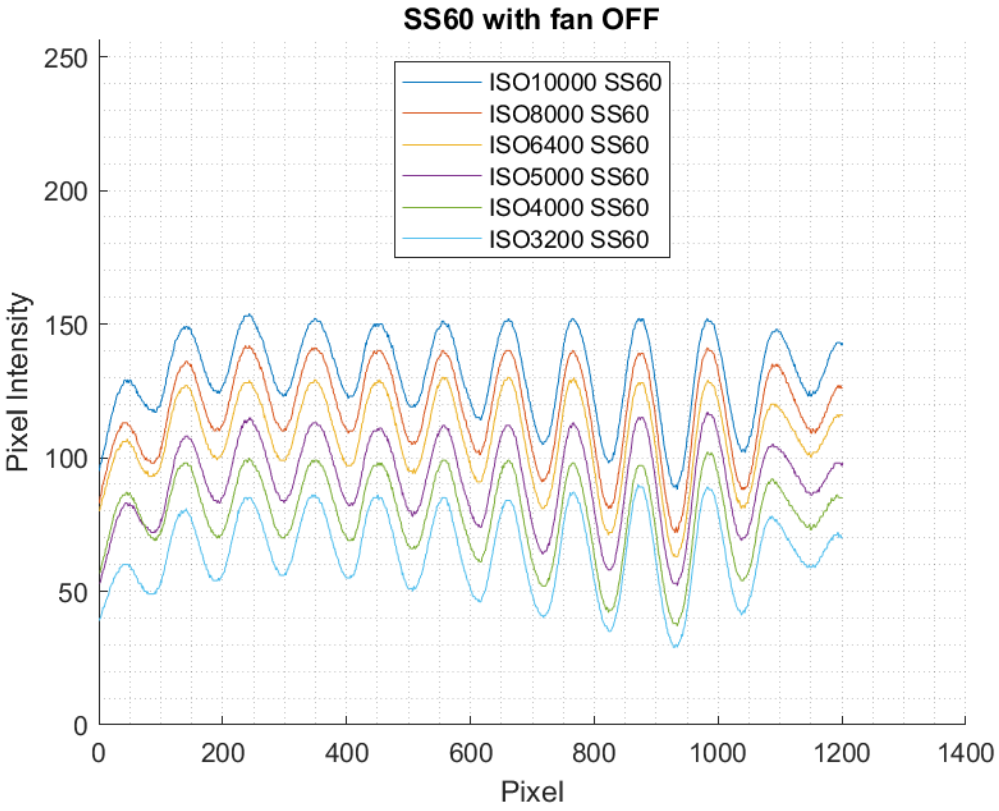

Figure 3-14: Different ISO levels at different shutter times

A higher ISO leads to a higher sensitivity in both the signal and the ambient light, but tends to introduce more noise. The overall shape of the sin wave remains the same independent on ISO. The amplitude does increase with a higher ISO. Reading the values from Figure 3-14 and looking at the largest amplitude of the ISO10000 line it is 64, while the largest amplitude of the ISO3200 line is 58. There is an increase in amplitude on the signal with the higher ISO but less than 15%. The mean intensity value of the overall schlieren image goes up as the ISO increases, as expected.

3-5 Discussion

In Figure 3-6 the peaks of the signals have different heights, while the acoustic signal is the same. This could be the result of the interference between the acoustic wave and the reflections which can be visualised differently. This has not been investigated in this schlieren image. Figure 3-12 seems to be at much lower mean intensity than other similar images. This is due to the experiments taken at different days and times. The ambient light level could not be controlled and effected the mean intensity. The light source frequency does visualise a signal at double the frequency of the acoustic wave. Assuming that the intensities do not simply add together this could be the standing wave. Looking back at the assumptions made on acoustics and its effect on the refractive index, it could also be a temperature or density change.

Chapter 4

Acoustic field visualisation

4-1 Modelling light and acoustic field interaction

4-1-1 Model explanation

As explained in subsection 1-6-5, there are three main steps in constructing schlieren images from flow fields . The first, identifying and calculating the appropriate refractive index functions. Second, integrating these functions along the ling of sight and last, post-processing the integrals to obtain the correct image. For this report, a model is made to compare schlieren images with. How this model is constructed is explained below.

Coordinate system To streamline comparison of results and understanding of equations a coordinate system is set. The coordinate system of the rectangular acoustic levitator is used which is illustrated in Figure 4-1.

As is also illustrated that the origin is in the center of the acoustic levitator. The viewing direction from the point of view of the camera is such that xz-plane is visible. In a schlieren image, the z-axis will point up and the x axis will point from right to left. Often a bar scale is added to a experimental schlieren image, which represents the x and z directions. The length of the bar scale represents 10mm. The optical axis is parallel to the y-axis and assumed to be the same.

Piston model The transducer pressure waves from each transducer together form the acoustic field. A simple way to calculate the incident far field is the piston model [27]. The complex acoustic pressure field from one transducer can be calculated using Equation 4-1. The constant P_0 is a constant that defines the transducer output efficiency while V is the peak-to-peak signal amplitude.

$$p(\mathbf{r}, t) = P_0 A \frac{D_f(\theta)}{d} \exp i(kd + \omega t + \phi) \tag{4-1}$$

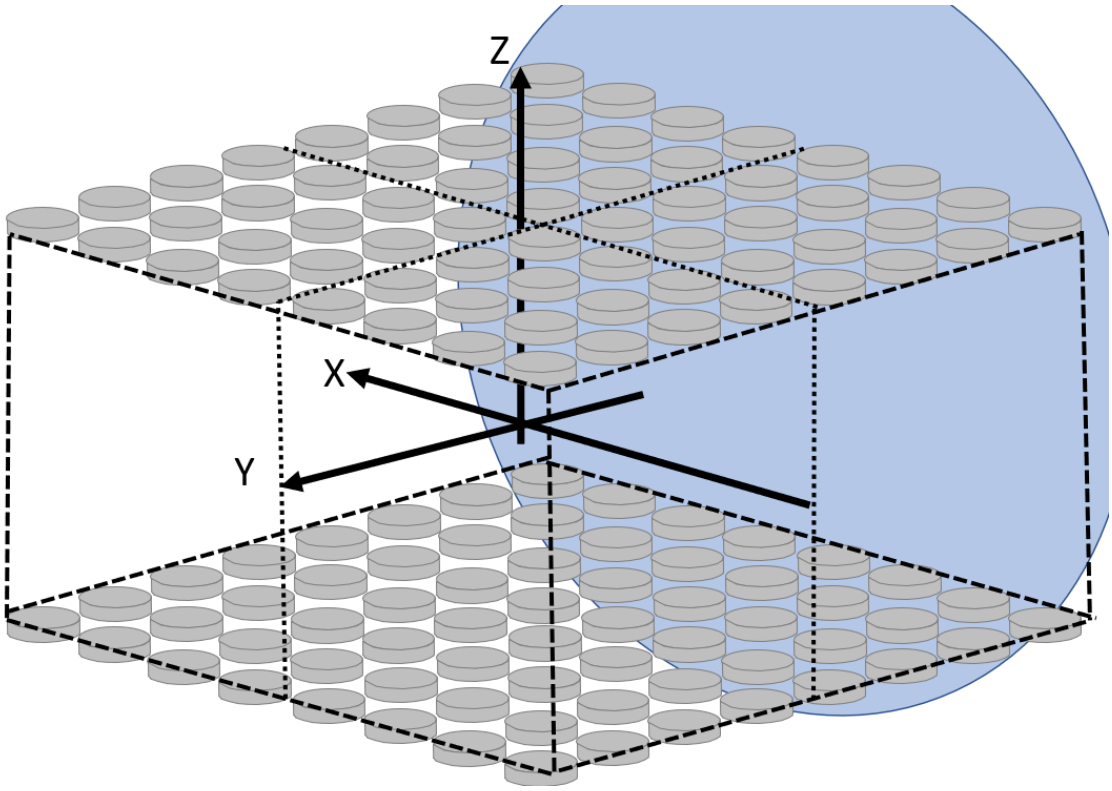

Figure 4-1: Coordinate system

The far-field directivity D_f, is given in Equation 4-2, and is dependent on the angle between the normal vector from the transducer surface θ and a point in space $\mathbf{r}$. Divergence of the pressure is accounted for dividing the directivity by d, which is the distance to point $\mathbf{r}$.

$$D_f(\theta) = \text{sinc}(\text{ka} \cdot sin(\theta)) \tag{4-2}$$

The total acoustic field can be calculated for the volume between the two arrays, in which $\mathbf{r} = (x, y, z)$ using Equation 4-3. The transducer is given a time dependent phase, which can also be written in Equation 4-1. The phase delay constant ϕ is added, but assumed constant and equal for all transducers.

$$p(\mathbf{r}, t) = \sum_{n=1}^{n=N} Ae^{i(k\mathbf{r}+\omega t+\phi)} \tag{4-3}$$

Calculating refractive index field and integrating Each transducer is modelled as a point source with pressure p as presented in Equation 4-1. A finite grid centered around the origin is modelled. The grid has dimensions in x and y of 137.6mm and in z 6.9mm, with each grid element having size of 1.075mm. This is such that exactly eight grid elements go into one wavelength. This grid and grid element size has been found by trial and error and was limited by the computational limits. Once the complete pressure field is known the gradient field $\frac{dn}{dx}(\mathbf{r})$ can numerically be calculated. A straight line integral is numerically taken across the

y-axis to get the image intensity $\Delta I_m(x,z)$ for the modelled schlieren image, as is illustrated step-by-step in Figure 4-2.

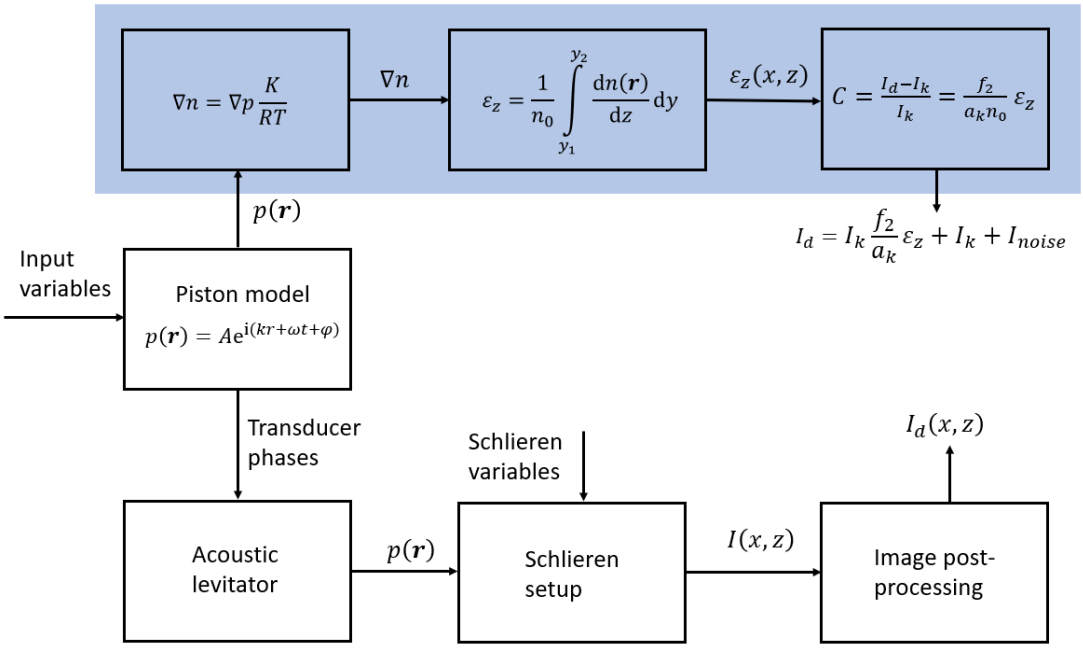

Figure 4-2: Block diagram for pressure to intensity for model schlieren image and experimental schlieren image

$$I_{d,z}(x,z) = I_k \frac{f_2}{a_k} \epsilon_z(x,z) + I_k \tag{4-4}$$

Image intensity The blue area indicates the schlieren model. Once ϵ_z is calculated, it can be used to calculate the contrast C and output intensity I_d, given in Equation 4-6 and Equation 4-4. While I_d is the illumination at the schlieren image, I_k is the illumination on the screen while a knife edge is present. The cut-off is assumed at 50%. While Equation 4-4 is given in literature [7]. The addition I_{noise}, as shown in Equation 4-5 seemed suitable to account for extra illumination of the image sensor due to ambient light and is used in the model.

$$I_{d,z}(x,z) = I_k \frac{f_2}{a_k} \epsilon_z(x,z) + I_k + I_{noise} \tag{4-5}$$

The output I_d can be compared to the experimental schlieren image.

$$C = \frac{\Delta I(x,z)}{I_k} = \frac{I_d - I_k}{I_k} \tag{4-6}$$

Post-processing experimental schlieren images for comparison Using Matlab, an experimental schlieren image can be compared to a modelled schlieren image. The experimental

schlieren images need to be post-processed to enable easy processing. First, the videos are converted into mean images by taking the mean intensity of a pixel over all the frames. This video is then cut to exclude features of the image that are non schlieren, such as parts of the levitator. The pixel intensities are on a 8 bit scale from 0 to 255. The intensity without a knife edge I_k is estimated by taking the mean intensity of the image.

Modelling the acoustic field is not an area of focus in this report, yet it does require some explanation. Distinguishing and understanding the differences in physical observations and the model can reveal imperfections of both.

4-1-2 Model results for transducer line

Taking the exact transducer phases that are sent to the levitator, the model not only allows for the calculation of the resulting schlieren images but also the pressure field and variables in between. While it is possible with the experimental schlieren setup to visualise the pressure gradient of a single transducer, a transducer line parallel to the optical axis, gives greater contrast. The modelled schlieren image result can be seen in Figure 4-3a, which can be compared to the corresponding experimental schlieren image in Figure 4-3b.

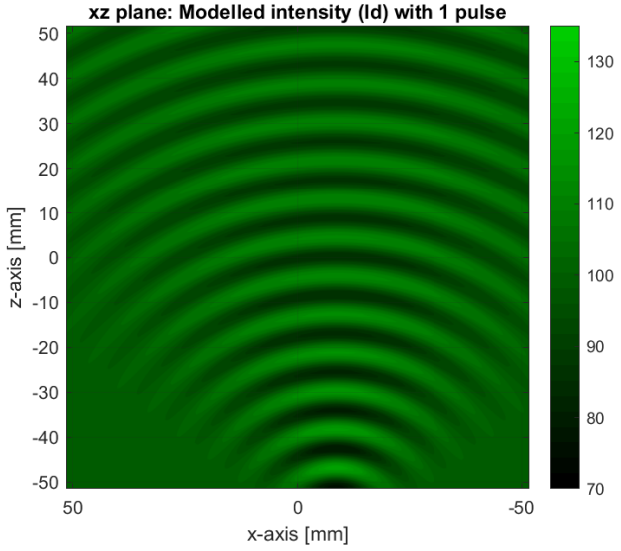

(a) Modelled schlieren image of transducer line

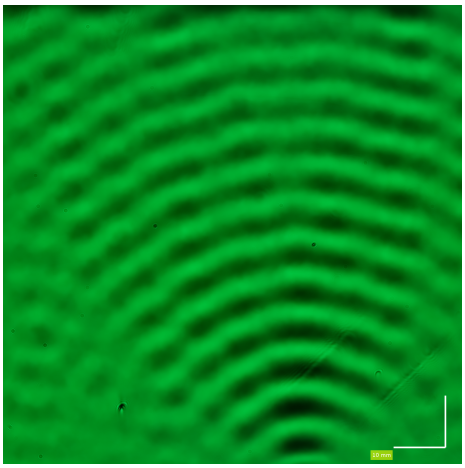

(b) Experimental schlieren image of transducer line

Figure 4-3: $\frac{dn}{dz}$ values along the y axis

Dependent on which transducers are on and what phase is set for each transducers it is possible to assume the pressure gradient field to have a constant $\frac{dn}{dz}$ along the optical axis. This assumption is valid for a transducer line where all the transducers have the same phase. The assumption is not valid for a more difficult complex field, such as the transducer phases optimized for a levitation point in the origin. To show this, the values $\frac{dn}{dz}$ for a single transducer line are plotted in Figure 4-4a. One can see that the values for $\frac{dn}{dz}$ are much more constant than the values plotted for a levitation point, which is plotted in Figure 4-4b. Both plots have all values plotted along a vertical line (parallel to the z-axis) at x = 0.

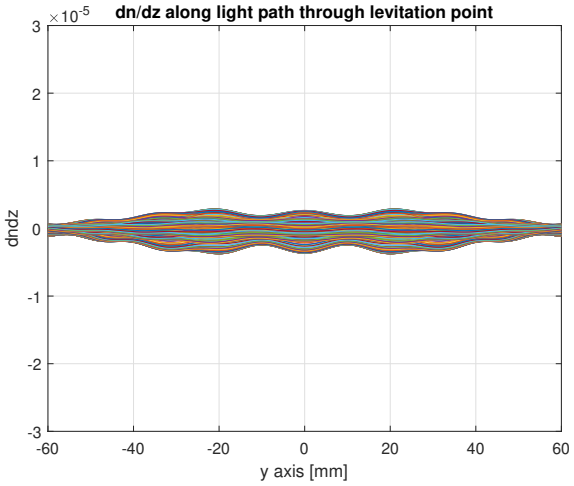

(a) $\frac{dn}{dz}$ values along the y axis, transducer line

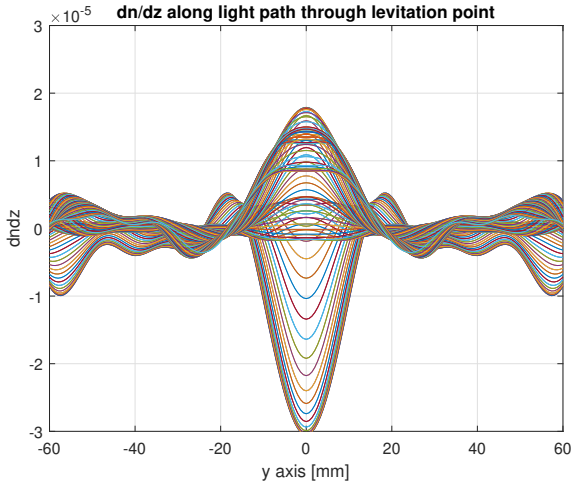

(b) $\frac{dn}{dz}$ values along the y axis, levitation point

Figure 4-4: $\frac{dn}{dz}$ values along the y axis

4-2 Visualisation of acoustic levitation related effects

This section will cover the visualisation of acoustic levitation related effects. This includes the pressure gradient of the acoustic field, but also unwanted effects such as reflections and air flow.

4-2-1 Visualisation of acoustic field

This section will go into the visualisation of the acoustic field. It will build up, from simple to more difficult acoustic fields, starting with visualising just one transducer to utilising the acoustic levitator to create multiple levitation points.

One transducer

A single transducer is visualised using the schlieren setup. The schlieren image can be seen in Figure 4-5a of which the line intensities across the red line are plotted in Figure 4-5b.

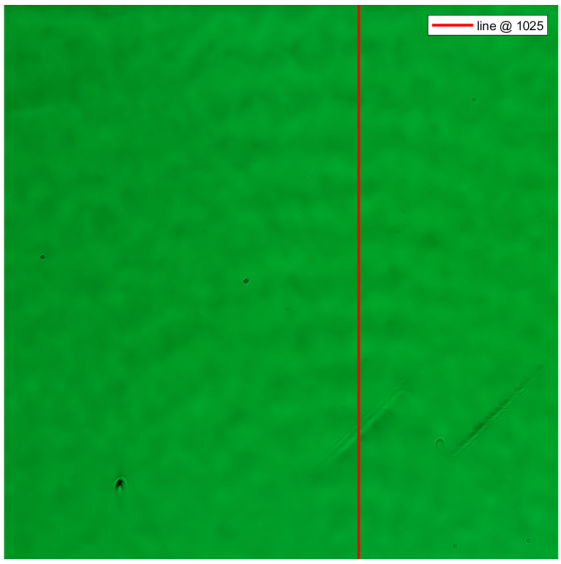

(a) Single transducer

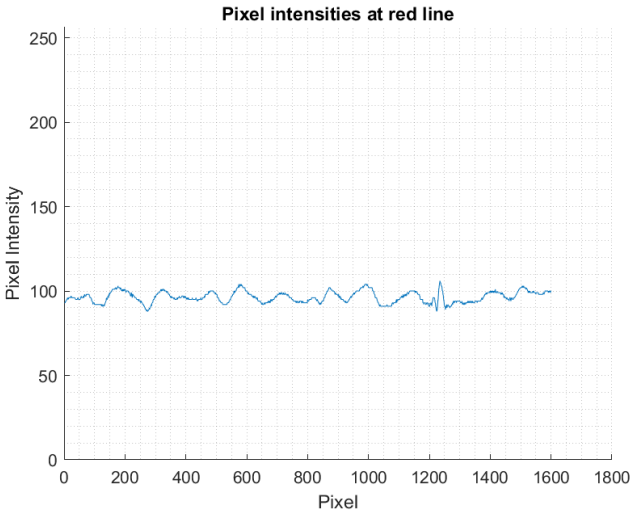

(b) Pixel intensities among vertical line cut of single transducer

Figure 4-5: Experimental schlieren image and pixel intensities along the vertical red line

Looking at the schlieren image, and the associated line cut, peaks and valleys can be identified that correspond to the wavelength of 40kHz. Even though peaks and valleys are visible, a sinusoidal shape cannot be identified in Figure 4-5b. The directivity can also be seen in the experimental schlieren image as the contrast is visible on the normal to the transducer surface, on the red line, but not on the sides. The sharp peak around pixel 1250 corresponds with the scratch on the experimental schlieren image.

One transducer line parallel to optical axis

A single line of 8 transducers parallel to the y-axis is visualised in Figure 4-6a. An illustration of which transducers are switched on, all with the same phase, is shown in Figure 4-6b. Note that the X',Y' and Z'-axis are not the same as the x, y and z-axis named in Figure 4-1 but are parallel to them and have the same direction but are used for ease of illustration.

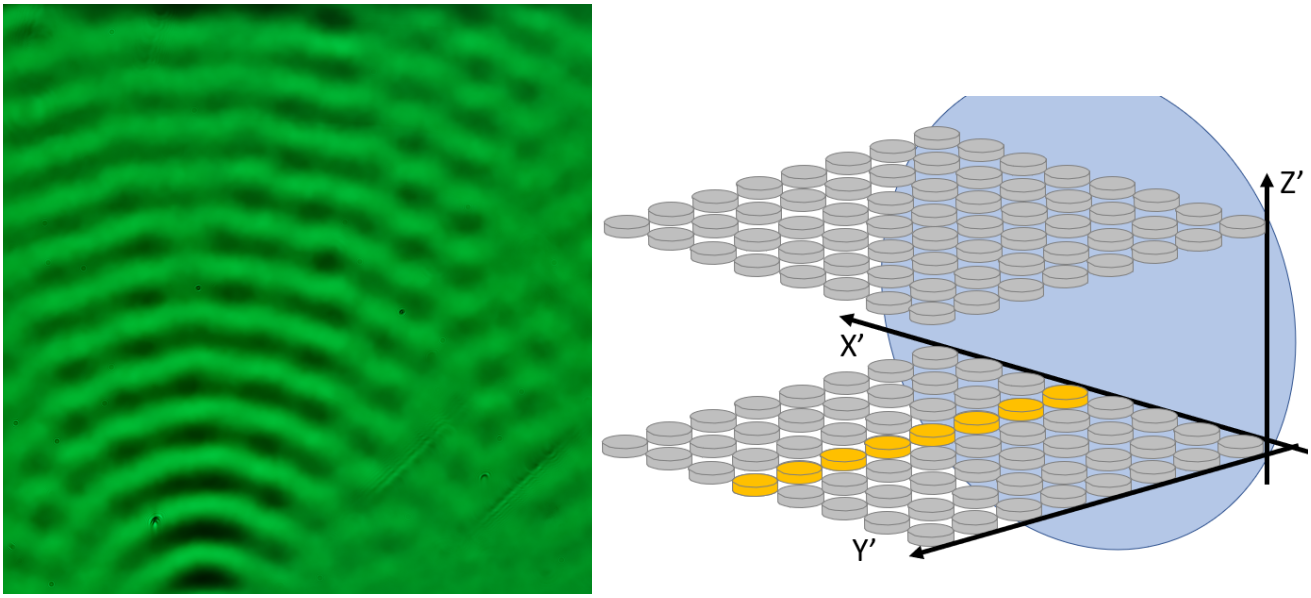

(a) Parallel transducer line 5, schlieren image **(b)** Parallel transducer line 5, illustrated

Figure 4-6: Bottom transducer line parallel to optical axis

One can clearly see the highest intensity can be seen closest to the transducer at the bottom of Figure 4-6a. The intensity of the waves decreases as the distance is further away from the source. The intensity also gets less, the further away from the normal of the transducer surface, clearly showing directivity. On both sides of Figure 4-6a, but mainly the right side, one can see a checkerboard pattern, indicating an interference pattern with other acoustic waves. These must be reflections as there is no other acoustic source. There is also a decrease in intensity on the top side of the image, across from the transducer line hinting at destructive interference from reflections. This will be further discussed in subsection 4-3-2. Different transducer lines are shown in the appendices section A-3. No major differences are visible between different parallel transducer lines, except for the reflections.

One transducer line perpendicular to optical axis

A single line of 8 transducers is visualised that is perpendicular to the optical axis, and parallel tot the x-and X'-axis. The schlieren image is shown in Figure 4-7a and the illustration, to indicate the switched on transducers is shown in Figure 4-7b.

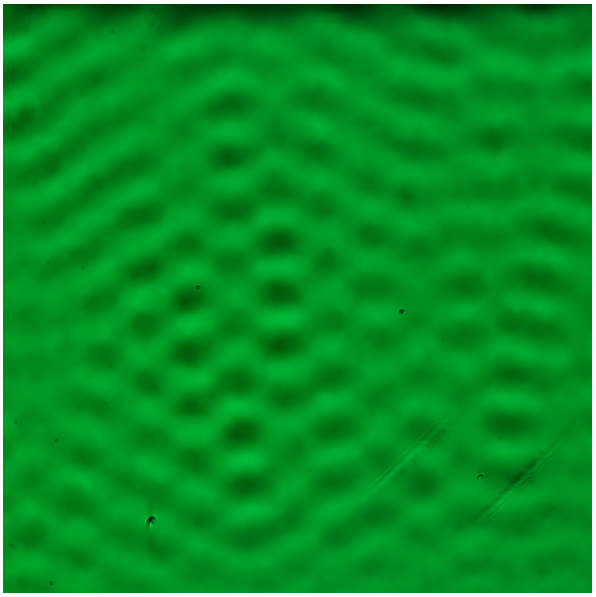

(a) Parallel transducer line 4, schlieren image

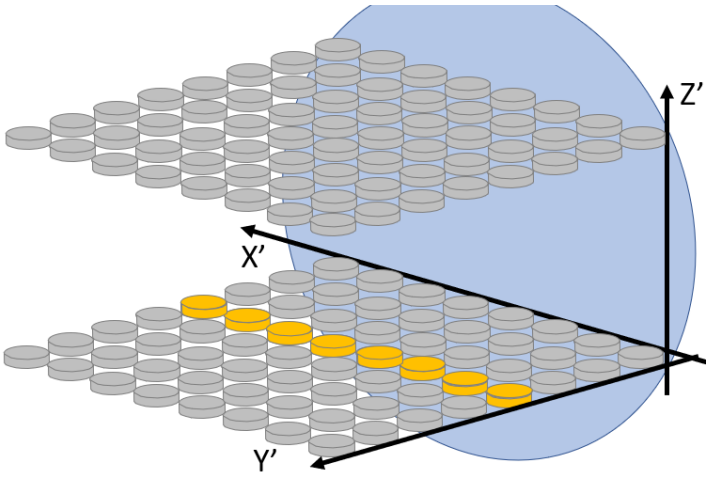

(b) Parallel transducer line 4, illustrated

Figure 4-7: Bottom transducer line perpendicular to optical axis

The schlieren image is taken in the same experiment as Figure 4-6a, thus the intensities can be compared. Less contrast is visible in this image since the acoustic field is shorter along the optical axis, thus less refraction is expected. A checkerboard pattern is visible, mostly in the middle. This is expected since the most interference between the acoustic waves from the different sources happens here. Different transducer lines are shown in the appendices section A-3. No major differences are visible between the different perpendicular transducer lines, except slight phase changes between some parts of the checkerboard pattern.

Two transducer lines parallel to optical axis

Two transducer lines parallel to the optical axis are switched on with identical phase. On the bottom line 4 has been turned on, while on the top array, line 1 has been turned on as is illustrated in Figure 4-8b. The accompanying schlieren image, can be seen in Figure 4-8a.

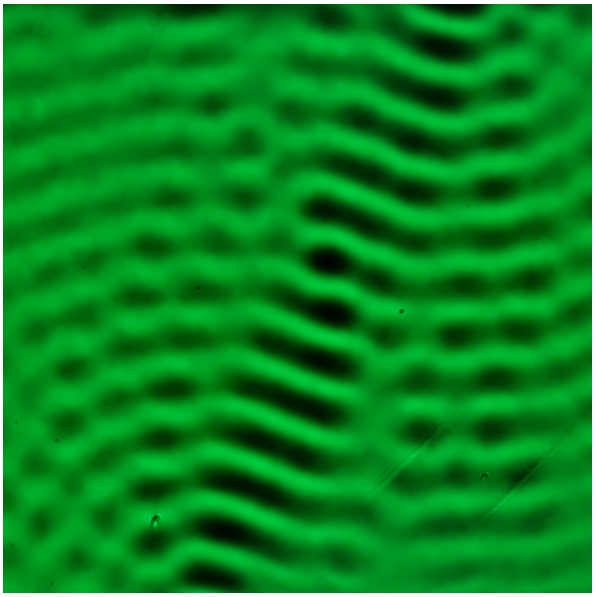

(a) Parallel transducer lines 4 and 1, schlieren image

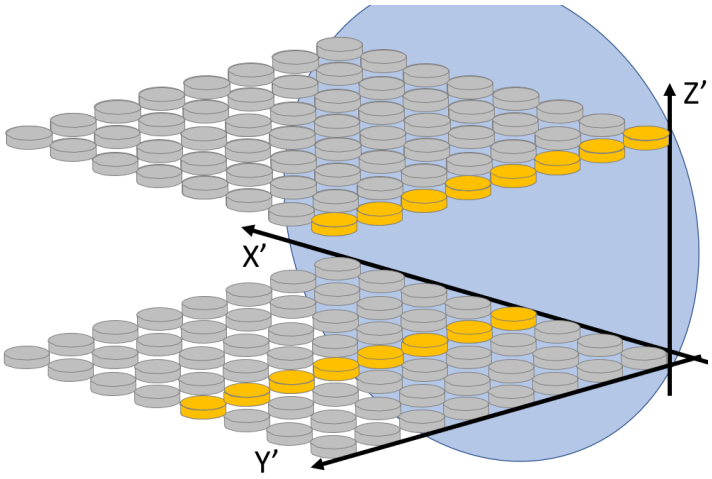

(b) Parallel transducer line 4 and 1, illustrated

Figure 4-8: Bottom and top transducer lines 4 and 1, parallel to optical axis

Comparing with the schlieren image of just the bottom line turned on, in Figure 4-6a, interference patterns can be seen. The radius of the waves emitted from their sources is still visible. The main addition is the clear distinction of the increased intensity on the tilted plane between line 4 and 1. The interference between the two acoustic waves results in a standing wave, which has an increased amplitude with respect to the travelling wave.

Switching the top transducer line from line 1 to 4 as is illustrated with Figure 4-9b with accompanying schlieren Figure 4-9a, with 0 degrees phase offset.

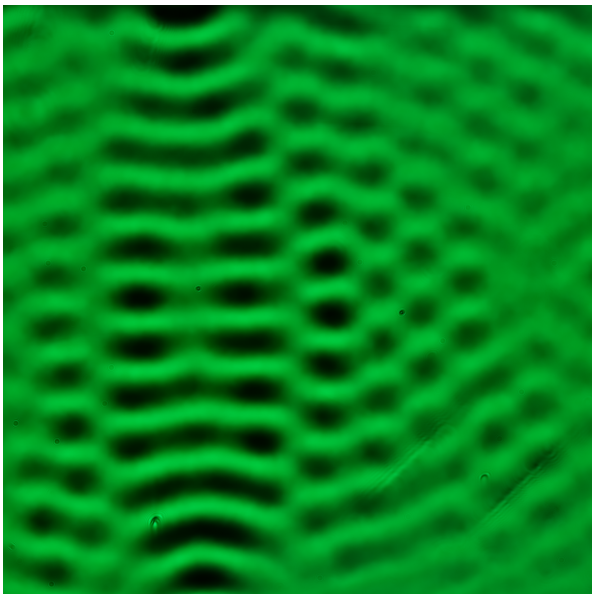

(a) Parallel transducer lines 4 and 4, schlieren image

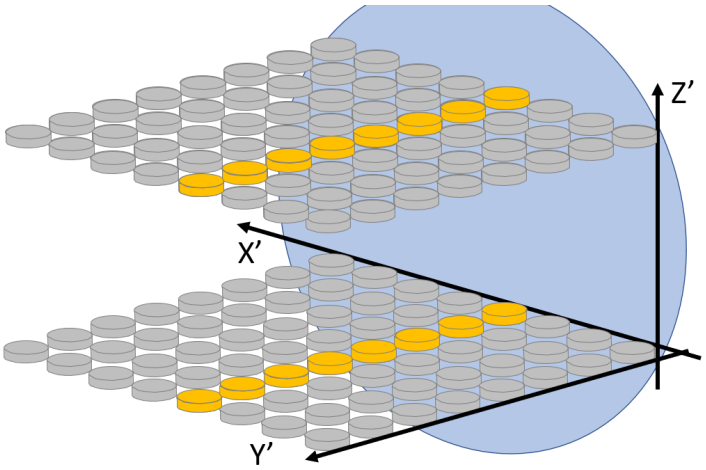

(b) Parallel transducer lines 4 and 4, illustrated

Figure 4-9: Bottom and top transducer lines 4 and 4 parallel to optical axis

The increased intensity between the transducer lines is shifted, since the lines are now right across from each other. The curved lines of the acoustic waves emitted from their sources can be identified more clearly on the right top and bottom of Figure 4-9a. In the middle of the standing wave, a decrease in intensity can be seen. This is caused by the used phase delay compared to the phase of the acoustics.

The importance of the phase delay starts to show. With a single transducer, or parallel transducer line, the complete acoustic wave is frozen at a slightly different location, as is shown in the last chapter in Figure 3-7. With standing waves, the appearance of the a standing wave in the schlieren image is dependent on the phase delay of the LED signal. The same transducers lines are turned on with all the same phases as in Figure 4-8b. Just a different LED frequency is used. Even though the contrast with a 80kHz light source frequency is lower than using the 40kHz that has been used before, the importance of the phase delay can still be seen in Figure 4-10. Assuming the pressure gradient is visualised with the 80kHz light source frequency. Hardly any pressure gradients are visible in Figure 4-10a, they can clearly be seen in Figure 4-10d.

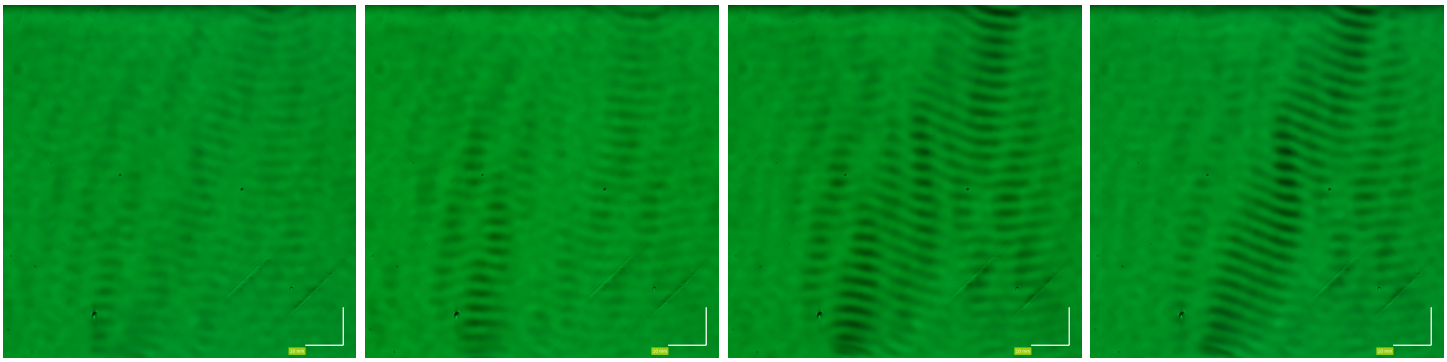

(a) +0 deg **(b)** +90 deg **(c)** +180 deg **(d)** +270 deg

Figure 4-10: Bottom and top transducer lines 4 and 4 parallel to optical axis, with varying phase delay with light source frequency at 80kHz

Two transducer lines perpendicular to optical axis

Two transducer lines perpendicular to the optical axis have been switched on with identical phase. Both on the top and the bottom array, line 4 has been turned on as is illustrated in Figure 4-11b. The accompanying schlieren image, with 0 degree phase offset can be seen in Figure 4-11a.

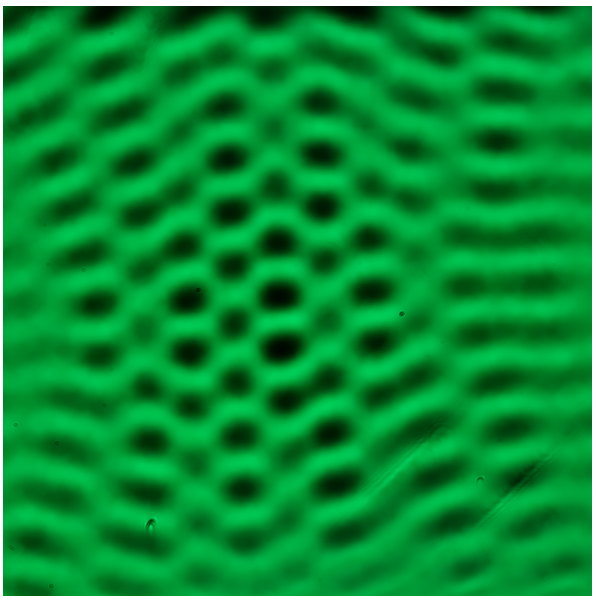

(a) Perpendicular transducer lines 4 and 3, schlieren image

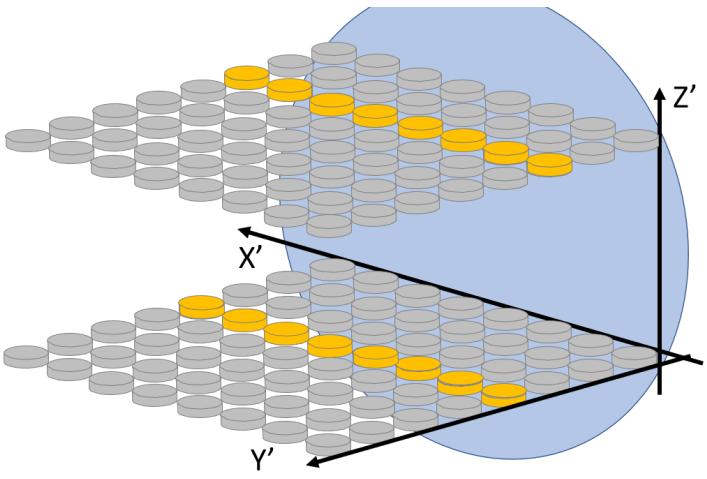

(b) Perpendicular transducer lines 4 and 3, illustrated

Figure 4-11: Transducer lines, top and bottom array, parallel to x axis visualised

Compared to Figure 4-7a, there is way more contrast in Figure 4-11a. This is caused by the interference of the acoustic waves, and the resulting standing wave having a larger amplitude.

4-2-2 Identifying trap location

To visualise the effect of creating particle traps at different locations within the acoustic levitator volume, 4 different positions will be shown. The positions will increase in 'complexity' regarding the symmetry around one or multiple planes. As the symmetry decreases regarding the particle positions, the accompanying transducer phases, and the accompanying acoustic field will decrease in symmetry as well. Asymmetry in the acoustic field might lead to a reduced ability to properly visualise the pressure gradient from just one viewing angle.

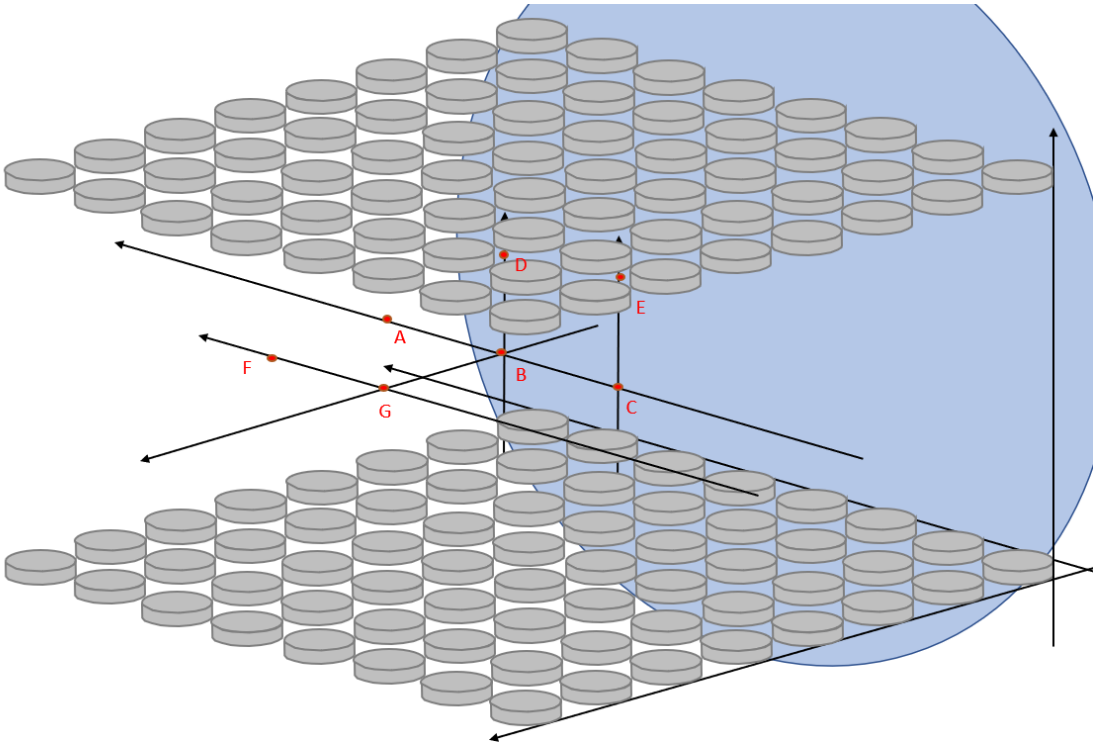

Figure 4-12: Illustrate different levitation positions within the levitated volume

	Letter(s)	Coordinates [mm]	Description
Position 1	B	[0, 0, 0]	Symmetric around xz-plane, Symmetric around yz-plane, Symmetric around xy-plane
Position 2	A, D, C	[20, 0, 0], [0, 0 ,20], [-20, 0 , 0],	Symmetric around xz-plane, Symmetric around yz-plane, Non-symmetric around xy-plane
Position 3	A, E	[20, 0, 0], [-20, 0 ,20]	Symmetric around xz-plane, Non-symmetric around yz-plane, Non-symmetric around xy-plane
Position 4	F, E	[20, 20, 0], [-20, 0 ,20]	Non-symmetric around xz-plane, Non-symmetric around yz-plane, Non-symmetric around xy-plane

Table 4-1: Description of 4 visualised levitation positions

Position 1 (B): [0,0,0] The most straight forward position will be position 1, in which 1 acoustic trap is placed at the coordinates 0,0,0. This is shown in Figure 4-13. The phases for all transducers are set such that a single levitation forms in the origin. This results in symmetry in the xz-, yz-, and xy-plane. The schlieren images are shown in Figure 4-13 with a phase delay of 180 degrees between Figure 4-13a and Figure 4-13b. The corresponding schlieren modelled pictures are shown in Figure 4-14, with the same relative phase difference between the two images.

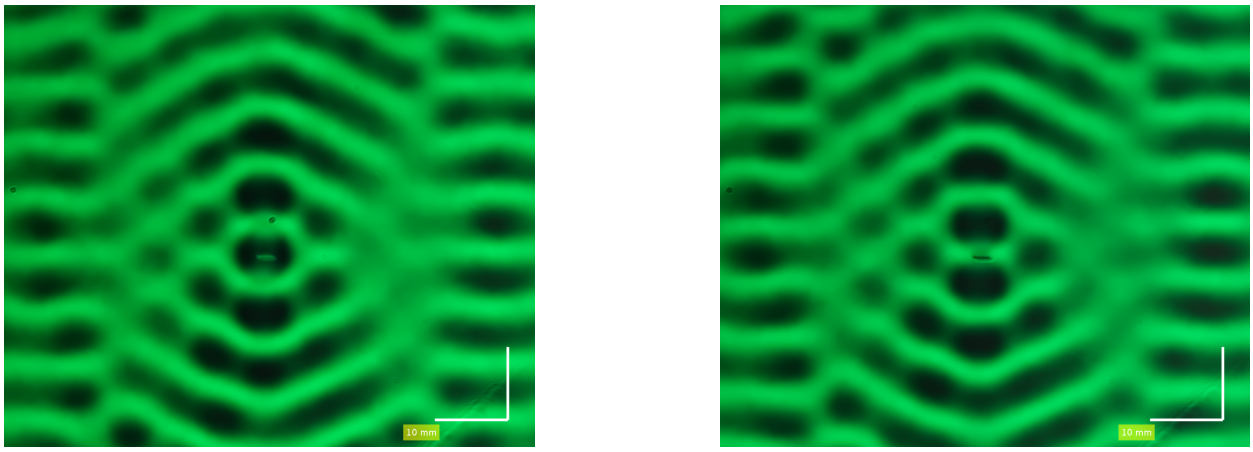

(a) Position 1, phase delay 0 deg

(b) Position 1, with 180 deg phase delay

Figure 4-13: Position 1, experimental schlieren image with different phase delays

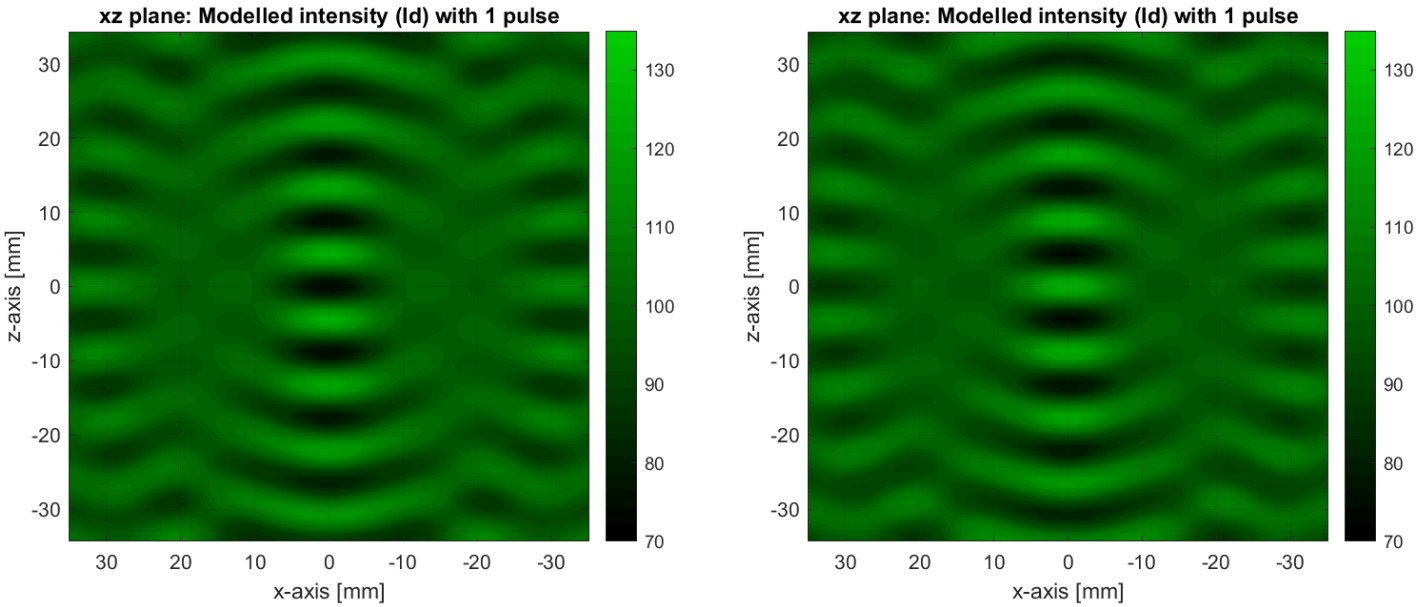

(a) Position 1, phase delay 60 deg

(b) Position 1, phase delay 240 deg

Figure 4-14: Position 1, modelled schlieren image with different phase delays

The bar scale of each experimental schlieren image shows a distance of 10mm in each direction.

The levitated object, which is flat, can be seen in the Figure 4-13, close to the middle of the image. As expected, with a phase change of 180 degrees, the previously low intensity spots have turned to high intensity and vice versa. This can be seen in both Figure 4-13 and Figure 4-14. The levitated particle sits in an area of either low or high intensity, dependent on the phase delay. The deviation is thus high with respect to the mean intensity. Since the pressure gradient is visualised this equals that the particle is located in an area of with a high pressure gradient, either positive or negative. The area just below and above the particle undergo a change from high to low intensity. Assuming a sinusoidal pressure gradient across the z axis, one can conclude that the particle itself is between two areas of either high or low pressure.

Position 2 (A, D & C): [20, 0.0, 0.0], [0, 20, 0] and [-20, 0, 0] Position 2 has the transducer phases optimized for 3 levitation points. These points are A, D and C, with coordinates [20, 0, 0], [0 0 20] and [-20, 0, 0] in mm, as also illustrated in Figure 4-12. Point A and C are located on the y-axis with the same distance from the origin and are thus symmetric in both the xz-and yz-plane. Point D is only shifted up in the z plane such that there is no symmetry in the xy-plane. The experimental schlieren images are shown in Figure 4-15 with a relative light source phase delay of 90 degrees between them. The corresponding modelled schlieren images are shown in Figure 4-16, also with a relative light source phase delay of 90 degrees.

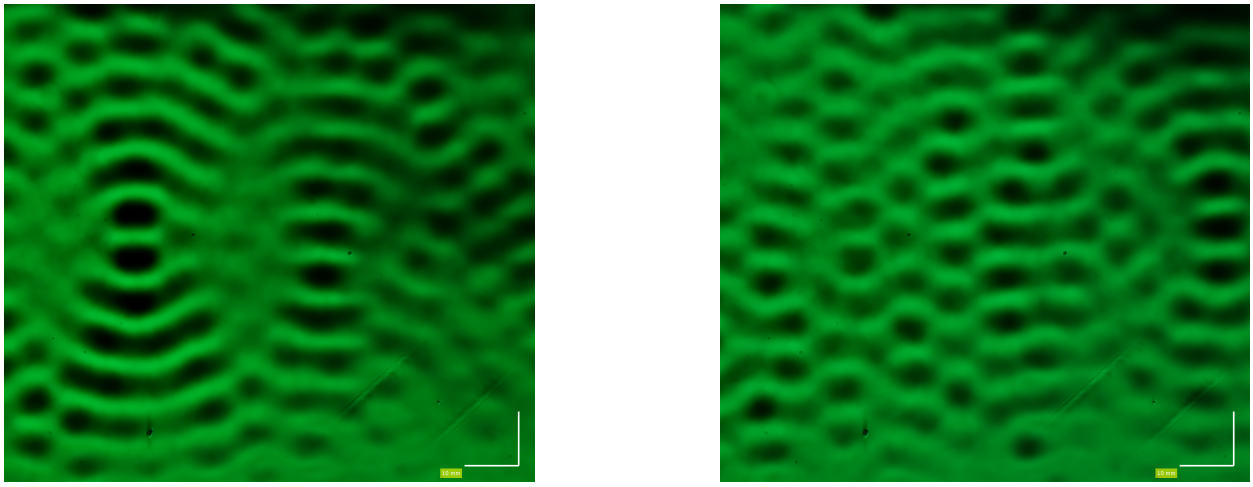

(a) Position 2, phase delay 90 deg **(b)** Position 2, phase delay 180 deg

Figure 4-15: Position 2, experimental schlieren image with different phase delays

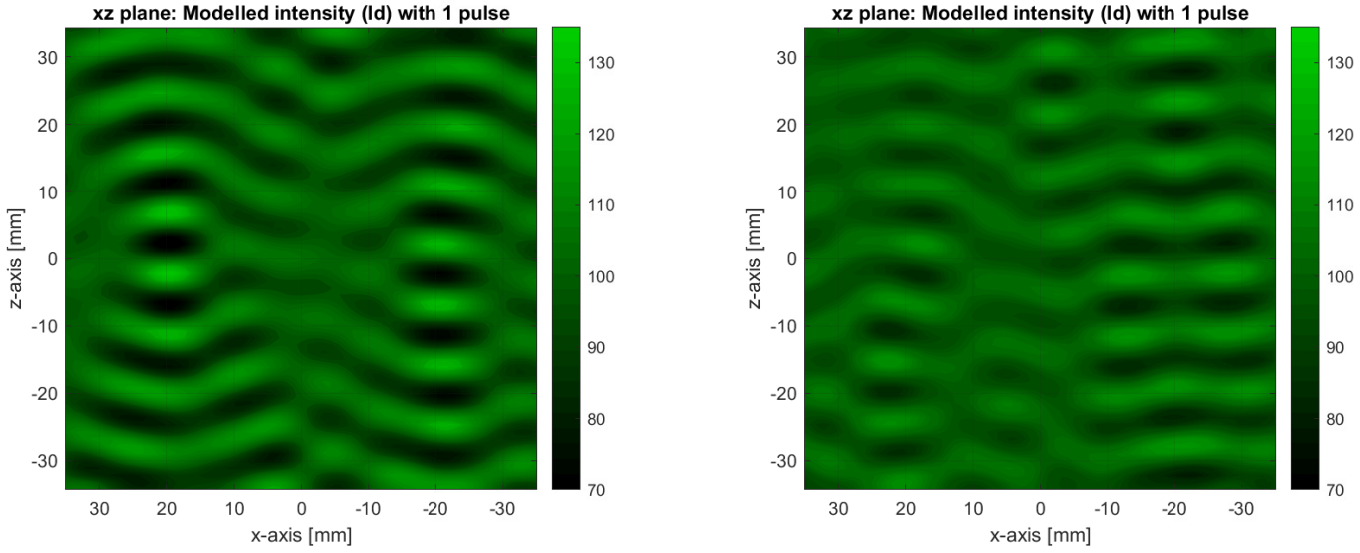

(a) Position 2, 0 deg phase delay **(b)** Position 2, 90 degree phase delay

Figure 4-16: Position 2, modelled schlieren image with different phase delays

Both traps A and C are properly visualised in Figure 4-15a and generally correspond with the model as shown in Figure 4-16a. Looking at the phases of the two points, shown in Figure 4-17, one can see that both A and C are on the same phase and are clearly distinguishable in Figure 4-15a. Point D has a lower pressure and is not as clearly visible at any phase.

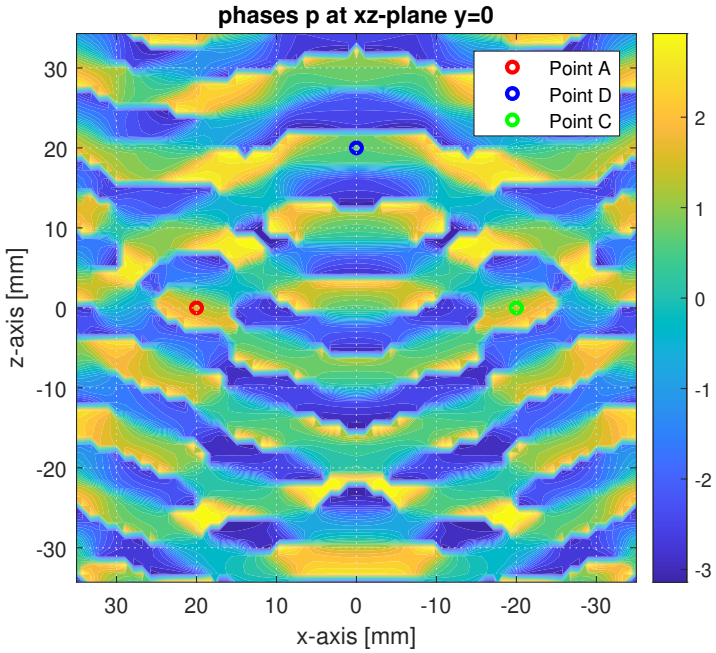

Figure 4-17: Phase of complex pressure field in xz-plane, y=0 for position 2

Position 3 (A, E): [20, 0, 0], [-20, 0, 20] Position 2 has the transducer phases optimized for 2 levitation points. These points are A and E, with coordinates [20, 0, 0] and [-20, 0, 20] in mm, as also illustrated in Figure 4-12. Both levitation points are on the same y-plane. Using the same phases as sent to the acoustic levitator the acoustic pressure field can be modelled.

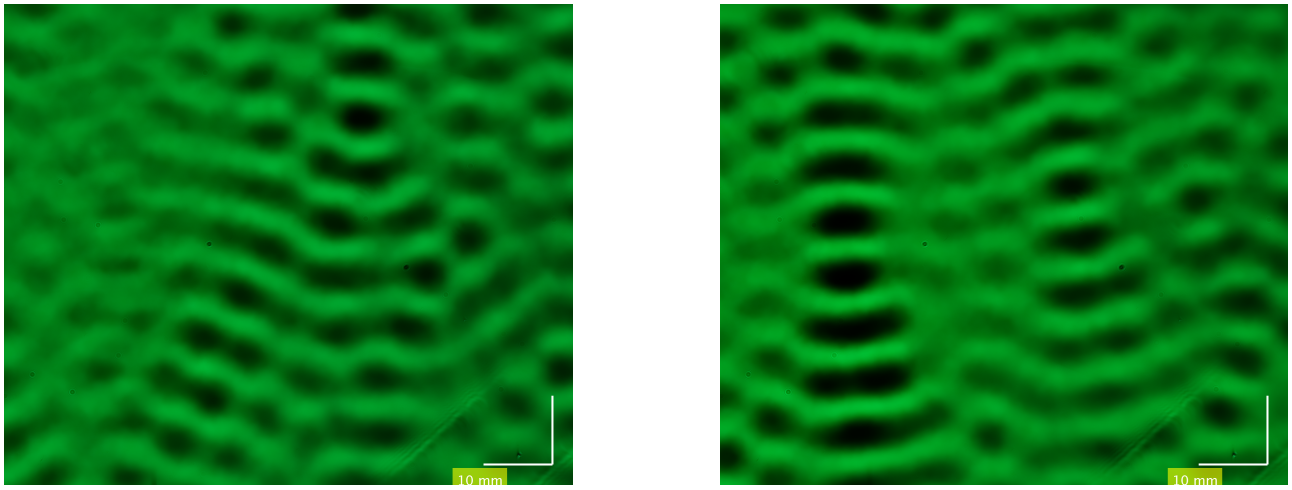

(a) Position 3, phase delay 30 deg **(b)** Position 3, phase delay 120 deg

Figure 4-18: Position 3, experimental schlieren image with different phase delays

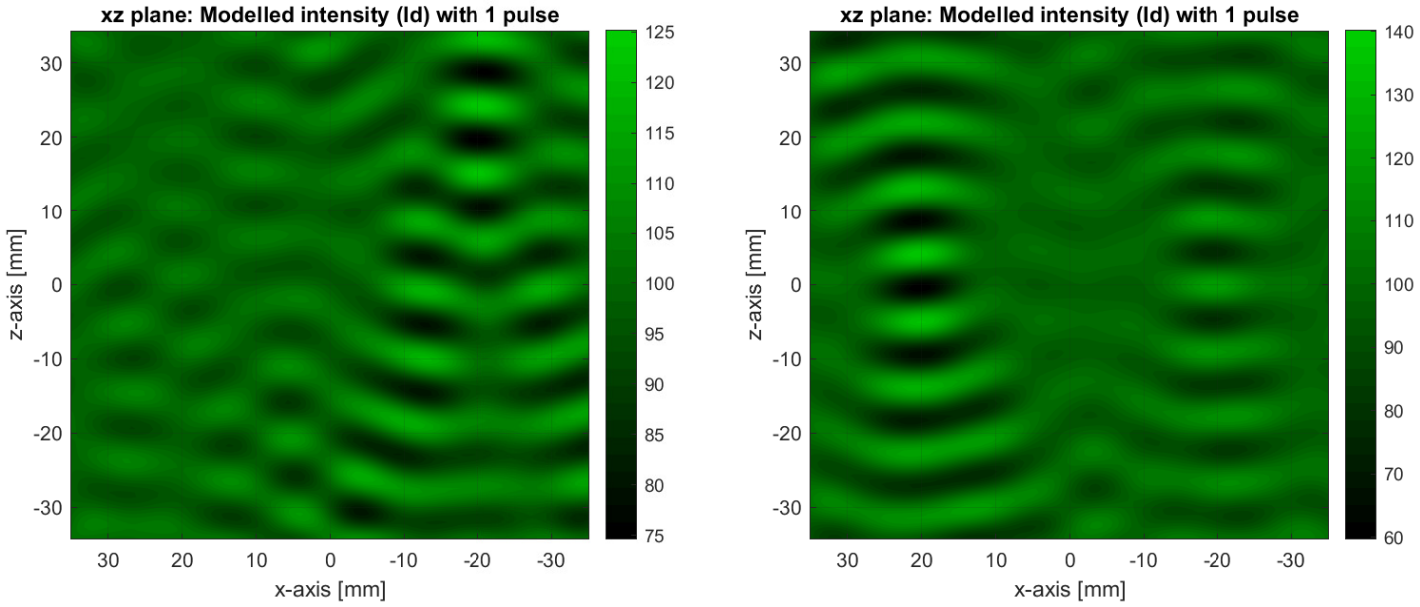

(a) Position 3, 60 deg phase delay **(b)** Position 3, 150 degree phase delay

Figure 4-19: Position 3, modelled schlieren image with different phase delays

Looking at the phases of the two points, shown in Figure 4-20, one can see that there is about a $\frac{\pi}{4}$ phase difference between the two points. Both in the experimental and model schlieren

images there is a 90 degree relative phase difference between the first and second schlieren image. Point E is visualised properly in Figure 4-18a and Figure 4-19b. While point A is visible using a relative phase delay of 90 degrees, in Figure 4-18b and Figure 4-19a.

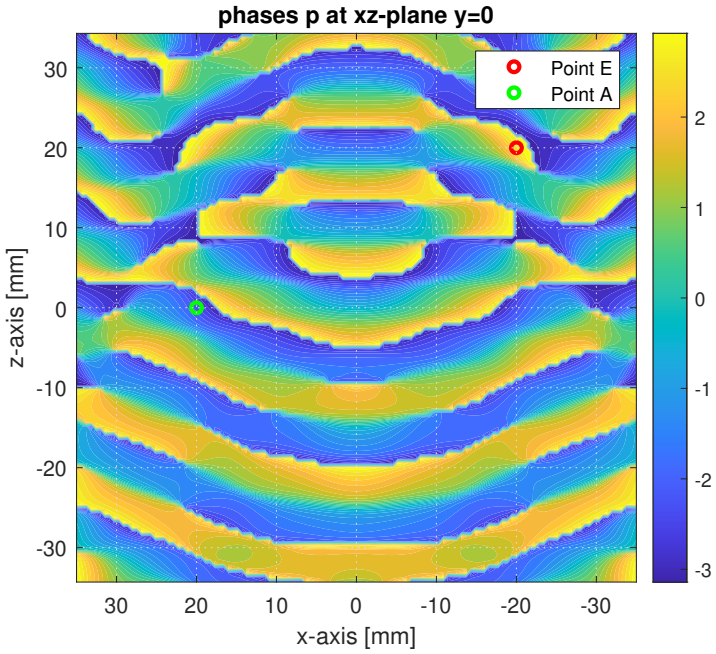

Figure 4-20: Phase of complex pressure field in xz-plane, y=0

Position 4 (F, E): [20, 20, 0], [-20, 0, 20] Positions 3, has the phases of all transducers optimized to be focused in two levitation points. The levitation points are F and E, in Figure 4-12. The experimental schlieren image is shown in Figure 4-21 with corresponding experimental schlieren image displayed in Figure 4-22. One can also see that both levitation points are visualised with the same phase delay, as can be seen in Figure 4-21b.

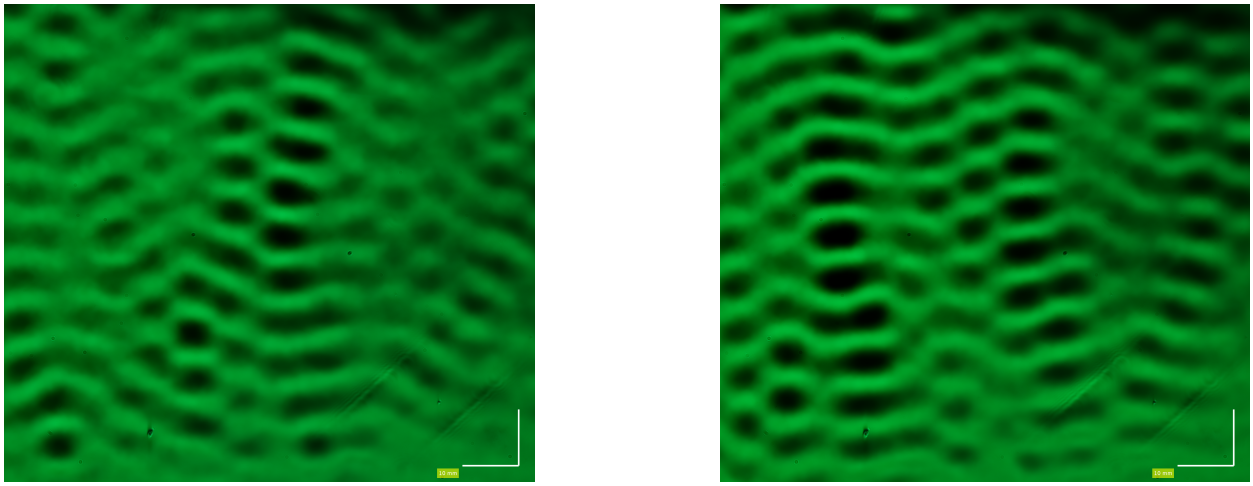

(a) Position 4, phase delay 30 deg **(b)** Position 4, phase delay 120 deg

Figure 4-21: Position 4, experimental schlieren image with different phase delays

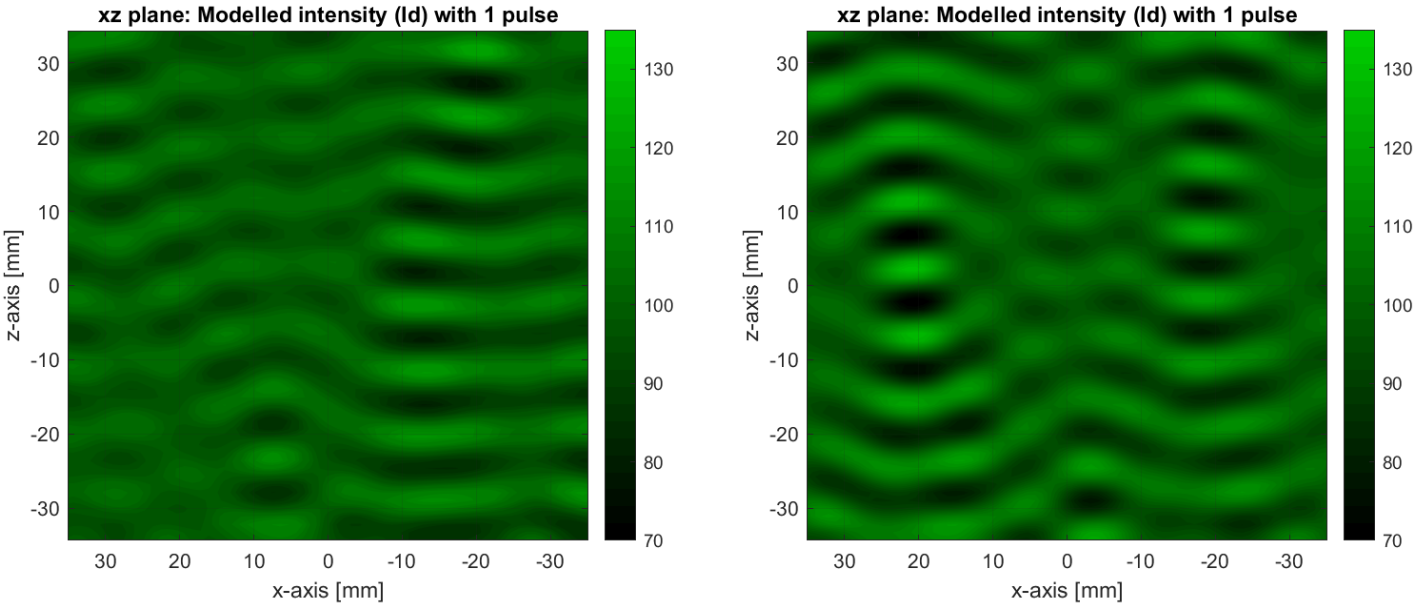

(a) Position 4, phase delay 0 deg **(b)** Position 4, phase delay 90 deg

Figure 4-22: Position 4, modelled schlieren image with different phase delays

In Figure 4-21a a strong intensity pattern is also visualised, which corresponds mostly with the modelled intensity in Figure 4-22a.

4-2-3 Identifying trap types

At the time or writing this report it was only possible to construct x-, y- and z-type traps on the acoustic levitators in use.

The Z-trap is visualised using a synced light source at two different frequencies. Copying the sound frequency at 40kHz, results in visualisation seen in Figure 4-23a. Doubling the light source frequency yields the result seen in Figure 4-23b.

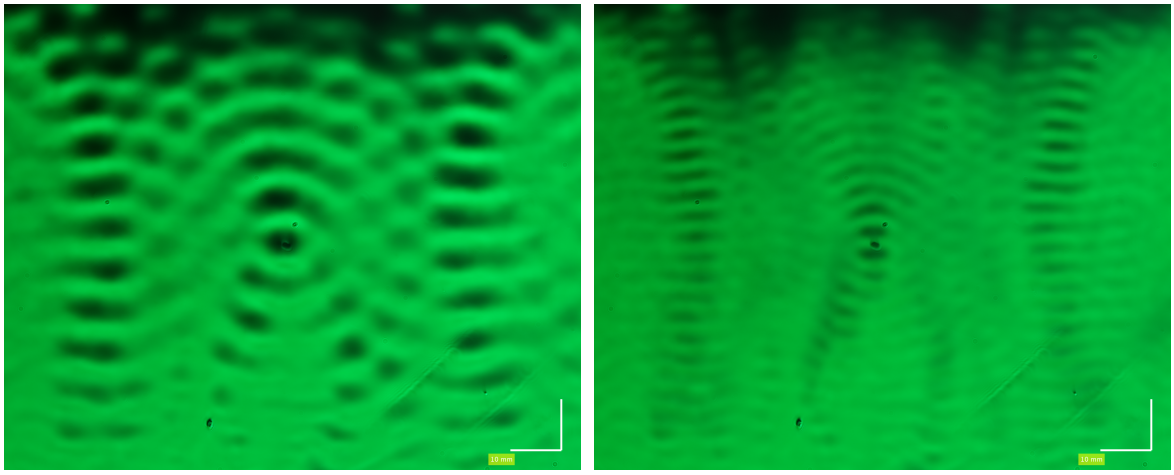

(a) Z-trap with 40kHz pulsed schlieren with levitated sphere

(b) Z-trap with 80kHz pulsed schlieren with levitated sphere

Figure 4-23: Z-trap schlieren image visualised with a light source frequency of 40 and 80kHz

The X-trap is also visualised using a synced light source at two different frequencies. Copying the sound frequency at 40kHz, results in visualisation seen in Figure 4-24a. Doubling the light source frequency yields the result seen in Figure 4-24b. The 180 degree offset between the right and left side of the array, which is needed for an X-trap, can clearly be identified in Figure 4-24a.

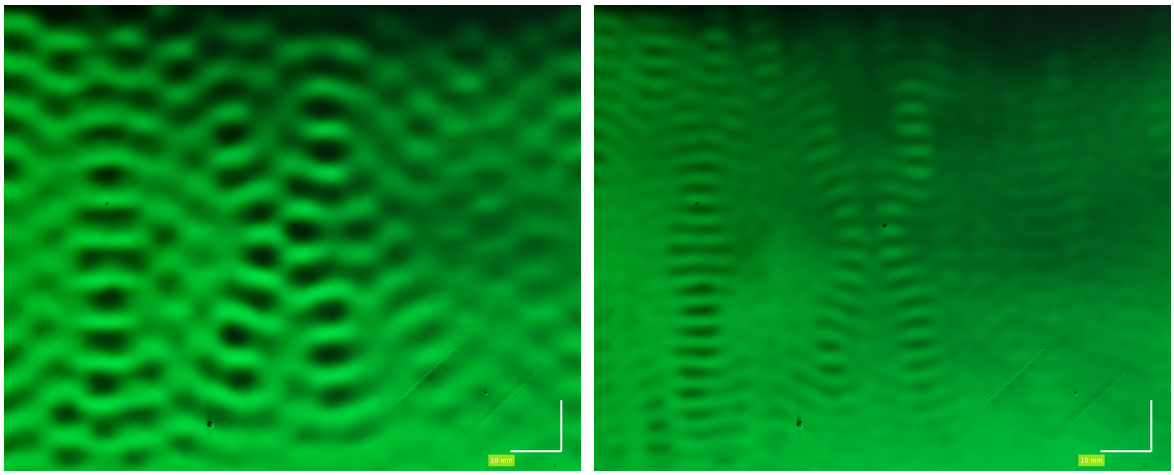

(a) X-trap with 40kHz pulsed schlieren

(b) X-trap with 80kHz pulsed schlieren

Figure 4-24: X-trap schlieren image visualised with a light source frequency of 40 and 80kHz

4-2-4 Discussion

Transducer lines One might notice that, especially with the perpendicular lines, that the transducer sources do not seem to be right across from each other. In post processing it was revealed that the camera, and it image sensor, were not completely square with the top and bottom array. This caused a tilt of the image.

Levitation positions While most main features seem to be recognisable, the experimental and the modelled schlieren image are not identical. There are a few main reasons for this. Reflections play a major role in determining the acoustic field, while they are not modelled. Despite taking the mean intensities of a movie, averaged effects of flow are still visible in the experimental schlieren images while this is not modelled, and thus won't show in the modelled schlieren image. The model takes a straight line integral, modelling schlieren with ray tracing yields more accurate results as has been mentioned in subsection 1-6-5. It is assumed that the double coincidence schlieren setup, simply yields twice the sensitivity without effecting the schlieren image. Especially for more complicated pressure gradient fields this assumption needs to be verified. The grid and grid element size was limited by computational limits, though could probably be improved if the Matlab script is improved. Using the model to visualise schlieren images made with a double light source frequency required the intensities to not be summed together. This is because, then, the intensities will cancel out. The fact that visualisations are made, might point to non-linearity in the image sensor. Non-linearity can occur in CMOS image sensor capturing light intensity [101]. This is not modelled. It might also point to temperature changes and thermal streaming. When presenting the experimental schlieren image the phase difference between the two images is the same as the corresponding modelled schlieren images. This is because exact starting phase of the transducers is unknown with respect to the clock signal that is sent to sync the light source.

4-3 Observation of parasitic effects

4-3-1 Influence of convection

While schlieren allows the visualisation of pressure gradients generated by ultrasound transducers it will also visualise any other phenomenon that changes the reflective index. Temperature fluctuations also cause a change in refractive index and can be visualized using the setup. On the rectangular setup are two main sources of high temperature; both the transducers and the amplifier's which are mounted side by side. Soon after switching the acoustic levitator on and observing the acoustic field with the schlieren setup one can see thermal plumes forming and rising. The thermal plumes forming and rising greatly affect the clarity of the schlieren image, as can be seen in Figure 4-26a. To get clearer schlieren pictures, and thus a better visualisation, the mean intensities are taken of a 20 second video, this can be seen in Figure 4-26b.

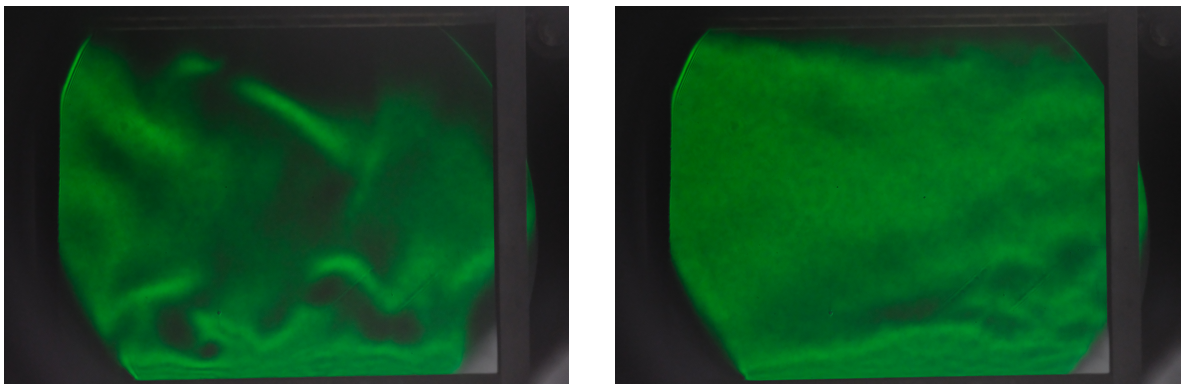

(a) Schlieren image, sound off fan off

(b) Schlieren image, sound off fan on

Figure 4-25: Schlieren image, fan off and fan on

Since direct feedback through camera readout is very useful, it would be beneficial to reduce the effects of the thermal convection plumes. A PC fan was added to the levitator on the positive y side. A fan shroud was designed to blow air over the arrays preventing the heat to rise slowly. Though this adds a bright layer on the bottom and a dark layer near the top array as can be seen Figure 4-26 and Figure 4-25b. While adding two areas of turbulent air, it greatly improved clarity for direct visual feedback on the monitor. Comparing the mean intensity images from a schlieren image with and without the fan on did not yield noticeable differences besides the areas containing the streams of air near the top and bottom array.

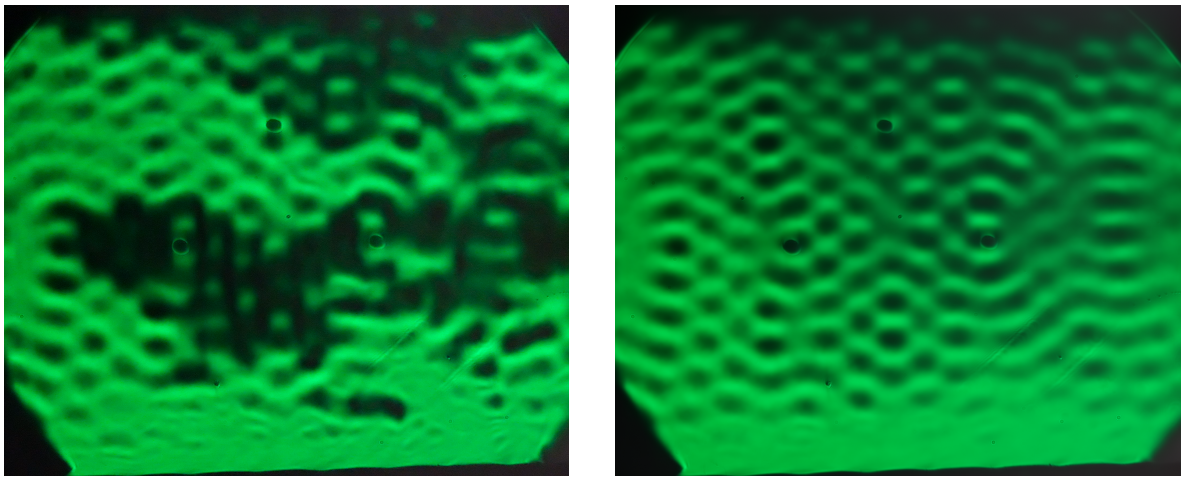

(a) Single frame of video **(b)** Schlieren image with mean pixel intensity

Figure 4-26: Mean intensity of video

While the airflow moved quicker causing it to be easily 'removed' by looking at the mean pixel values, the increase in airflow did cause an excitation of the particle at a specific frequency. A polystyrene sphere with a diameter of 3.62mm was levitated in a trap in the origin. Using the schlieren setup camera, while turning off the LED and switching on front light schlieren allows for a clear identification of the levitated sphere to do particle tracking in Matlab. For 15 seconds the movement of the particle is observed with the camera taking a video at 240 frames per second. The movement in both x and z can be observed easily since they are perpendicular to the optical axis. The influence of the fan on the particle movement can be clearly seen in Figure 4-27. One can see that the movement in x is affected more than the z movement, which is logical since a z trap is used, which has the highest stiffness in z.

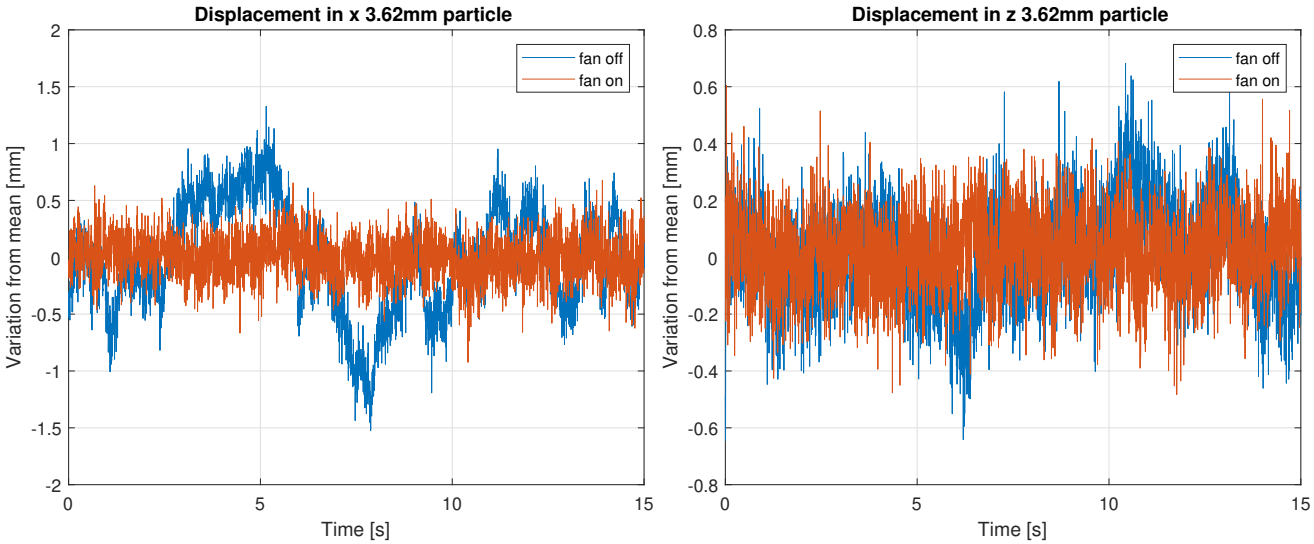

(a) Particle movement in x, fan on vs off **(b)** Particle movement in z, fan on vs off

Figure 4-27: Analysis of fan airflow on particle movement in time domain

The power spectral density (PSD) of the movement in x and z direction is shown in Figure 4-28. Clear peaks show up in the x direction at 26Hz and in the z direction at 21Hz while the fan is off. These peaks are not present while the fan is off, indicating that the fan, while not blowing air directly at the particle does cause an excitation at this frequency. The PSD of the x signal with the fan off is higher in the region under 10Hz. This is also visible in the PSD of the z data but to a lesser extend. Similar observations are seen with a smaller levitated object. A measurement with a ball diameter of 1.48mm and with a higher density has also been done. Since these measurements were done at 30fps they have been placed in the appendices in section A-4.

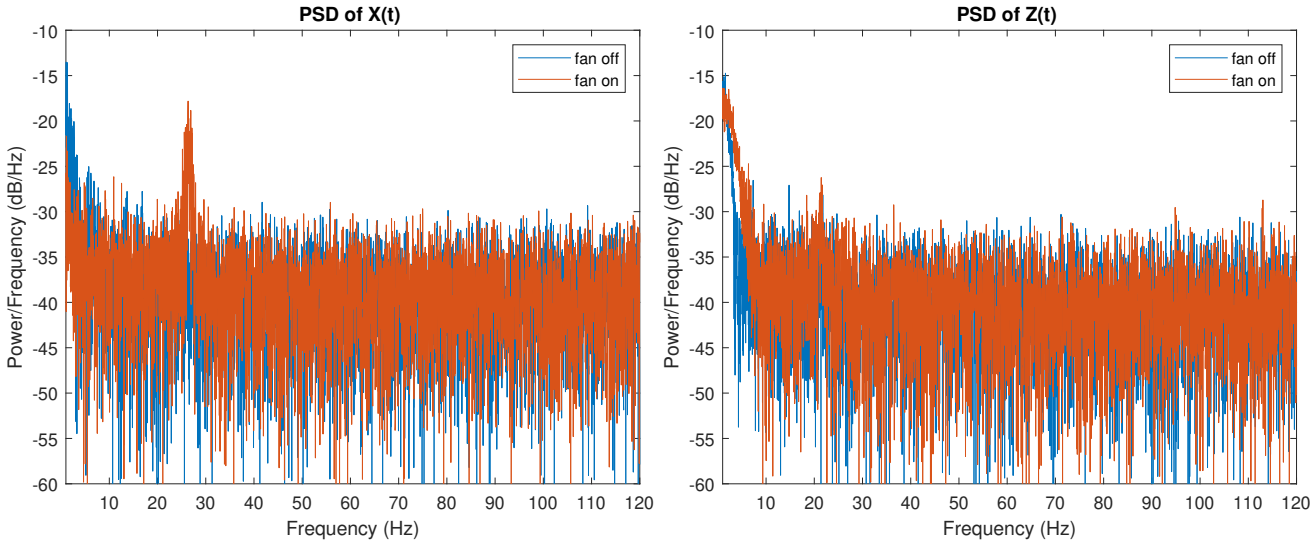

(a) PSD of movement in x, fan on vs off

(b) PSD of movement in z, fan on vs off

Figure 4-28: Analysis of fan airflow on particle movement in frequency domain

4-3-2 Influence of reflections

As noted in subsection 1-1-5 reflections can influence the acoustic field. Setting the duty cycle allows the visualisation of standing waves but also of travelling waves and thus most reflections. The main object against which the sound will reflect is the opposite array from which the sound is emitted. Reflections of sound coming from a single transducer can be visualised but have very minimal contrast, thus it was chosen to look at the reflections from a transducer line. The interference patterns of the sound waves, or checker board pattern, indicating reflections can be seen in both Figure 4-29a and Figure 4-29b on the left side. While not the acoustic levitator is unchanged in Figure 4-29a, sound dampening material is placed against the top array in Figure 4-29b.

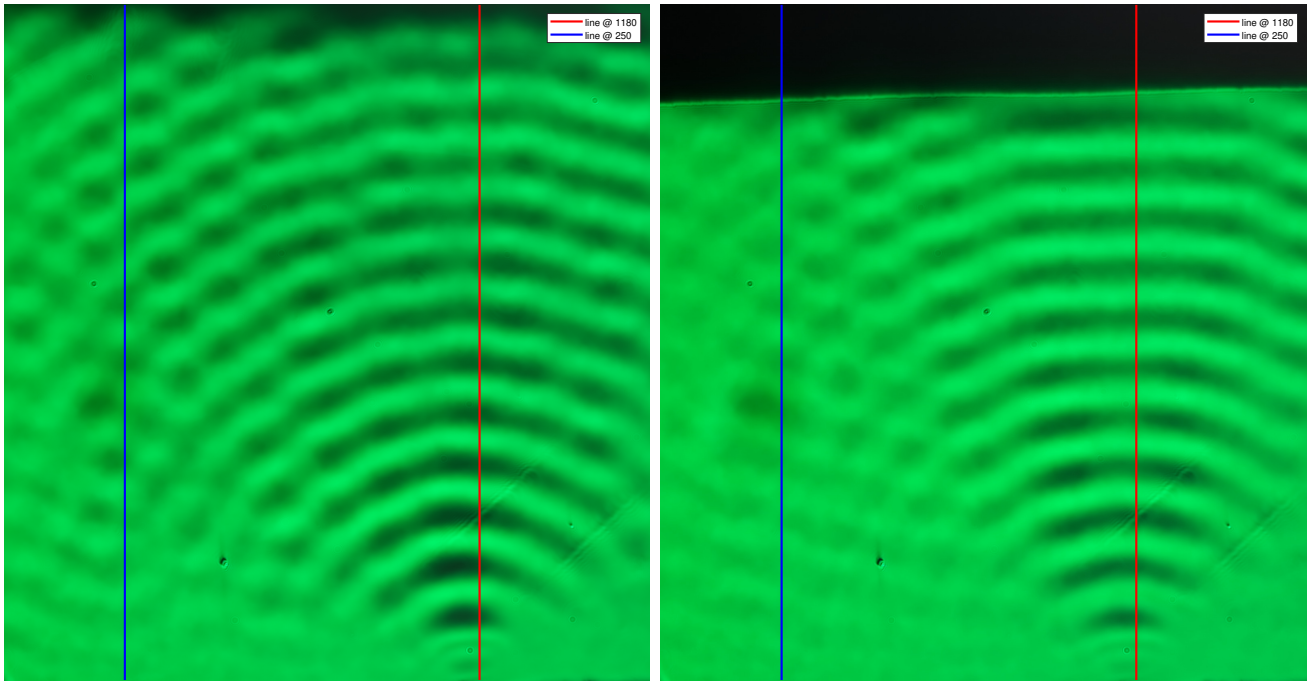

(a) No sound dampening material **(b)** With sound dampening material

Figure 4-29: Comparison of reflection against the top array with and without sound dampening material

Line cuts are made from both Figure 4-29a and Figure 4-29b at the lines indicated in red and blue. Analyzing Figure 4-30a, one can see that the addition of the sound dampening material prevents the decrease in the pixel intensity in the range of pixels 400 to 800.

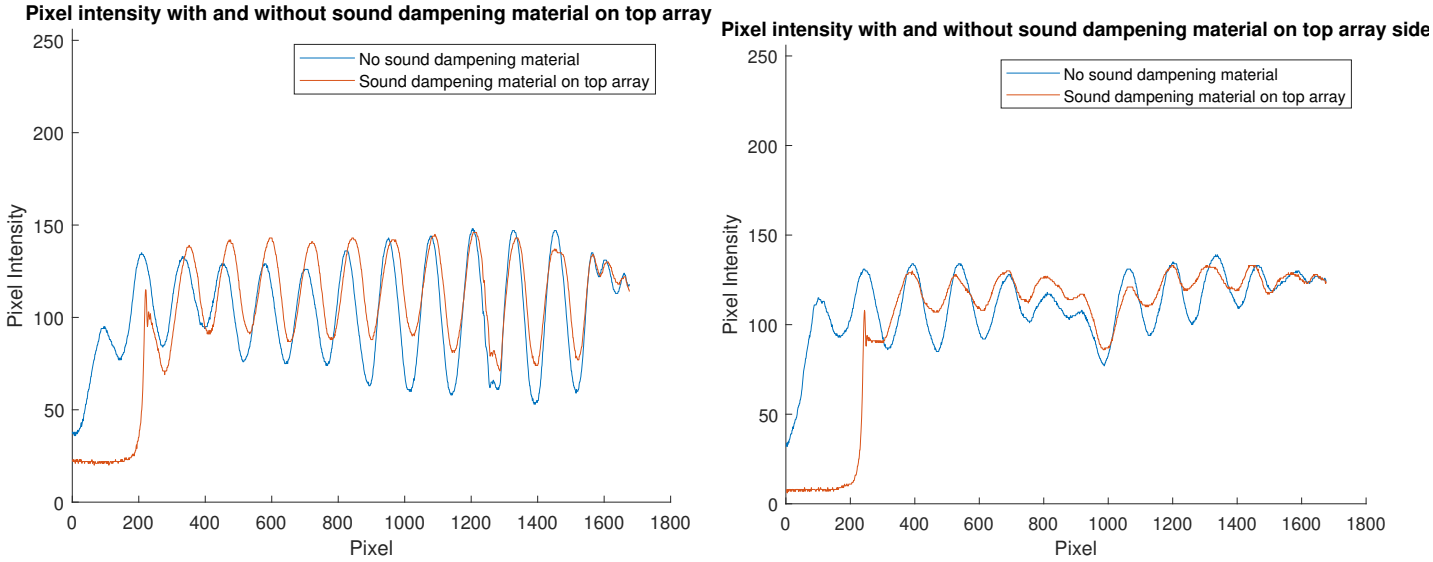

(a) Line cut above sound source (red line) **(b)** Line cut above in checkerboard pattern (blue line)

Figure 4-30: Pixel intensity comparison with regards to reflections

4-3-3 Discussion

Influence of air flow on the particle has been observed. Looking at the schlieren image, temperature and pressure do not affect the refraction angle similarly. More research is needed to fully assess the influence of air flow on the particle. Regarding the influence of reflections: although sound dampening material decreases the reflections, it does not fully remove them. There are also other surfaces than the top array, the acoustic waves can reflect from.

Chapter 5

Quantification

This chapter looks at quantifying the schlieren images. In this MSc thesis, the attempts at quantifying the pressure gradient have not been successful, yet the attempts that are made are placed here and in the appendices.

5-1 Quantifying the pressure gradient

The quantification of experimental schlieren images can be explained by finding the proper correlation between the pixel intensity and the pressure gradient. Under the assumption of a constant pressure gradient along the optical axis, the pressure gradient can be integrated to obtain the pressure field. Semi-quantitative judgments can still be made from schlieren images without. Under the assumption that the field can be assumed as constant over the optical axis, the pixel intensities can be compared with each other. If the same measurement setup parameters are used, and the assumption is made for ambient light, pixel intensities across images can be compared as well. Indicating a higher pixel intensity to a higher pressure gradient, and vice versa.

To correlate the pixel intensity to an exact pressure gradient one can use multiple methods. If one assumes a linear correlation between the intensity on the schlieren image and the pressure gradient, intensities can be extrapolated when two different points of pressure gradient and intensity are known. This can be done using a microphone, but also the eigenfrequency method gives an indication of the pressure at a location.

5-1-1 Microphone

Experiments with a lone transducer, outside of the acoustic levitator, have been conducted, but the contrast generated by the pressure field was not satisfactory, thus the example is moved to the appendices, in section A-2. The contrast was low because the amplitude of the signal was 10 volt peak-to-peak. This was the maximum signal that could be put on a lone transducer with the available equipment.

5-1-2 Thin lens method

Experiments have been done placing a variety of thin lenses with long focal lengths in the optical path alongside the ultrasound field. A plano convex lens of with a focal distance of 10m and 5m have been used and a double convex lens with a focal distance of 1.5m has also been used. The intensities observed on the schlieren image at the location of the lens seemed dependent on focus, which will be further explained in section 5-2. The experimental result of using the thin lens method to quantify the pressure gradient is not satisfactory for any of the lenses and one example of this is placed in the appendices in section A-5.

5-1-3 Eigenfrequency of levitated particle to determine strap stiffness

The movement of a levitated particle inside a node is tracked. Using the camera from the schlieren setup, but capturing a video at 240 frames per second the particle movement is recorded. Front lightning is switched on and the LED is turned off to create contrast between the particle and the background. The movements are tracked in Matlab and converted into the frequency domain to analyze the particle movement. The frequency spectrum of both x and z direction are plotted in Figure 5-1.

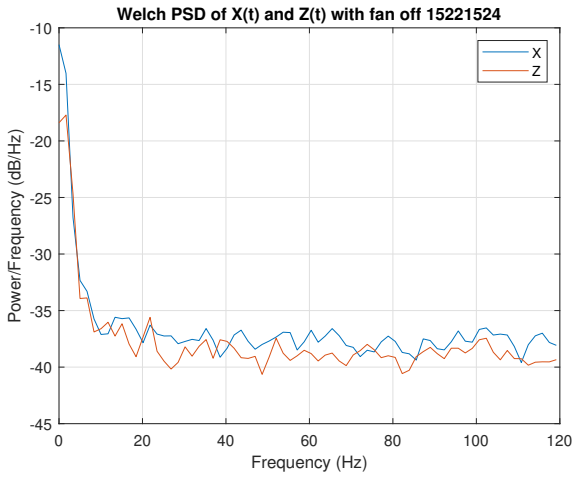

(a) Welch PSD of movement in x and z, fan off

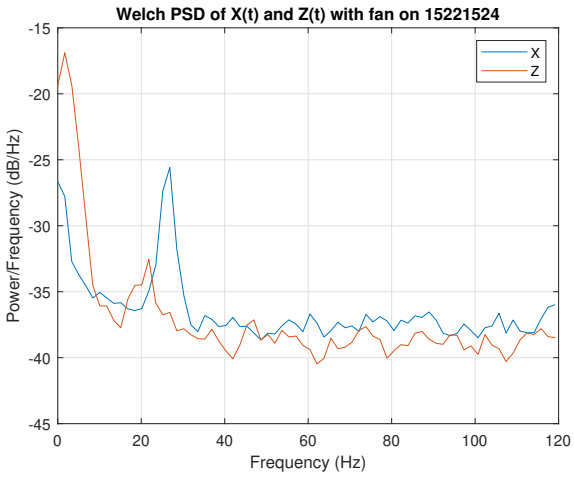

(b) Welch PSD of movement in x and z, fan on

Figure 5-1: Analysis of fan airflow on particle movement in frequency domain

Looking at the eigenfrequency in z direction one can use Equation 5-1 to calculate the local pressure p_a [102]. In which ω, c_0, ρ_0, ρ_p and f are the eigenfrequency, average speed of sound in the medium, density of the medium, density of the levitated particle and the sound frequency respectively. The density of the levitated particle (polystyrene) is 1005 $\frac{kg}{m^3}$. With a eigenfrequency of 21Hz, the pressure amplitude is calculated to be 1,91kPa.

$$\omega = \frac{f p_a}{2c_0^2}\sqrt{\frac{5}{\rho_p \rho_0}} \tag{5-1}$$

Numerical integration of a schlieren image is needed to get the pressure field, in order to 'fill in' the pressure from the eigenfrequency. This has been attempted but without good results.

5-1-4 Discussion

The microphone can be used to get a measure for the pressure field. It does require the integration of the schlieren image or the differentiation of the microphone data. The used microphone did not fit into the acoustic levitator perpendicular to any of the arrays to get a proper reading. The eigenfrequency method requires the schlieren image to be integrated to obtain the pressure field. The integration has been attempted without yielding good results. The eigenfrequency in z direction is expected to be higher than the eigenfrequency in x direction. This was not the case. The eigenfrequency could only be detected with the fan on. The influence of the fan on the eigenfrequency and particle movement needs to be studied. The setup of the camera and the ability to track a particle are not ideal. The particle itself, and its reflection in the mirror can both be seen, making it more difficult to sharply track the movement. The movements of the particle without the fan turned on are too small for the camera to properly track.

5-2 Observation of important parameter for quantifying pressure gradient

5-2-1 Observation

While using the schlieren setup and adjusting the camera lens to focus on the correct xz-plane to take schlieren images it was difficult to exactly determine the right plane. When a levitated particle was present it became easier since the object could be put into focus. To investigate the influence of camera focus distance on the schlieren image an investigation is done. The lens is replaced by a known set of lenses before the bare image sensor. This is done to be able to fully model the optical elements in the light path, since the exact details of the lenses in the lens system of the camera are unknown. This change with names for the lenses and distances are presented in Figure 5-2.

A convex lens f_2 with focal distance 100mm and a concave lens f_3 with a focal length of 50mm are replacing the camera lens. Distance d_1 is set at 50mm, while a stepper motor controlled distance d_2 on a linear guide and rail from 10 to 150mm. The lenses are chosen such that the image size on the sensor remains fairly constant, while the dept of focus changes. This is observed by placing different objects at different distances from the acoustic levitator and seeing these going in and out of focus while shifting d_2. Distance d_3 is kept constant and at 5mm. By shifting distance d_2 the focus of the image on the sensor can be changed. Connecting the linear guide to a spindle and stepper motor allows distance d_2 to be controlled and moved at a constant speed. The distance d_2 at which the plane of the levitator is in focus is about $d_2 = 30$mm. The focus is thus shifted from before to far beyond the levitator plane.

Observation 1: change in phase The transducer were given a signal such that a single levitation position was put in the origin while d_2 was shifted. The LED signal was synced at

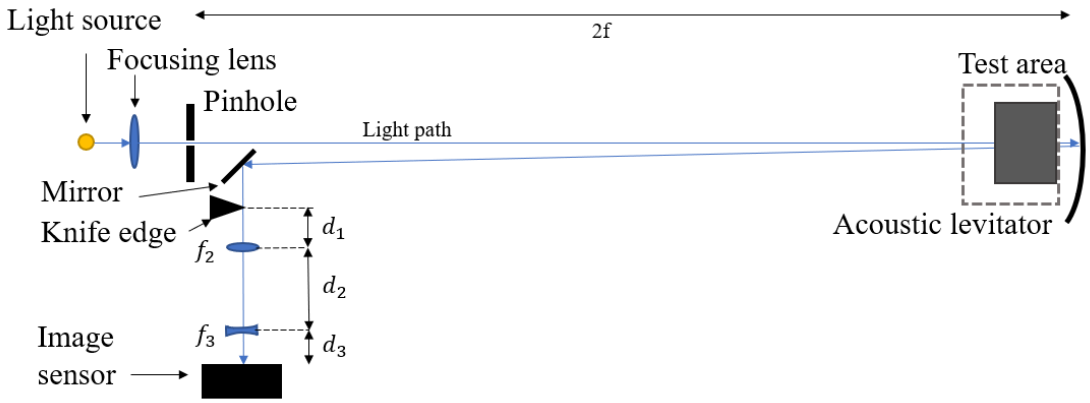

Figure 5-2: Change in schlieren setup optics

40kHz, while the knife edge is moved to such a position that it does not cut off any part of the light. This normally would not display any contrast in the schlieren image, so this would be considered a shadow graph. The distance d2 is moved linearly from about 10mm to 110mm. The pixel intensities along the vertical line, at the levitation point, are taken for the whole video. The intensities are plotted in Figure 5-3.

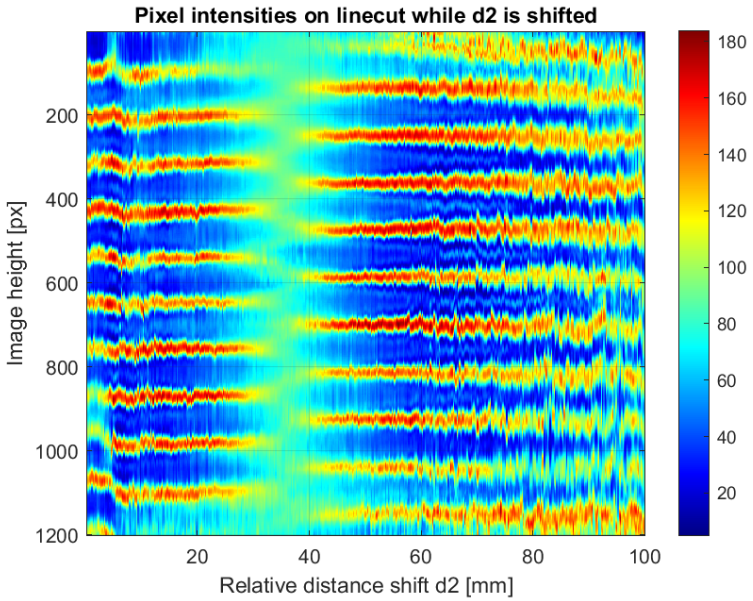

Figure 5-3: Change in phase with 40kHz signal

No clear contrast is visible when the focus is around the plane of the levitator itself. Before and after the distance d2, one can clearly see the pattern of a acoustic wave, with the wavelength of 8.5mm. The place at which these peaks appear on the image shift half a wavelength, while the acoustic signal remains unchanged.

Observation 2: Intensity changes With the knife edge still not cutting off any part of the light. The signal to the LED is changed such that the light is not synced with the transducers. The transducer phases are set, such that a levitation point is formed in the origin. As with observation 1, the pixel intensities along the vertical line, at the levitation point, are taken for the whole video. The intensities are plotted in Figure 5-4.

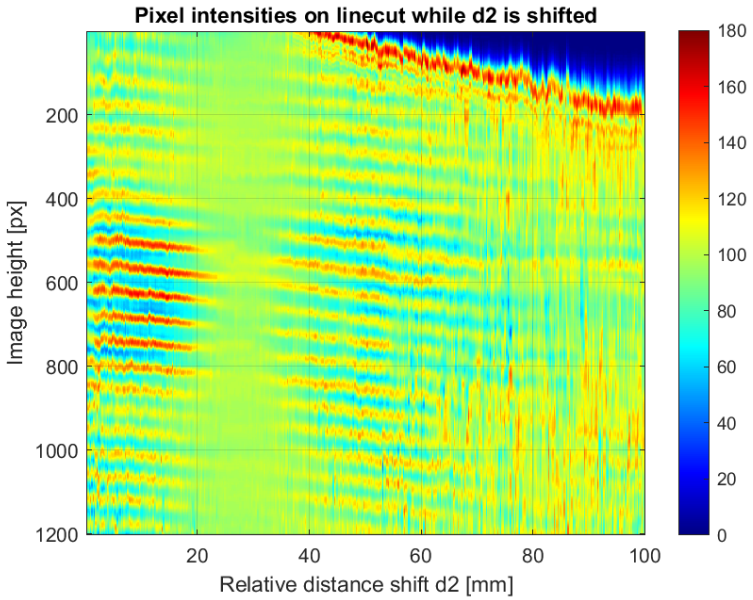

Figure 5-4: Change in phase with 40kHz signal

The pattern of an acoustic wave appears before and after the distance of $d_2 = 30$mm. The strongest pressure gradient are expected nearest to the levitation point. The strongest intensities are thus also expected near the origin, around pixel 600. These intensities also fade last, and appear first while the distance d_2 is increased. The intensities of the standing wave pressure gradients close to the origin, also have their peak values at a different location compared to an intensity lower down. For a better explanation, 2 examples will be given. First, taking the horizontal line at about vertical pixel 500. The first peak is about at $d_2 = 15$mm, while the second peak is about at $d_2 = 40$mm. Secondly, looking at the horizontal line at about vertical pixel 1000. The first peak can be estimated to be around $d_2 = 13$mm, while the second peak can be estimated to be around $d_2 = 55$mm. The data is very noise thus it is difficult to get exact values. The dependency of intensity and distance shift d_2 is interesting.

5-2-2 Proposed model

Traditional schlieren Schlieren relates a refractive index gradient to an angle ϵ using Fermat's principle, given in Equation 1-38. This angle is the used to determine the intensity and contrast on the image sensor or screen using parameters from the schlieren setup, as shown in Equation 1-45. This theory has been proven multiple times but can be extended in the use of ultrasound waves. The acoustic wave can act as a index gradient lens focusing the light rays onto a certain spot. This focus point will differ slightly from the focus spot initiated by the governing optics in the system since the refracting angle ϵ is very small.

Proposed model that might explain observations Proposing a new model to explain the observations made in section 5-2 is built upon the last paragraph. This model has not been verified. Since there is a repeating pattern of refractive index gradients, caused by the shape of the acoustic wave, the waves can be seen as a collection of small thin lenses, each having their own shifted focal point. This shifted focal point is dependent on the strength of the local refractive index gradient. By shifting the focus dept of the camera, it should allow the image sensor to capture the exact focal point of these index gradient lenses. Light intensity is highest when the focal point is exactly focused upon the image sensor. With exact knowledge of the optical elements in the setup, and the known location of the focus dept, an intensity peak can be connected to a specific focus dept. Using matrix optics, it has been shown that the intensity of the light on the image sensor is dependent on the distance d2 and on the strength of the pressure gradient. The used model has been briefly explained in section A-6.

5-2-3 Discussion

The schlieren setup has been converted slightly to show the observations seen in Figure 5-3 and Figure 5-4, yet is has not been designed for this from the start. There is misalignment between the axis along which d_2 is moved and the optical axis. This causes the whole image to shift downward on the image sensor. The lenses have been set up in such a way to have the image on the image sensor remain a constant size. This has not fully been achieved, which makes it difficult to compare intensities from different distances. The starting distance d_2 is difficult to determine exactly, but the movement actuated by the stepper motor is known. The distance shift d_2 is therefor only known in relatively. At the start of the movement, the camera had to be turned on manually, thus there is more instability in the first few seconds, and thus mm of the plots. Using a signal for the LED that is not synced with the transducers and has a completely different frequency is something that is not been investigated in this thesis. Non-linearity in the image sensor could cause the super positions of the intensities to purely show the standing waves. This needs to be studied more. The data is very noisy, since the setup is not optimized for further research into these observations. Therefor it is difficult to identify a trend from noise. Although the matrix optics model shows a relation between the distance shift and the pressure gradient, further research is needed.

5-2-4 Relevant literature

Literature using the schlieren method often do not specify the focus dept of the camera equipment or point out that the focus plane of the camera should be at the test area [10]. Focus and out-of-focus effects could reveal extra information about the subject in the test area [103]. Nobuki presents a similar method where the position of the virtual screen changes the visualisation of the ultrasound pulses in water [52]. The shift distance of the virtual screen however, is not related to the peak intensity to determine the refractive index gradient. The phase contrast method for measuring ultrasonic field presented by Erwin K. Reichiel and Bernhard G. Zagar also observe the same, but in their application it has to do more with diffraction patterns [104].

Chapter 6

Conclusions

6-1 Main findings

1. The influence of schlieren setup parameters
    - A duty cycle of 20% for the light source yields the highest contrast, in the range from 20% tot 60%.
    - The horizontal knife edge gives the more contrast than the vertical knife edge, in the visualisation of pressure gradients generated by the double phased array
    - Light source phase delay allows adjustment to visualise different parts of the complex pressure gradient field
    - Light source frequency allows adjustment to visualise an intensity pattern at 40kHz and at 80kHz. The intensity pattern observed at double the frequency has a lower intensity than the pattern visualised at 40kHz.
2. The designed and constructed schlieren setup allows for the validation of the pressure gradient field
3. Single and double trap locations can be visualised through the variation of the light source phase delay
4. The phase delay between two acoustic traps can be validated
5. Under the assumption of a 2D pressure gradient field
    - Schlieren allows for real time feedback and visualisation of the pressure gradient in one direction
    - Schlieren is a useful research tool visualising the acoustic trap type
    - Schlieren is a useful research tool visualising the acoustic trap positions

6-2 Conclusions

Looking back at the research questions at the start of this thesis many insights were gained. The main research question as presented in the introduction is: "To what extent can improvements be made to acoustic levitation using the visualisation of the pressure gradient?". This question is divided into multiple questions, which will be answered here, after which the main research question is answered.

What is the most suitable pressure gradient visualisation technique? This question has been answered in two ways. First, studying different measurement techniques in literature. By assessing the suitability of each technique, schlieren was chosen as the most suitable when looking at the design requirements. The design requirements subdivided in subcategories difficulty, time per measurement and measurement sensitivity. Second, once the schlieren setup has been constructed, the design requirement have been validated. The difficulty is mainly defined to enable the experimental setup to be constructed within the span of a MSc. thesis. The working schlieren setup has proved that the setup is not too difficult. The setup has a time per measurement of 20 seconds, with direct feedback on a monitor and further analysis in post processing within minutes. The measurement sensitivity is sufficient as a pressure gradient produced by a single transducer can be measured.

To what extent do visualisation technique parameters influence the visualisation of the acoustic field? Different parameters in the schlieren system have been investigated. Using a knife-edge cut-off, both the horizontal and vertical cut off have been investigated. The horizontal knife edge yields the most the most contrast in the results. This is expected as the pressure gradient with respect to the vertical axis is the highest. The duty cycle of the square wave light signal was investigated from 20% to 60%. The lowest duty cycle of 20% allows for the best visualisation. The light source phase delay can be adjusted to view the travelling and standing wave at a different phase. The light source frequency is studied at once and twice the acoustic frequency. The light source frequency at once the acoustic frequency gives a higher contrast while the double light source frequency visualises the acoustic wave at two phases in time.

What factors that influence acoustic levitation can be visualised? Factors that influence the acoustic levitation are air flow, the acoustic field and its reflections. The acoustic field is the most important factor, of which the pressure gradient can successfully be visualised, under the assumption that it is constant over the optical axis. Specific features of the acoustic field are successfully visualised as well, namely acoustic trap locations and acoustic trap types. By adjusting the phase delay of the light source, the relative phase difference between two acoustic traps can be validated against modelled schlieren images. Regarding more complicated acoustic fields; it has been shown that as the complexity increases, that the assumption of the constant acoustic field over the optical axis does not hold, as expected. The visualisation of the acoustic field was needed not only for the verification of the acoustic field, but also for exploring parasitic effects that that influence levitated particle movement in the low frequency domain. Parasitic effects that influence acoustic levitation are also visualised. Reflections of the acoustic field can be visualised and also affect the acoustic field and thus

acoustic levitation. Airflow from heat has been visualised as well using the schlieren system. Analysing the levitator particle movement using the camera from the schlieren setup, it has been shown that the air movement around a particle does influence particle movement.

To what extent can the visualisations be quantified? The intensities on a schlieren image are dependent on the pressure gradient. The intensities can be categorized on an ordinal level. Quantifying the intensities with a known pressure gradient has not been achieved. Two calibrated schlieren methods have been attempted, but did not yield satisfactory results. Using a microphone to measure the pressure field, of which the measurement can be differentiated to the pressure gradient to calibrate the schlieren image. The schlieren setup was not sensitive enough to visualise the pressure gradient driven by a single transducer at 10 Vpp. Thus the baseline measurement could not be made. The second calibrated schlieren method is using a thin lens, of which the refraction angle is a function of the radius of the lens. Thin lenses with focal distances of 10m, 5m and 1.5m did not yield enough contrast to correlate the radius to a refraction angle. According to theory this calibrated schlieren method should work thus further research is needed. An observation regarding a correlation between the camera focus distance, measured light intensity and pressure gradient has been made as well. Numerical integration of the schlieren image to obtain the pressure field has also been attempted but did not yield satisfactory results. Detailed knowledge on the image sensor's ability to capture light is needed as well for quantification.

Main research question: To what extent can improvements be made to acoustic levitation using the visualisation of the pressure gradient? The schlieren setup is a great research tool to have. It allows for easy verification of the acoustic field. Especially identifying and confirming trap types and locations. This has already proven helpful to acoustic levitation research and will continue doing so. Now the answer to the main research questions: 'To what extent can improvements be made to acoustic levitation using the visualisation of the pressure gradient?'. First, the visualisations have shown that reflections of the acoustic field, affect the acoustic field and thus acoustic levitation. Reflections are currently not taken into considerations but it is expected that accounting for them will improve understanding of the generated acoustic field. Second, the schlieren setup has visualised thermal air flow and it has been assessed that this does effect particle movement. And at last, the ability to visualise the pressure gradient to visualise trap types and locations has proved helpful. Even without the assumption of a constant acoustic field, the experimental schlieren image can be seen as a fingerprint to validate the against the modelled schlieren image. Visualising the trap type and using the light source phase delay to identify trap locations and pressure gradient phase, are significant improvements over the state of the art presented in theory with regards to airborne ultrasound generated by phased arrays, as this has not yet achieved.

Chapter 7

Outlook

7-1 Visualising pressure gradient

7-1-1 Schlieren equipment improvements

Improvement to the schlieren equipment that would be feasible within one month.

- The use of different source and cut-off filters
  - The use of a square pin hole would be a better pair in combination with a straight knife edge. For quantitative analysis, the refractive index is dependent on the dimensions of the rectangular source slit. Though widely used for visualisation, the use of a pinhole for quantitative analysis needs to be investigated.
  - Making a custom gradient cut off filter for a wider measurement range.
  - Making a custom color filter would allow for viewing both the refractive index gradient in z and x direction simultaneously
- Stability improvements to the whole setup
  - Placing the setup on an optical table to minimize vibrations
  - Controlling the ambient air flows around the setup better
  - Eliminate ambient light around the setup as this is a factor that is now uncontrolled. This would allow comparison between experiments on different days as the ambient light level is controlled.
  - Eliminating the ambient airflow caused by air conditioning, room ventilation and people movement will allow the better identification of sources of flow in the test area. Since room ventilation is difficult to control an air tight and light blocking case is advised to build around the setup.

- Noise reduction. The static noise can be reduced by looking at the optics or the camera. At the time of this report, not all desired optical components were in stock thus suitable alternatives were chosen. One could check if a higher quality mirror with greater or equal focal distance is available to lower standard deviation. A higher bit dept for the camera would also improve the resolution, though this seems unnecessary if the quality of the optics remains the same. Further research is needed to pinpoint the main noise source as the camera or the optics.
- The use of a scientific camera would help quantify the light intensities on each pixel. With the current image sensor, it is unknown how exactly light is converted into a digital image. This includes the linearity of intensity with the electrically produced signal and the post processing that occurs on the camera.
- Visualisation while using the double light frequency needs further research. Possible causes are the non linearity of the image sensor, or phenomena like acoustic streaming.
- Tomography is a logical next step which could be explored if a full visualisation of the 3D field is needed.

7-1-2 Post-processing improvements

For post-processing in this thesis, the Matlab function 'im2gray' has been mainly used to convert the schlieren RGB images into a grayscale image. Looking purely at the green channel gives different results. Without knowing the exact specifications of the image sensor and the light source it is difficult to extract the correct light intensity information out of the raw image. More knowledge is needed on how the image sensor converts light into a digital signal and how this digital signal is processed before it is presented to the user.

7-2 Quantifying pressure gradient

7-2-1 Schlieren

While schlieren allows for visualisation of the pressure gradient, getting a ratio measurement from schlieren data is difficult and has not been achieved in this thesis. The main reason for this is that it is unknown how the image sensor captures and converts light. A scientific calibrated camera would be beneficial in quantifying the pressure gradient. The light emitted from the light source would also need to be known. The use of color filters could allow for quantification of the pressure gradient, though it would also require excellent knowledge on the image sensor, optical elements and light source. The thin lens method, according to the presented theory, seems the easiest quantification method thus different lenses can be acquired to further investigate. The use of the microphone can still be investigated, when the top side of the acoustic levitator is removed. This allows the placement of the microphone at various distances and also gets rid of the main expected reflector of the ultrasound: the top array. The acoustic field can still be studied this way, including reflections against known surfaces. Quantifying a 3D acoustic field, which cannot be assumed constant over the optical axis, using schlieren will require extra work. While tomography is an option, exploring other methods for quantifying the pressure can be investigated as well.

7-2-2 Different methods

The observations of the importance of the focus dept of the camera is something to be further explored. Although its connections to shadowgraphy, the unique combination with the repeating pattern of ultrasound waves might yield interesting results and a new way to quantify the pressure gradient. Relating a peak in intensity to a certain focus dept instead of trying to relate the height of the intensity peak to a refraction angle can be beneficial. This has also not been covered by theory, with regards to ultrasound in air. Yet, this method would still be constrained by assuming a constant 2D field over the optical axis.

7-3 Visualising flow

Even though visualising flow was not the goal of this thesis, the schlieren setup allows for the visualisation of flow. But the schlieren setup has not been optimized for this. It would be interesting to study the general flow within the phased array. It would also be interesting to study the flow between levitation traps, though further research is needed to see if this is possible with the current schlieren setup. Using the phased arrays this is difficult since a 3D acoustic field is present. A single axis acoustic levitator might be easier to observe and can be approximated better as a 2D field. To further investigate the influence of the transducer and amplifier heating on particle stability, one should investigate the particle movement and the flow generated by a temperature controlled phased array at different setup temperatures.

7-4 Further thoughts

Acoustic levitation is a promising research area with many unexplored options. Risks regarding working with high intensity ultrasound needs to be properly understood and suitable preventive measurements need to be put in place. This applies to both a research environment and manufacturing a commercial machine.

Appendix A

Appendix

A-1 Derivation of general wave equation for the pressure

This whole derivation is put into the appendices this report for ease of use but is taken directly from Kundu et al [12].

The conservation of mass given in Equation A-1. With p, ρ, u and q the pressure, density, velocity and unsteady volume source distribution, respectively.

$$\frac{1}{\rho}\frac{D\rho}{Dt} + \frac{\delta u_i}{\delta x_i} = q(x_i, t) \tag{A-1}$$

The conservation of momentum given in Equation A-2. With g_j, τ_{ij} and f, the gravity, viscous stress tensor and unsteady body-force distribution, respectively.

$$\frac{Du_j}{Dt} + \frac{1}{\rho}\frac{\delta p}{\delta x_j} = g_j + \frac{1}{\rho}\frac{\tau_{ij}}{\delta x_i} + f_j(x_i, t) \tag{A-2}$$

The equation for pressure in accordance with the isentropic assumption.

$$\frac{Dp}{Dt} = (\frac{\delta p}{\delta \rho})_s + (\frac{\delta p}{\delta s})_\rho \frac{Ds}{Dt} = c^2 \frac{D\rho}{Dt} \tag{A-3}$$

One can use Equation A-3 and Equation A-1 to find Equation A-4. Where the summed over index has been switched from i to j.

$$\frac{D}{Dt}(\frac{1}{\rho c^2}\frac{Dp}{Dt} = \frac{Dq}{Dt}) - \frac{D}{Dt}\frac{\delta u_j}{\delta x_j} \tag{A-4}$$

Apply $-\frac{\delta}{\delta x_j}$ to Equation A-4.

$$\frac{\delta}{\delta x_j}\frac{Du_j}{Dt} - \frac{\delta}{\delta x_j}(\frac{1}{\rho}\frac{Dp}{Dx_j}) = -\frac{\delta g_j}{\delta x_j} - \frac{\delta}{\delta x_j}(\frac{1}{\rho}\frac{\delta \tau_{ij}}{\delta x_i}) - \frac{\delta f_j}{\delta x_j}) \tag{A-5}$$

Drop the viscous stress term and note that $\frac{\delta g_j}{\delta x_j} = 0$ if the assumption is made that the body force is uniform.

$$\frac{\delta}{\delta x_j}(\frac{1}{\rho}\frac{\delta p}{\delta x_j}) = -\frac{\delta f_i}{\delta x_j} + \frac{\delta}{\delta x_j}\frac{Du_j}{Dt} \tag{A-6}$$

Combine Equation A-5 and Equation A-6 to get to final answer with the necessary simplifications.

A-2 Estimating minimum detectable refraction angle

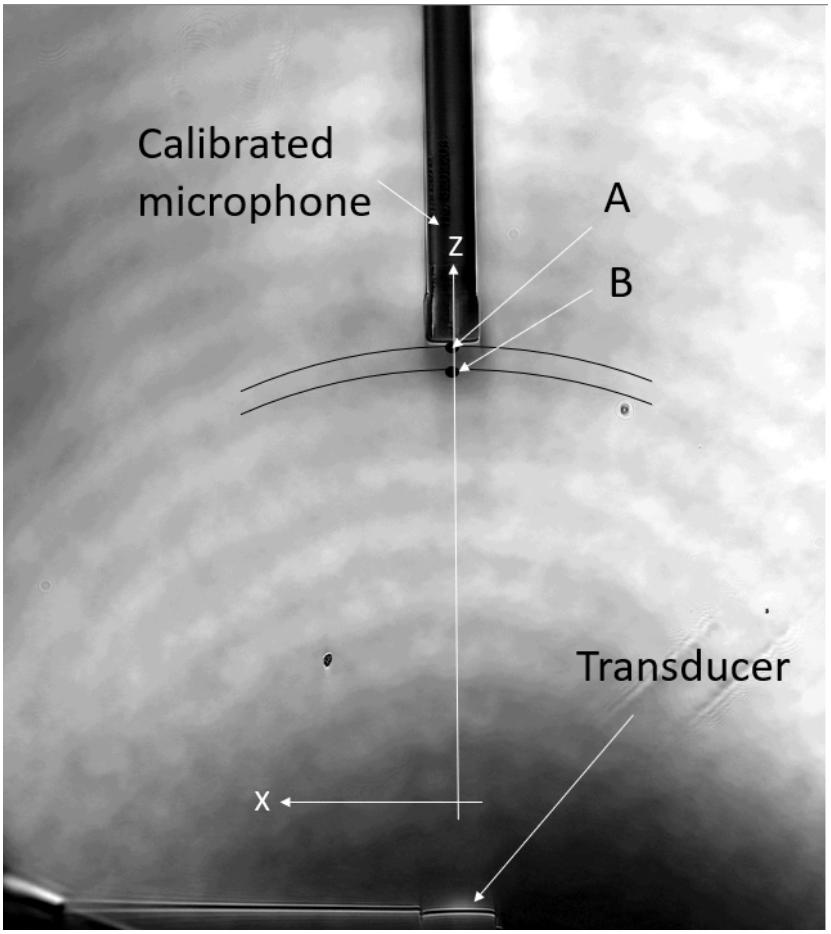

Figure A-1: Schlieren image of single transducer and microphone, with post processing

A single transducer is emitting an acoustic signal and is driven by a 40kHz signal at 10Vpp. A calibrated microphone (Bruer & Kjaer Type 4939-A-011) is at a known distance directly

	Single transducer	Transducer line
wavelength	8.57mm	8.57mm
L	10.5mm	8*10.5
Signal [Pixel Intensity]	1	100
Measured pressure point A	40mVpp = 9.80 Pa	-
Calculated maximum pressure	-	300 Pa
Estimated $\epsilon_{z,max}$	1.96e-6 rad	4.79e-4 rad
Estimated $\frac{d\epsilon}{dI}$	1.96e-6	4.79e-5

Table A-1: Estimated parameters for minimum detectable pressure gradient for single transducer and line

above the transducer. The pressure in point A is measured across time t. This is a sinusoidal shape as expected. This reveals something about the pressure in point A. Point B is exactly half a wavelength from A along the z axis. If, at a time t_0, the pressure in A is the maximum pressure. Assuming no attenuation, this will tell that the pressure in B is the minimum pressure. The pressure, close to the transducer can be estimated using Equation A-7, in which P_{max} is the maximum measured pressure in the microphone signal.

$$p(z, t = t0) = P_{max} sin(\frac{2\pi}{\lambda} z) \tag{A-7}$$

The derivative of the pressure with respect to the z dimensions can be calculated using Equation A-8.

$$\frac{dp}{dz}(z, t = t0) = P_{max} \frac{2\pi}{\lambda} \cos(\frac{2\pi}{\lambda} z) \tag{A-8}$$

The pressure gradient is related to the refraction angle with Equation 1-39. In which the values are filled in from Table A-1. Using a 20% duty cycle, the LED is on for 20% while it is off for the other 80% of the signal. With a duration of the signal of exactly the acoustic frequency, an estimate for the measured epsilon is given in Equation A-9. In which dutycycle is specified in %.

$$\epsilon_{z,meas} = \frac{KL}{n_0 RT} \frac{2\pi}{\lambda \cdot \text{dutycycle}} \int_{-\frac{\text{dutycycle}}{2}\pi}^{+\frac{\text{dutycycle}}{2}\pi} P_{max} \frac{2\pi}{\lambda} \cos(\frac{2\pi}{\lambda} z)\, dz \tag{A-9}$$

$$\epsilon_{z,meas,max} \approx \frac{KL}{n_0 RT} \frac{2\pi}{\lambda} 0.95 P_{max} \tag{A-10}$$

Of the pressure gradient that is displayed, the maximum value of $\frac{dp}{dz}$ causes the maximum value for ϵ_z. The signal is estimated using the maximum intensity value minus the minimum intensity value.

$$\frac{d\epsilon}{dI} = \frac{2\epsilon_{max,meas}}{I_{signal}} \tag{A-11}$$

A-3 Additional visualisations of acoustic field

A-3-1 Parallel lines, bottom only

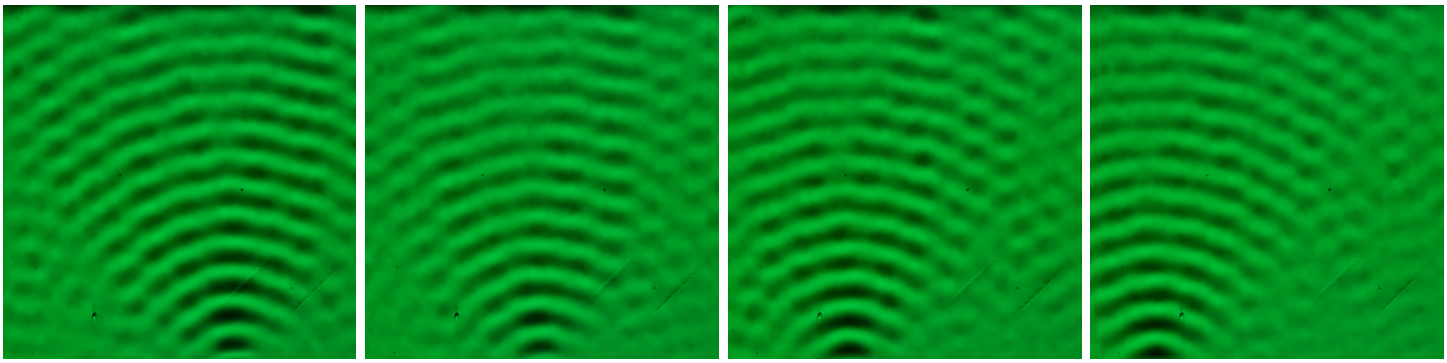

(a) Parallel transducer line 3 **(b)** Parallel transducer line 4 **(c)** Parallel transducer line 5 **(d)** Parallel transducer line 6

Figure A-2: Transducer lines on bottom array parallel to y axis visualised

A-3-2 Perpendicular lines, bottom only

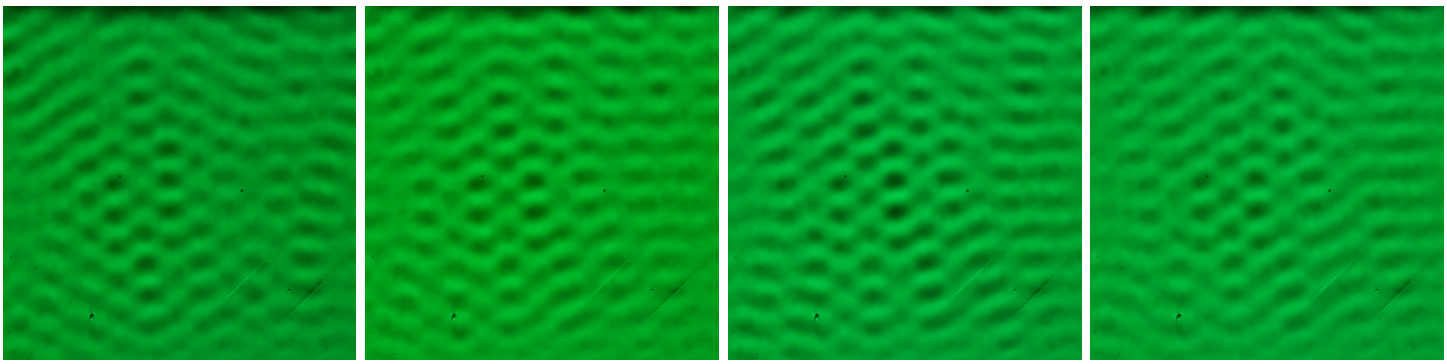

(a) Parallel transducer line 1 **(b)** Parallel transducer line 2 **(c)** Parallel transducer line 3 **(d)** Parallel transducer line 4

Figure A-3: Transducer lines on bottom array perpendicular to y axis visualised

A-3-3 Transducer line parallel to optical axis, top and bottom

A-3-4 Transducer line perpendicular to optical axis, top and bottom

A-4 Additional frequency spectrum of levitated particle movement with fan off and on

These plots are the results of measurements that are done to analyze the influence the fan and the thermal air flow on the particle movement. Videos are taken for 60 seconds at 29.97

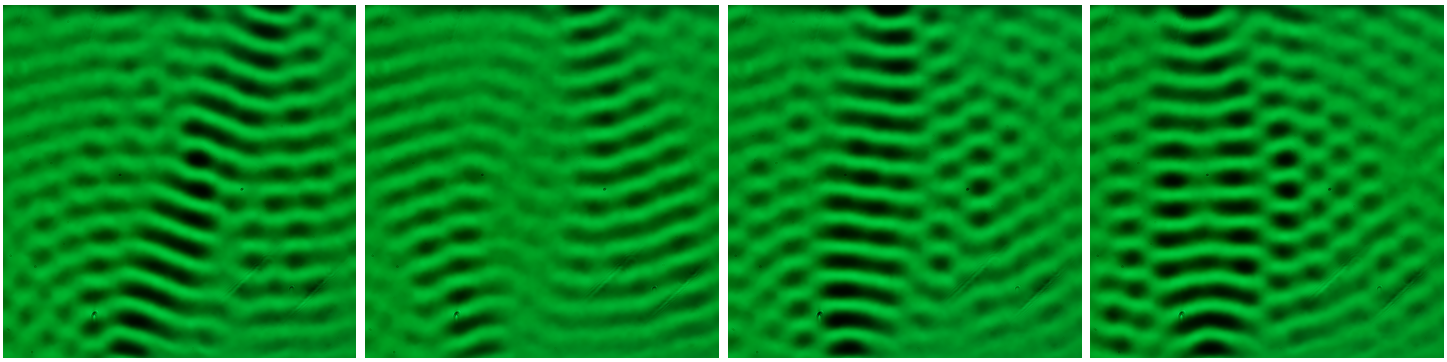

(a) Double parallel transducer line 4 and 2

(b) Double parallel transducer line 4 and 3

(c) Double parallel transducer line 4 and 4

(d) Double parallel transducer line 4 and 5

Figure A-4: Transducer lines, top and bottom array, parallel to y axis visualised

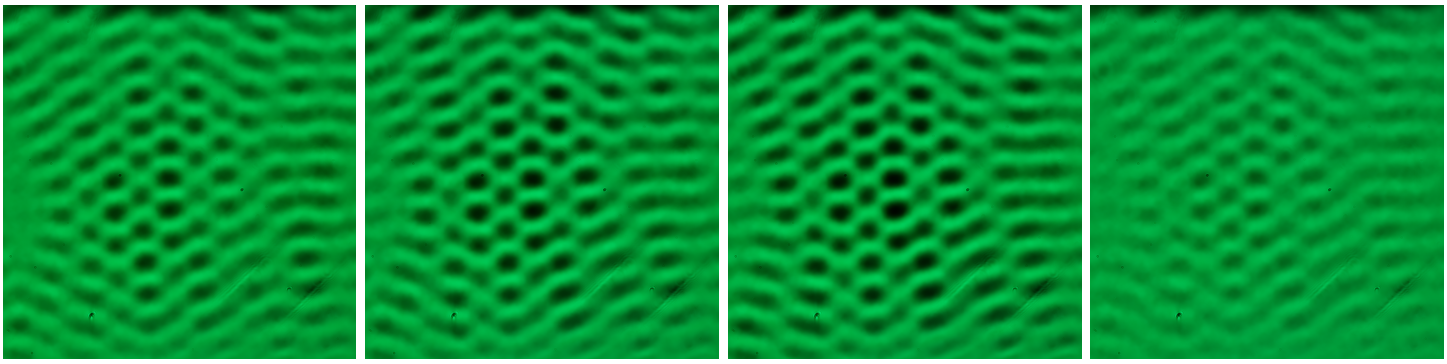

(a) Double perpendicular transducer line 3

(b) Double perpendicular transducer line 4

(c) Double perpendicular transducer line 5

(d) Double perpendicular transducer line 6

Figure A-5: Transducer lines, top and bottom array, parallel to x axis visualised

fps, thus only a maximum frequency of 15Hz can be observed. The particle has a diameter of 1.48mm and consists out of cellulose. The particle is levitated in an acoustic trap located in the origin. The PSD of the x direction is presented in Figure A-6a while the z direction is shown in Figure A-6b.

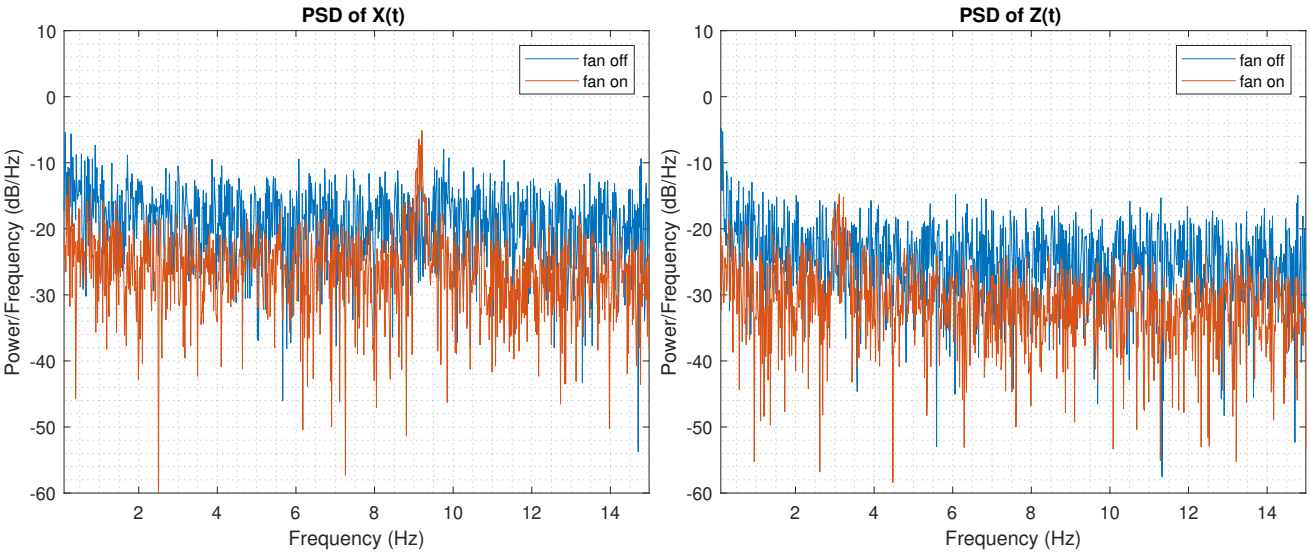

(a) PSD of movement in x, fan on vs off

(b) PSD of movement in z, fan on vs off

Figure A-6: Analysis of fan airflow on particle movement in frequency domain

A-5 Thin lens method schlieren images

A schlieren image of a lens is taken and shown in Figure A-7a. The lens with a focal length of 5m is placed against the acoustic levitator. This is not a video of which the mean intensities are taken but a single photograph. A shutter time of 60 and ISO of 2000 are used. A vertical knife edge is used as with it blocking off the negative direction of the x axis in the xz-plane. the acoustics are not turned on, but ambient airflow can be identified in the schlieren image.

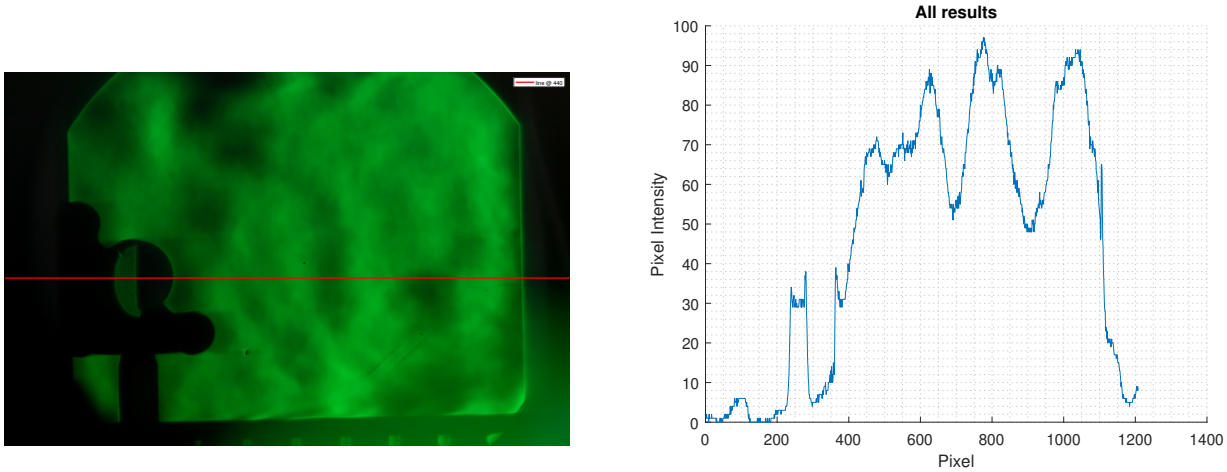

(a) Thin lens with vertical knife edge. No sound

(b) Pixel intensities along red line

Figure A-7: Thin lens with vertical knife edge without sound and pixel intensities along red line

The theory expects a intensity distribution across the lens that correlates with the horizontal

distance to the center line of the lens. This is not observed in Figure A-7b.

A-6 Focus dept observations

Using ray optics and matrix optics the following model has been made. The pressure gradients are modelled as weak lenses with varying focal dept. Please note that the distances and the coordinate system in this model are not the same as is used in the rest of this thesis.

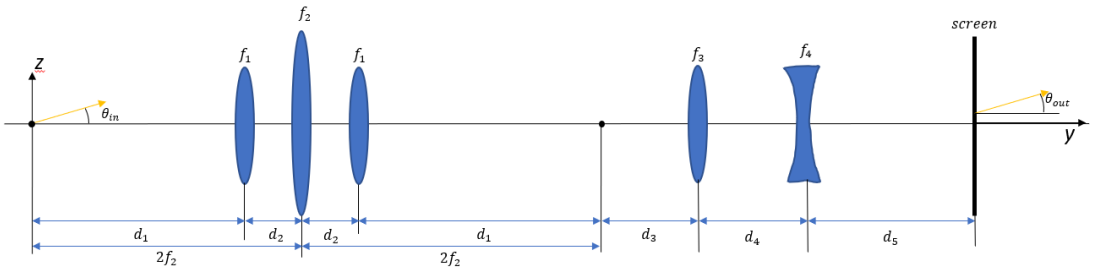

$f_1 = varied\ from\ 0.05m\ to\ 50m$
$f_2 = 2.032m$
$f_3 = 0.1m$
$f_4 = -0.05m$

$d_1 = 0.95 * 2 * f_2$
$d_2 = 0.05 * 2 * f_2$
$d_3 = f_3$
$d_4 = 0.10m$ *(or varied from 0.02 tot 0.15m)*
$d_5 = 0.05m$

Figure A-8: Matrix optics model

Looking at Figure A-9 one should look at the point where each line crosses the zero line. This would be the point where the highest peak of intensity is expected. Two light rays with initial height z_{in} and $-z_{in}$ and with angle θ_{in} and $-$
$theta_{in}$ come meet each other when height z_{out} equals zero. This is where the highest intensity is expected. The baseline gives focal point of the light rays, when the lenses f1 are not present. The introduction of thin lens f1 shows that the focal point is shifted dependent on the focal distance f1.

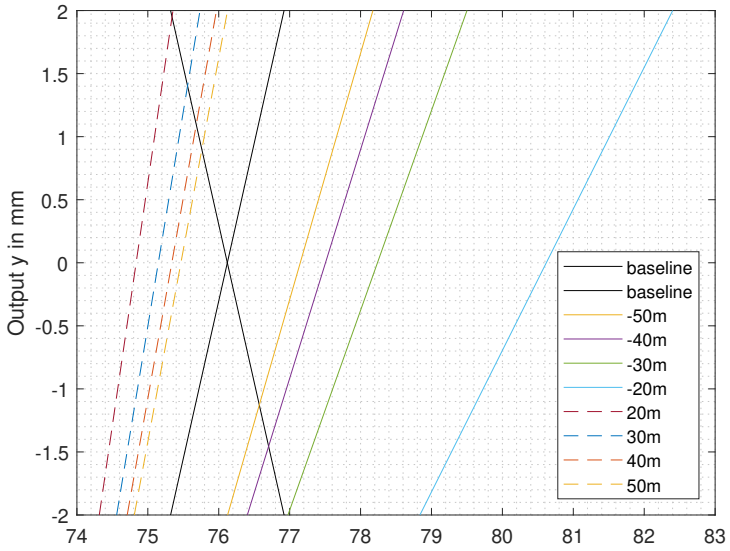

Figure A-9: Matrix optics model results

Bibliography

[1] A. M.A.B., R. T.S., O. F.T.A., and A. J.C., "Nonlinear characterization of a single-axis acoustic levitator," *Review of Scientific Instruments*, vol. 85, no. 4, 2014.

[2] K. Hasegawa, Y. Abe, A. Kaneko, Y. Yamamoto, and K. Aoki, "Visualization measurement of streaming flows associated with a single-acoustic levitator," *Microgravity Science and Technology : An International Journal for Microgravity and Space Exploration Related Research*, vol. 21, no. 1, pp. 9–14, 2009. 9.

[3] T. Omirou, A. Marzo, S. A. Seah, and S. Subramanian, *LeviPath Modular Acoustic Levitation for 3D Path Visualisations*, pp. 309–312. Proceedings of the 33rd Annual ACM Conference on Human Factors in Computing Systems, ACM, 2015.

[4] Smarter Every Day, "Acoustic levitation in ultra slow motion."

[5] . Settles, G. S. (Gary S.), *Schlieren and shadowgraph techniques : visualizing phenomena in transparent media*. Experimental fluid mechanics, Berlin ;: Springer, 2001.

[6] H. Richard and M. Raffel, "Principle and applications of the background oriented schlieren (bos) method," *Measurement Science and Technology*, vol. 12, pp. 1576–1585, Aug 2001.

[7] R. J. Goldstein, *Fluid mechanics measurements*. Washington, DC: Taylor & Francis, 2nd ed. ed., 1996.

[8] E. Olsson, N.-E. Molin, M. Sjodahl, L. Zipser, and H. Franke, "Scattered ultrasound fields measured by scanning laser vibrometry," in *SPIE Proceedings* (W. Osten, M. Kujawinska, and K. Creath, eds.), SPIE, May 2003.

[9] A. Pulkkinen, J. J. Leskinen, and A. Tiihonen, "Ultrasound field characterization using synthetic schlieren tomography," *The Journal of the Acoustical Society of America*, vol. 141, pp. 4600–4609, June 2017.

[10] M. J. Hargather and G. S. Settles, "A comparison of three quantitative schlieren techniques," *Optics and Lasers in Engineering*, vol. 50, no. 1, pp. 8–17, 2012. Advances in Flow Visualization.

[11] T. D. Rossing, *Introduction to Acoustics*, pp. 1–7. Springer Handbook of Acoustics, New York, NY : Springer New York : Springer, 2014.

[12] P. K. Kundu, I. M. Cohen, D. R. Dowling, and G. Tryggvason, *Fluid mechanics*. London: Academic Press, sixth edition. ed., 2016.

[13] S. W. Rienstra and A. Hirschberg, "An introduction to acoustics," 2001.

[14] S. L. . Garrett, "Understanding acoustics : an experimentalist's view of sound and vibration," 2020.

[15] M. V. Berry, *The diffraction of light by ultrasound*. London: Academic Press, [u.s. ed.]. ed., 1966.

[16] T. A. Pitts and J. F. Greenleaf, "Three-dimensional optical measurement of instantaneous pressure.," *The Journal of the Acoustical Society of America*, vol. 108, no. 6, pp. 2873–83, 2000. 2873.

[17] T. A. Pitts, A. Sagers, and J. F. Greenleaf, "Optical phase contrast measurement of ultrasonic fields.," *IEEE transactions on ultrasonics, ferroelectrics, and frequency control*, vol. 48, no. 6, pp. 1686–94, 2001. 1686.

[18] M. J. Crocker, "Encyclopedia of acoustics. volume 1," 1997.

[19] G. E. Elsinga, B. W. van Oudheusden, F. Scarano, and D. W. Watt, "Assessment and application of quantitative schlieren methods: Calibrated color schlieren and background oriented schlieren," *Exp. Fluids*, vol. 36, pp. 309–325, Feb. 2004.

[20] M. A. B. Andrade, N. Pérez, and J. C. Adamowski, "Experimental study of the oscillation of spheres in an acoustic levitator.," *The Journal of the Acoustical Society of America*, vol. 136, no. 4, pp. 1518–29, 2014. 1518.

[21] E. Leung, N. Jacobi, and T. Wang, "Acoustic radiation force on a rigid sphere in a resonance chamber," *The Journal of the Acoustical Society of America*, vol. 70, no. 6, pp. 1762–1767, 1981. 1762.

[22] M. W. Thompson and A. A. Atchley, "Simultaneous measurement of acoustic and streaming velocities in a standing wave using laser doppler anemometry," *The Journal of the Acoustical Society of America*, vol. 117, pp. 1828–1838, Apr. 2005.

[23] M. Wiklund, "Ultrasonic enrichment of microparticles in bioaffinity assays," 05 2023.

[24] M. A., D. B.W., and B. A., "Tinylev: A multi-emitter single-axis acoustic levitator," *Review of Scientific Instruments*, vol. 88, no. 8, 2017.

[25] T. Aikawa and N. Kudo, "Visualization of wall propagation and surface reflection effects on ultrasound fields generated inside a small container," *Japanese Journal of Applied Physics*, vol. 58, p. SGGE11, June 2019.

[26] L. V. King, "On the acoustic radiation pressure on spheres," *Proceedings of The Royal Society A: Mathematical, Physical and Engineering Sciences*, vol. 147, pp. 212–240, 1934.

[27] D. Zang, ed., *Acoustic Levitation: From Physics to Applications*. Singapore: Springer Singapore, 2022/08/30/10:46:31 2020.

[28] M. Settnes and H. Bruus, "Forces acting on a small particle in an acoustical field in a viscous fluid.," *Physical review. E, Statistical, nonlinear, and soft matter physics*, vol. 85, no. 1 Pt 2, p. 016327, 2012. 016327.

[29] H. Bruus, "Acoustofluidics 7: The acoustic radiation force on small particles.," *Lab on a chip*, vol. 12, no. 6, pp. 1014–21, 2012. 1014.

[30] T. Wang, C. Zhang, A. Aleksov, I. Salama, and A. Kar, "Two-dimensional refractive index modulation by phased array transducers in acousto-optic deflectors.," *Applied optics*, vol. 56, no. 3, pp. 688–694, 2017. 688.

[31] A. Lamprecht, T. Schwarz, J. Wang, and J. Dual, "Viscous torque on spherical micro particles in two orthogonal acoustic standing wave fields," *The Journal of the Acoustical Society of America*, vol. 138, pp. 23–32, July 2015.

[32] M. W. Kepa, T. Tomizaki, Y. Sato, D. Ozerov, H. Sekiguchi, N. Yasuda, K. Aoyama, P. Skopintsev, J. Standfuss, R. Cheng, M. Hennig, and S. Tsujino, "Acoustic levitation and rotation of thin films and their application for room temperature protein crystallography," *Scientific Reports*, vol. 12, Mar. 2022.

[33] A. Marzo, T. Corkett, and B. W. Drinkwater, "Ultraino: An open phased-array system for narrowband airborne ultrasound transmission," *IEEE Transactions on Ultrasonics, Ferroelectrics, and Frequency Control*, vol. 65, pp. 102–111, Jan. 2018.

[34] D. R. Sahoo, T. Nakamura, A. Marzo, T. Omirou, M. Asakawa, and S. Subramanian, *JOLED, A Mid-air Display based on Electrostatic Rotation of Levitated Janus Objects*, pp. 437–448. Proceedings of the 29th Annual Symposium on User Interface Software and Technology, ACM, 2016.

[35] R. Hirayama, G. Christopoulos, D. Martinez Plasencia, and S. Subramanian, "High-speed acoustic holography with arbitrary scattering objects," *Science Advances*, vol. 8, p. eabn7614, 2022/10/06 XXXX.

[36] J. Huang, J. A. Nissen, and E. Bodegom, "Diffraction of light by a focused ultrasonic wave," *Journal of Applied Physics*, vol. 71, no. 1, pp. 70–75, 1992. 70.

[37] R. Adler, "Interaction between light and sound," *IEEE Spectrum*, vol. 4, no. 5, 1967.

[38] P. K. Panigrahi and K. Muralidhar, "Schlieren and shadowgraph methods in heat and mass transfer," 2012.

[39] B. E. A. . Saleh and M. C. Teich, *Fundamentals of photonics*. Wiley series in pure and applied optics, New York: Wiley, 1991.

[40] C. Brownlee, V. Pegoraro, S. Shankar, P. McCormick, and C. Hansen, "Physically-based interactive schlieren flow visualization," in *2010 IEEE Pacific Visualization Symposium (PacificVis)*, pp. 145–152, 2010.

[41] C. V. Raman and N. S. Nagendra Nath, "The diffraction of light by sound waves of high frequency: Part ii," *Proceedings of the Indian Academy of Sciences - Section A*, vol. 2, no. 4, pp. 413–420, 1935. 413.

[42] L. Jia, B. Xue, S. Chen, H. Wu, X. Yang, J. Zhai, and Z. Zeng, "Characterization of pulsed ultrasound using optical detection in raman-nath regime.," *The Review of scientific instruments*, vol. 89, no. 8, p. 084906, 2018. 084906.

[43] C. V. Raman and N. S. Nagendra Nathe, "The diffraction of light by high frequency sound waves: Part i.," *Proceedings of the Indian Academy of Sciences - Section A*, vol. 2, pp. 406–412, Oct 1935.

[44] P. Kwiek, W. Molkenstruck, and R. Reibold, "Determination of the klein-cook parameter in ultrasound light diffraction," *Ultrasonics*, vol. 34, pp. 801–805, Dec 1996.

[45] R. Reibold and P. Kwiek, "On ultrasound light diffraction," *Ultrasonics*, vol. 31, no. 5, pp. 307–313, 1993. 307.

[46] A. Holm and H. W. Persson, "Optical diffraction tomography applied to airborne ultrasound," *Ultrasonics*, vol. 31, no. 4, pp. 259–265, 1993.

[47] P. Kwiek, W. Molkenstruck, and R. Reibold, "Optical mapping of ultrasonic fields in the intermediate range between weak and strong acousto-optical interaction," *Ultrasonics*, vol. 35, no. 7, pp. 499–507, 1997. 499.

[48] R. Reibold and P. Kwiek, "Uncertainty considerations of ultrasonic field mapping by light-diffraction tomography," *Ultrasonics*, vol. 35, no. 3, pp. 187–193, 1997.

[49] A. Korpel, *Acousto-optics.* Optical engineering ; 57, New York: Dekker, 2nd ed. ed., 1997.

[50] G. V. Kulak and T. V. Nikolaenko, "Reflection of light from a plane-parallel layer modulated by ultrasound," *Optics and Spectroscopy*, vol. 98, no. 1, pp. 84–88, 2005. 84.

[51] . Settles, G. S. (Gary S.), *Schlieren and shadowgraph techniques : visualizing phenomena in transparent media.* Experimental fluid mechanics, Berlin ;: Springer, 2001.

[52] N. Kudo, "A simple technique for visualizing ultrasound fields without schlieren optics," *Ultrasound in Medicine and Biology*, vol. 41, pp. 2071–2081, July 2015.

[53] N. Kudo, "Optical methods for visualization of ultrasound fields," *Japanese Journal of Applied Physics*, vol. 54, p. 07HA01, June 2015.

[54] J. Rienitz, "Schlieren experiment 300 years ago," *Nature*, vol. 254, pp. 293–295, Mar 1975.

[55] A. Martínez-González, D. Moreno-Hernández, M. León-Rodríguez, C. Carrillo-Delgado, and E. Cossío-Vargas, "Simultaneous schlieren-shadowgraph visualization and temperature measurement fields of fluid flow using one color CCD camera," *Sensors*, vol. 22, p. 9529, Dec. 2022.

[56] D. Möller, N. Degen, and J. Dual, "Schlieren visualization of ultrasonic standing waves in mm-sized chambers for ultrasonic particle manipulation," *Journal of Nanobiotechnology*, vol. 11, no. 1, p. 21, 2013.

[57] T. Neumann and H. Ermert, "Schlieren visualization of ultrasonic wave fields with high spatial resolution," *Ultrasonics*, vol. 44, pp. e1561–e1566, Dec. 2006.

[58] A. Hanafy and C. Zanelli, "Quantitative real-time pulsed schlieren imaging of ultrasonic waves," in *IEEE 1991 Ultrasonics Symposium,*, pp. 1223–1227 vol.2, 1991.

[59] B. Porter, "Quantitative real-time schlieren system for ultrasound visualization," *Review of Scientific Instruments*, vol. 55, pp. 216–221, Feb. 1984.

[60] B. Schneider and K. K. Shung, "Quantitative analysis of pulsed ultrasonic beam patterns using a schlieren system," *IEEE TRANSACTIONS ON ULTRASONICS FERROELECTRICS AND FREQUENCY CONTROL UFFC*, vol. 43, no. 6, pp. 1181–1186, 1996. 1181.

[61] Q. Zhou, J. Zhang, X. Ren, Z. Xu, and X. Liu, "Multi-bottle beam generation using acoustic holographic lens," *Applied Physics Letters*, vol. 116, p. 133502, Mar. 2020.

[62] Z. Xu, H. Chen, X. Yan, M.-L. Qian, and Q. Cheng, "Three-dimensional reconstruction of nonplanar ultrasound fields using radon transform and the schlieren imaging method," *The Journal of the Acoustical Society of America*, vol. 142, pp. EL82–EL88, July 2017.

[63] B. Schneider and K. K. Shung, "Quantitative analysis of pulsed ultrasonic beam patterns using a schlieren system," *IEEE Transactions on Ultrasonics, Ferroelectrics, and Frequency Control*, vol. 43, no. 6, 1996.

[64] A. Crockett and W. Rueckner, "Visualizing sound waves with schlieren optics," *American Journal of Physics*, vol. 86, pp. 870–876, Nov. 2018.

[65] M. J. Hargather, G. S. Settles, and M. J. Madalis, "Schlieren imaging of loud sounds and weak shock waves in air near the limit of visibility," *Shock Waves*, vol. 20, pp. 9–17, Aug. 2009.

[66] V. Contreras and A. Marzo, "Adjusting single-axis acoustic levitators in real time using rainbow schlieren deflectometry," *Rev. Sci. Instrum.*, vol. 92, p. 015107, Jan 2021.

[67] M. Iodice, W. Frier, J. Wilcox, B. Long, and O. Georgiou, "Pulsed schlieren imaging of ultrasonic haptics and levitation using phased arrays," Sep 2018.

[68] A. Bauknecht, B. Ewers, C. Wolf, F. Leopold, J. Yin, and M. Raffel, "Three-dimensional reconstruction of helicopter blade–tip vortices using a multi-camera bos system," *Experiments in Fluids*, vol. 56, p. 1866, Dec 2014.

[69] H. Richard and M. Raffel, "Principle and applications of the background oriented schlieren (bos) method," *Measurement science & technology.*, vol. 12, no. Part 9, pp. 1576–1585, 2001. 1576.

[70] M. Kremer, C. Caskey, and W. Grissom, "Background-oriented schlieren imaging and tomography for rapid measurement of FUS pressure fields: initial results," *Journal of Therapeutic Ultrasound*, vol. 3, June 2015.

[71] E. Koponen, J. Leskinen, T. Tarvainen, and A. Pulkkinen, "Nonlinear estimation of pressure projection of ultrasound fields in background-oriented schlieren imaging," *J. Opt. Soc. Am. A*, vol. 39, pp. 552–562, Apr 2022.

[72] M. Iodice, W. Frier, J. Wilcox, B. Long, and O. Georgiou, "Pulsed schlieren imaging of ultrasonic haptics and levitation using phased arrays," 2018.

[73] H. Takei, T. Hasegawa, K. Nakamura, and S. Ueha, "Measurement of intense ultrasound field in air using fiber optic probe," *Japanese journal of applied physics.*, vol. 46, no. 7 S, p. 4555, 2007. 4555.

[74] S. J. Sanabria, T. Marhenke, R. Furrer, and J. Neuenschwander, "Calculation of volumetric sound field of pulsed air-coupled ultrasound transducers based on single-plane measurements," *IEEE Transactions on Ultrasonics, Ferroelectrics, and Frequency Control*, vol. 65, pp. 72–84, Jan. 2018.

[75] S. F. Wu, *The Helmholtz equation least squares method.* New York, NY: Springer New York, 2015.

[76] N. Aujogue, A. Ross, and J.-M. Attendu, "Time-space domain nearfield acoustical holography for visualizing normal velocity of sources," *Mechanical Systems and Signal Processing*, vol. 139, 2020.

[77] S. A. Tsysar, D. A. Nikolaev, and O. A. Sapozhnikov, "Broadband vibrometry of a two-dimensional ultrasound array using transient acoustic holography," *Acoust. Phys.*, vol. 67, pp. 320–328, May 2021.

[78] M. . Raffel, C. E. Willert, F. Scarano, C. J. Kahler, S. T. Wereley, and J. Kompenhans, "Particle image velocimetry : a practical guide," 2018.

[79] J. C., G. E.R., J. H., and A. C.J., "On the temporal analysis of acoustic waves using schlieren imaging," *Measurement: Journal of the International Measurement Confederation*, vol. 116, pp. 507–513, 2018. 507.

[80] M. J. Hargather and G. S. Settles, "A comparison of three quantitative schlieren techniques," *Optics and Lasers in Engineering*, vol. 50, no. 1, pp. 8–17, 2012. 8.

[81] E. H. Trinh and J. L. Robey, "Experimental study of streaming flows associated with ultrasonic levitators," *Physics of Fluids*, vol. 6, no. 11, pp. 3567–3579, 1994. 3567.

[82] S. Biswas, *Schlieren Image Velocimetry (SIV)*, pp. 35–64. Springer Theses 2190-5061, Cham : Springer International Publishing : Springer, 2018.

[83] J. Yin, C. Tao, P. Cai, and X. Liu, "Photoacoustic tomography based on the green's function retrieval with ultrasound interferometry for sample partially behind an acoustically scattering layer," *Applied Physics Letters*, vol. 106, p. 234101, June 2015.

[84] D. R. Bacon, "Primary calibration of ultrasonic hydrophone using optical interferometry," *IEEE Transactions on Ultrasonics, Ferroelectrics, and Frequency Control*, vol. 35, no. 2, 1988.

[85] P. F. U. Ortiz, J. Perchoux, A. L. Arriaga, F. Jayat, and T. Bosch, "Visualization of an acoustic stationary wave by optical feedback interferometry," *Optical Engineering*, vol. 57, p. 1, Feb. 2018.

[86] M. Ueda, Y. Oshida, K. Iwata, and R. Nagata, "Visualization of high frequency ultrasonic wavefronts by holographic interferometry," *IEEE Transactions on Sonics and Ultrasonics*, vol. 28, no. 6, 1981.

[87] T. A. Pitts, A. Sagers, and J. F. Greenleaf, "Optical phase contrast measurement of ultrasonic fields.," *IEEE transactions on ultrasonics, ferroelectrics, and frequency control*, vol. 48, no. 6, pp. 1686–94, 2001. 1686.

[88] J. J. Pulkkinen, Akiand Leskinen and A. Tiihonen, "Ultrasound field characterization using synthetic schlieren tomography.," *The Journal of the Acoustical Society of America*, vol. 141, no. 6, p. 4600, 2017. 4600.

[89] M. Kremer, C. Caskey, and W. Grissom, "Background-oriented schlieren imaging and tomography for rapid measurement of FUS pressure fields: initial results," *Journal of Therapeutic Ultrasound*, vol. 3, June 2015.

[90] E. Koponen, J. Leskinen, T. Tarvainen, and A. Pulkkinen, "Acoustic pressure field estimation methods for synthetic schlieren tomography," *The Journal of the Acoustical Society of America*, vol. 145, pp. 2470–2479, Apr. 2019.

[91] I. Butterworth, A. Shaw, and . 39th Annual Ultrasonic Industry Association Symposium (UIA) Cambridge, *Realtime acousto-optical QA methods for high intensity fields*, pp. 1–5. Proceedings of the 39th Annual Symposium of the Ultrasonic Industry Association, IEEE, 2010.

[92] G. S. Settles and M. J. Hargather, "A review of recent developments in schlieren and shadowgraph techniques," *Measurement Science and Technology*, vol. 28, p. 042001, Feb. 2017.

[93] J. S. Harvey, H. E. Smithson, and C. R. Siviour, "Visualization of acoustic waves in air and subsequent audio recovery with a high-speed schlieren imaging system: Experimental and computational development of a schlieren microphone," *Optics and Lasers in Engineering*, vol. 107, pp. 182–193, Aug. 2018.

[94] L. A. Vasilev and A. Baruch, *Schlieren methods*. Israel Program for Scientific Translations, 1971.

[95] L. A. Yates, A. I. of Aeronautics, Astronautics., and T. AIAA Aerospace Ground Testing Conference (17th : 1992 : Nashville, *Images constructed from computed flowfields*. Paper / American Institute of Aeronautics and Astronautics, Washington, D.C: AIAA, 1992.

[96] E. Luthman, N. Cymbalist, D. Lang, G. Candler, and P. Dimotakis, "Simulating schlieren and shadowgraph images from LES data," *Exp. Fluids*, vol. 60, Aug. 2019.

[97] J. Hinrichs, Y. Bendel, M. Rutsch, G. Allevato, M. Sachsenweger, A. Jager, and M. Kupnik, "Schlieren photography of 40 kHz leaky lamb waves in air," in *2020 IEEE International Ultrasonics Symposium (IUS)*, IEEE, Sept. 2020.

[98] N. Chitanont, K. Yaginuma, K. Yatabe, and Y. Oikawa, "Visualization of sound field by means of schlieren method with spatio-temporal filtering," in *2015 IEEE International Conference on Acoustics, Speech and Signal Processing (ICASSP)*, IEEE, Apr. 2015.

[99] J. L. Chaloupka, r. Woods, Maurice, J. Aas, J. Hutchins, and J. D. Thistle, "Color schlieren imaging with a two-path, double knife edge system," *Opt. Express*, vol. 22, pp. 8041–8046, Apr 2014.

[100] M. Ohno, N. Tanaka, and Y. Matsuzaki, "Schlieren imaging by the interference of two beams in raman-nath diffraction," *Japanese Journal of Applied Physics*, vol. 42, pp. 3067–3071, May 2003.

[101] J. Nakamura, "Image sensors and signal processing for digital still cameras," 2006.

[102] N. Pérez, M. A. B. Andrade, R. Canetti, and J. C. Adamowski, "Experimental determination of the dynamics of an acoustically levitated sphere," *Journal of Applied Physics*, vol. 116, p. 184903, Nov. 2014.

[103] S.-T. Chen and C. li Sun, "Out-of-focus effects on microscale schlieren measurements of mass transport in a microfluidic device," *Measurement Science and Technology*, vol. 27, p. 085203, July 2016.

[104] E. Reichel and B. Zagar, "Phase contrast method for measuring ultrasonic fields," *IEEE Transactions on Instrumentation and Measurement*, vol. 55, pp. 1356–1361, Aug. 2006.